A Design Study for an Experiment to Search for Dark Photons at ELSA

Dissertation
zur
Erlangung des Doktorgrades (Dr. rer. nat.)
der
Mathematisch-Naturwissenschaftlichen Fakultät
der
Rheinischen Friedrich-Wilhelms-Universität Bonn

vorgelegt von
Jan - Eric Heinrichs
aus
Düren

Bonn 2025

Angefertigt mit Genehmigung der Mathematisch-Naturwissenschaftlichen Fakultät der Rheinischen Friedrich-Wilhelms-Universität Bonn

Gutachter/Betreuer:	Prof. Dr. Klaus Desch
Gutachter:	Prof. Dr. Jochen Dingfelder
Tag der Promotion:	07.10.2025
Erscheinungsjahr:	2025

Foreword

The design study this thesis is concerned with works towards an experimental proposal with the name Lohengrin. It is perhaps more well known as an opera written by Wagner. This might seem rather unusual as names for experiments in physics traditionally consist of witty acronyms, with recursive acronyms also becoming more fashionable over the years. Lohengrin however currently does not stand for an acronym at the moment. The following text gives some insights into the reasoning behind the name. Certain parallels to the opera become apparent during the course of the thesis.

The opera Lohengrin is set in 10^{th} century Antwerp. One of the main characters **Elsa** is accused of murdering her brother Gottfried (heir to the Brabantian throne) and thus faces trial. The trial is conducted by combat. None of the Brabantian knights offer their assistance to fight for **Elsa**. She does however dream of a mysterious saviour who also suddenly arrives in a boat. In addition to offering to fight for her, he also asks for her hand in marriage. This is however linked to the condition of **Elsa** not being allowed to ask for his name nor his origin[1]:

> Nie sollst du mich befragen,
> noch Wissens Sorge tragen,
> woher ich kam der Fahrt,
> noch wie mein Nam' und Art.
>
> — *Richard Wagner*

Due to doubts sown by the defeated knight, **Elsa** gives in and asks the mysterious stranger for his name. He obliges and reveals being a grail knight named **Lohengrin**. After **Lohengrin's** identity is revealed by **Elsa** he is forced to leave and disappear with the boat he came with.

[1] This is an excerpt from the first act of Lohengrin[1]

Acknowledgements

I would like to begin by expressing my gratitude to my advisor, Klaus Desch, for providing me the opportunity to be a member of his research group and working on this thesis. The unwavering support, guidance and mentorship was instrumental in finishing this work.

I am also deeply thankful to Matthias and Philip for their valuable feedback, thoughtful suggestions and time spent for advice during the last few years. Thank you for giving reassurance in times of need.

Thanks also go to Andreas Salzburger for mentoring me during a research stay at CERN and providing me with insights into the topic of tracking, I otherwise probably would not have gotten.

To my colleagues and friends at the PI and FTD, thank you for creating a collaborative and supportive environment that made every step of this journey not only possible, but also enjoyable. To Cedric, Lena, Luka, Murillo, and Simon, whom I shared the office with, and Laney for the unparalleled sense of community and fruitful discussions during coffee breaks.

To my family, there are no words that can adequately express how grateful I am for your love and support. To my parents, Astrid and Bernd, thank you for always believing in me and for supporting me during my academic journey. To my sister Lara, your support has kept me grounded and reminded me to keep a sense of humuor throughout the ups and downs.

Lastly, to my close friends Dominik, Nassim, Patrick, Rieka, Roman, Srijan, and Svenja, who have been there through it all — thank you for your constant encouragement and for making sure I got the recreation I needed. Your companionship and understanding have been invaluable.

This thesis is as much a reflection of your encouragement as it is of my own efforts. It would not have been possible without you.

Contents

Chapter 1

Introduction and Scope of this Work

The Standard Model of particle physics (SM) describes elementary particles and the interactions between them (excluding gravity) with previously unknown precision. It is however known to be an incomplete theory. It does not provide an answer to the strong CP problem [2], the origin of neutrino masses, or the true nature of dark matter (DM) [3]. Many extensions concerning the inclusion of DM into the SM have been proposed and some of these have also been experimentally probed (see [4–9]). Weakly interacting massive particles (WIMPs) in the mass range of GeV to TeV have been considered to be excellent DM candidates [10]. However, direct DM search experiments and indirect bounds from LHC experiments provide ever stronger limits on the possible WIMP parameter space [10]. Consequently, other models explaining the nature of DM are receiving more attention. One such model introduces a new gauge interaction based on a spontaneously broken symmetry. DM particles are introduced as either scalar or fermionic particles which form a dark sector. The associated gauge boson, the dark photon, then feebly couples to the SM through kinetic mixing, thus acting as a portal between the SM and the dark sector [10].

This thesis provides a design study for a proposed dark photon search experiment at the ELSA accelerator at the university of Bonn, called Lohengrin. The aim of Lohengrin is to search for dark photons by employing a missing momentum measurement of single electrons traversing a thin target. Making use of the unique kinematics of the dark photon production signal process called dark Bremsstrahlung. The strength of this approach is based on the fact, that the sensitivity is not limited by the conversion of dark sector particles back into SM particles. As discussed in [10], the idea of fixed target missing momentum searches stems from [11], while the fundamental predictions have been carried out in [12–16].

The most relevant results from this thesis have been published in a whitepaper describing the experiment and providing a sensitivity estimate: [10]. Significant work was done concerning the simulation of two critical components for the proposed detector:

the electromagnetic calorimeter and the tracker. The studies show that a highly granular SiW electromagnetic calorimeter can meet the requirements of the LOHENGRIN experiment for the photon veto, if some changes are made to the readout ASIC. Furthermore the experiment will benefit from a thin pixelized tracking detector built from monolithic active pixel sensors. This thesis focuses on the detailed description of the simulation studies being performed for these two components of the experiment and how they can ultimately be used for a combined sensitivity estimate. Nevertheless the entire proposed experiment is described in this thesis. Consequently, other relevant parts of the proposal in [10] are described where necessary for the understanding. Parts which are mostly based on or summarised from [10] are appropriately marked at the beginning of the respective chapter or section.

This thesis is organised as follows: Chapter 2 explains the necessary theoretical background of this thesis in general. The concept behind LOHENGRIN is introduced in Chapter 3. It also contains additional theoretical considerations specific to the design of LOHENGRIN and an overview and explanation of all of the foreseen detector components. The general simulation framework, `ExPlORA`, is explained in Chapter 4 by constructing a simple example. A potential first level trigger for the experiment, based on the tracking information, is described in Chapter 5. Studies concerning the calorimetry for LOHENGRIN are collected in Chapter 6. The tracking setup is simulated in Chapter 7. Results from considerations and simulations of all detector components subsequently allow to give a sensitivity estimate of the proposed experiment, which is given in Chapter 8. Finally, the thesis concludes with a short summary and outlook in Chapter 9.

Unit Conventions

Natural units are adopted throughout this thesis where feasible:

$$\hbar = c = 1$$

As a result, energies and momenta are typically expressed in electronvolt (with or without a corresponding prefix). However, spatial quantities in the macroscopic world, such as the dimensions of a detector or detector components, are expressed in terms of SI units to maintain consistency with experimental conventions.

Chapter 2

Theoretical Background

This chapter serves as a short overview and introduction to the theoretical concepts needed for this thesis. It contains information about the standard model of particle physics and possible extensions to accommodate dark photons - the particle whose discovery is the main driver for the LOHENGRIN experiment. This also includes an overview on production mechanisms accessible to experiments based at accelerators such as ELSA. Detailed information is omitted in favour of brevity where appropriate. More information can be found in the cited references. Explanations concerning algorithms and simulation setup are given in sections where they become relevant and before this knowledge is required.

This chapter loosely follows a similar overview given in [17].

2.1 The Standard Model of Particle Physics

The standard model of particle physics (SM) encapsulates our current understanding of particles and their interactions. This includes the strong force, the weak force and electromagnetism. Notably it does not provide a description for gravity. Due to the relative weakness of gravity however, it does usually not play a role in elementary particle physics.

The SM provides us with the tools to accurately predict cross sections for particle interactions which can then be verified in experiments to astonishing precision. Notable examples for particles predicted by the SM, which were then found in later experiments, include the discovery of the top quark in 1995 by the D0 [19] and CDF [20], and the Higgs boson in 2012 by the ATLAS[21] and CMS collaborations[22].

2.1.1 Overview of Particles and Interactions

A schematic overview of fundamental particles and their interactions in the SM can be found in Fig. 2.1. The particles in the SM can be grouped into leptons and quarks (spin

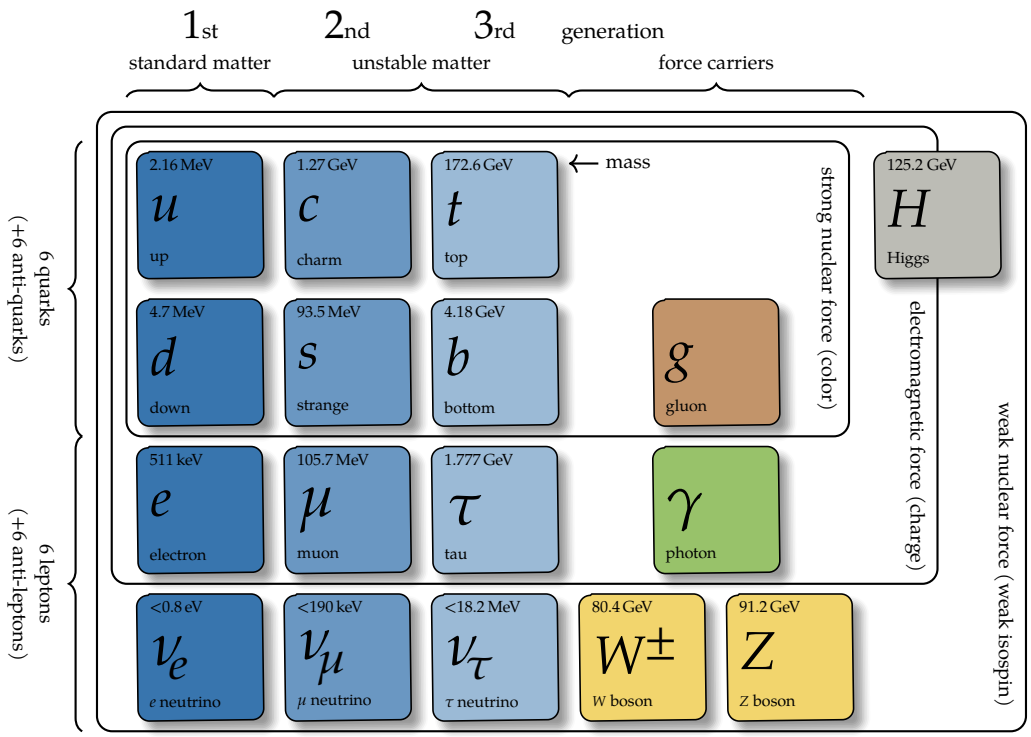

Figure 2.1: The Standard Model of Particle Physics with all known particles [18].

1/2), gauge bosons (spin 1) and the Higgs boson (spin 0). In general particles (this includes particles made up of several elementary particles) can be differentiated into bosons with integer spin and fermions with half integer spin.

As seen in Fig. 2.1 some particles are also divided into generations. The particles in one generation are generally similar to particles in another generation. They do however significantly differ in mass. The first generation contains the lightest particles which are stable. Particles from higher generations can ultimately decay into particles from the first. This rule does not apply to the neutrinos though.

The forces in the SM are mediated by the photon (electromagnetism), W and Z bosons (weak force) and gluons (strong force). The Higgs boson is not a force carrier, but is used to give particles their mass via the Higgs mechanism [23].

As already stated in Section 2.1, gravity is not included in the SM. It also does not play any role in the scope of this work due to its relative strength compared to other forces. It is about 31 orders of magnitude weaker than the weak force for two particles at a distance of about 1 fm [24].

2.1.2 Quantum Electrodynamics

The SM is formulated as a quantum field theory with gauge group $\mathrm{SU(3)_C \times SU(3)_L \times U(1)_Y}$. The full theory can be written down in the form of a Lagrangian. Cross sections can then be calculated by using the Hamiltonian formalism and perturbation theory. A comprehensive overview is given in [25]. Particles can be thought of as excitations in the respective quantum field.

Each gauge group is responsible for different fundamental interactions. The SM lagrangian can hence be looked at in parts, which correspond to individual gauge groups and their respective interactions. Electromagnetic interactions play a crucial role for the understanding of this thesis. They are thus shortly highlighted here.

The electromagnetic interaction between electrically charged particles is described by quantum electrodynamics (QED). One starts with the Dirac Lagrangian describing a free fermion with the field ψ and mass m [25]

$$\overline{\psi}(i\gamma^\mu \partial_\mu - m)\psi. \tag{2.1}$$

The interactions of QED arise if one requires the Lagrangian to be invariant under local gauge transformations corresponding to that group [26]:

$$\psi(x) \to e^{i\alpha(x)}\psi(x). \tag{2.2}$$

This is achieved by introducing the so called covariant derivative D_μ with a new vector field A_μ given in Eq. (2.3) [26].

$$D_\mu \psi(x) = \partial_\mu \psi(x) + ieA_\mu \psi(x), \quad A_\mu(x) \to A_\mu(x) - \frac{1}{e}\partial_\mu \alpha(x) \tag{2.3}$$

Requiring local gauge invariance also allows for the addition of the kinetic term of the previously introduced field A_μ [26]:

$$\frac{1}{4}F^{\mu\nu}F_{\mu\nu}, \quad F_{\mu\nu} = \partial_\mu A_\nu - \partial_\nu A_\mu. \tag{2.4}$$

The QED part of the SM Lagrangian ($\mathcal{L}_{\mathrm{QED}}$) can hence be written as [25, 26]:

$$\mathcal{L}_{\mathrm{QED}} = \frac{1}{4}F^{\mu\nu}F_{\mu\nu} + i\overline{\psi}\not{D}\psi - m\overline{\psi}\psi. \tag{2.5}$$

In Eq. (2.5) $F_{\mu\nu}$ is the electromagnetic field strength tensor, ψ the Dirac field of a fermion, $\not{D} = \gamma^\mu(\partial_\mu + ieA_\mu)$ the covariant derivative (see [25] for Dirac slash notation) and m is the mass of the respective fermion.

All types of electromagnetic interactions between charged particles can be described with this Lagrangian. Of particular importance for this thesis is a process called Bremsstrahlung. It serves as the basis for the production process of dark photons (see Section 2.4).

2.2 Dark Matter and the Dark Sector

While the SM is remarkably successful in predicting and explaining many phenomena, it is commonly understood that it is at least incomplete. Several observations cannot be explained by the current state of the SM though proposed extensions do exist.

The oscillations of neutrinos were observed in e.g. solar neutrino experiments like the Super-Kamiokande [27, 28] and SNO [29, 30], reactor based experiments like KamLAND [31], Daya Bay[32] and Double Chooz [33], and accelerator based experiments like MINOS [34] and T2K [35]. These observed oscillations mean that at least two of three known neutrino types must have a non-zero mass. This is however in contradiction to the SM, where neutrinos are massless.

Quantum chromodynamics (QCD) allows for terms in the QCD Lagrangian which inherently are *CP* violating [25]. These terms can have physical effects. In order to be consistent with observations (where *CP* is conserved in strong interactions), the strong *CP* phase must be small despite the large amount of *CP* violation in the weak sector [25]. This became known as the strong *CP* problem. One possible solution is the introduction of axions as extension to the SM [2, 25]. The axion has not been discovered yet, but is searched for in several experiments, like the IAXO experiment [36].

Another area so far inaccessible to the SM is dark matter (DM). A form of matter which can only be observed through its interaction via gravity. Hence the attribute *dark* as part of its name [37]. Several observations from cosmological experiments hint at its existence. Obtaining any handle for probing this kind of matter or the dark sector in particle physics experiments seems challenging due to the irrelevance of gravity (see also Section 2.1.1). A possible mechanism exploring portal interactions between the SM and the dark sector is highlighted in Section 2.4. Some notable examples hinting at the existence of DM are highlighted in the following.

A very instructive and compelling piece of evidence for the existence of DM can be obtained by studying the rotation curves of galaxies. The distribution of visible matter can be inferred from the distribution of stars within it. This coupled with the current understanding of gravity on macroscopic scales gives an expected rotational velocity of stars depending on their distance from the galactic centre. This prediction can be compared to the actual velocity of stars in e.g. the milky way as seen in Fig. 2.2. The stellar and gas density decrease exponentially with distance to the galactic centre. The rotational velocity should thus be $\propto 1/\sqrt{\text{distance}}$ [37]. The observations do however indicate that the

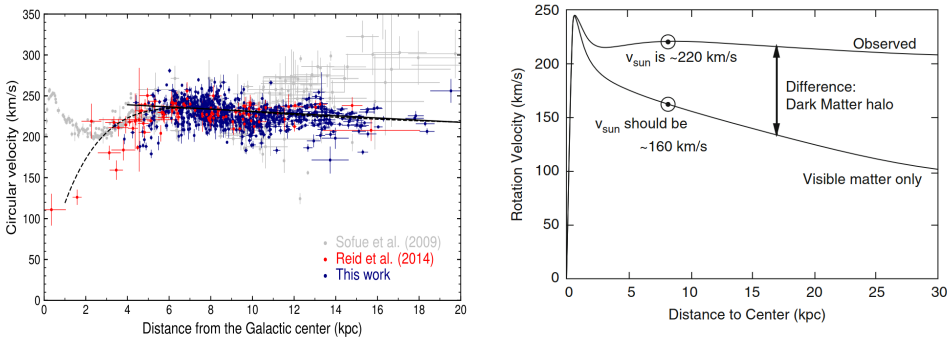

(a) Taken from [38]. (b) Taken from [37].

Figure 2.2: Rotation curves for the milky way. (a): Measurement of the rotation curve of the milky way. (b): Rotation curve of the milky way where measurements are summarised to a single line and the prediction based on visible matter is also shown. The position of the sun is marked as well as the difference in speeds due to the presence of DM.

velocity stays almost constant. Hence implying the existence of gravitationally interacting matter invisible to observations.

Another notable example is the observation of gravitational lensing in large clusters of galaxies. Fig. 2.3 shows galaxies clearly distorted by the presence of matter due to gravitational lensing of the cluster of galaxies towards the middle of the picture. The actual extent of lensing can be compared to predictions based on the distribution of visible matter in the cluster. Discrepancies are attributed to the existence of dark matter being present [39].

So far searches for DM have been unsuccessful in the sense that no DM has been found or the experiments were not reproducible (for an overview see e.g. [4–9]).

One possible DM candidate is the existence of a weakly interacting massive particle (WIMP). These are particles with masses in excess of 100 GeV interacting via the weak force with the SM. This scenario has been well tested in experiments producing powerful null results [4, 5].

Another possibility is to investigate lower mass ranges of $\approx$ 0.01 to 1 GeV, which is realised via portal interactions to the dark sector. This possibility is investigated in further detail below.

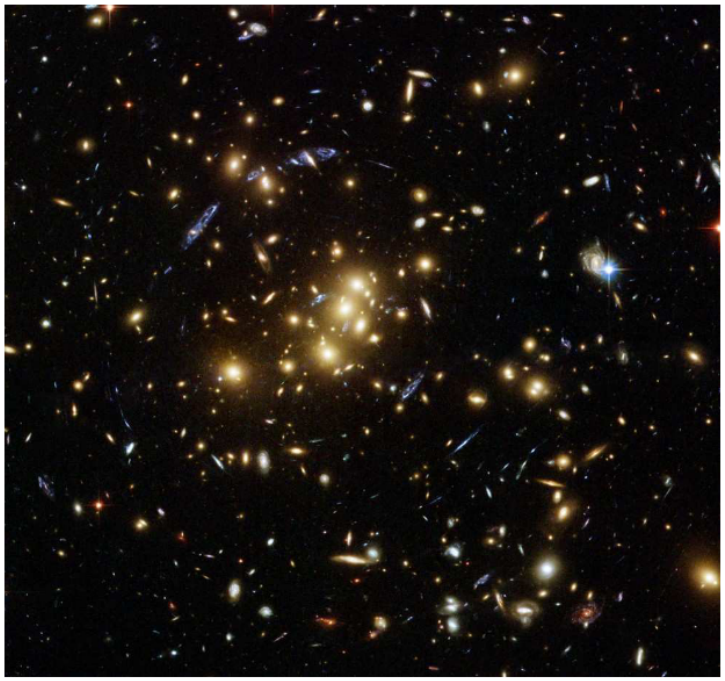

Figure 2.3: Gravitational lensing around the galaxy cluster CL0024+17. Taken from [39].

2.3 Possible Portal Interactions Accessible to Accelerator Based Experiments

As outlined in Section 2.2 the possible existence of DM provides a strong motivation to search for physics beyond the Standard Model. One way to extend it is by introducing a coupling to a mediator which can serve as portal to a dark sector. Several possibilities for such a mediator exist. One case, the dark photon, is highlighted in more detail in Section 2.4. An overview based on the discussions in [15, 16] is given in this section.

Mediator Spin 1 The interaction between SM leptons l and this new mediator can be expressed with the following Lagrangian [15]:

$$\mathcal{L} = \varepsilon e \begin{cases} A'_\mu \bar{l}\gamma^\mu l & \text{vector} \\ Z'_\mu \bar{l}\gamma^\mu P_{L,R}\gamma^\mu & \text{chiral vector} \\ V^\mu \bar{l}\gamma^\mu\gamma^5 l & \text{axial vector.} \end{cases} \tag{2.6}$$

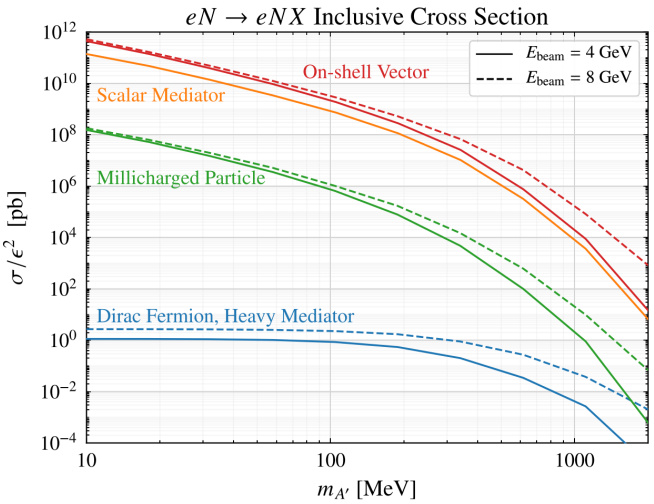

Figure 2.4: Fixed target production cross sections different mediator scenarios 4 and 8 GeV electron beams hitting a 0.1 X_0 tungsten target. Taken from [15]

In Eq. (2.6), A'_μ, Z'_μ, V_μ are the vector, chiral vector and axial vector mediator respectively, ε encodes the strength of the coupling, e is the elementary charge and $P_{L,R} = (1 \mp \gamma^5)/2$ is the left/right projection operator [15].

Mediator Spin 0 The interaction between SM leptons l and this new mediator can be expressed with the following Lagrangian [15]:

$$\mathcal{L} = \varepsilon e \begin{cases} s\bar{l}l & \text{scalar} \\ ia\bar{l}\gamma^5 l & \text{pseudoscalar.} \end{cases} \tag{2.7}$$

In Eq. (2.7), s and a represent the scalar and pseudoscalar fields respectively [15].

In order to evaluate the feasibility of these models, it is possible to look at the potential production cross section at accelerators like ELSA. This means an achievable energy in the 3 to 4 GeV range. The production cross section for different mediators and mediator masses is given in Fig. 2.4. The heavy mediator and millicharged particle case in this figure are not treated in more detail and omitted, because they become relevant once the mediator is too heavy for direct detection or the mediator decay into DM pairs is kinematically forbidden [15] (see also Section 2.4.1). Bounds on chiral vector and axial vector mediators are very strong and thus also not investigated further [15]. They are summarised in e.g. [40, 41]. It can be seen, that the vector mediator has the highest

potential production cross section in a fixed target experiment at energies accessible to accelerators like ELSA. Furthermore, this interaction can be added to the SM in a seamless way by adding a new $U(1)$ gauge symmetry (see Section 2.4). It is also possible to obtain minimal values for the coupling based on cosmological observations (see Section 2.4.2). This is especially noteworthy as it uses results from a completely different branch of physics working on completely different scales.

Further emphasis is thus put on the dark photon being the vector type mediator for the remainder of this chapter.

2.4 Dark Photons

The SM was introduced as a quantum field theory. One of the simplest extensions to it is the addition of an additional $U(1)_D$ gauge group which gives rise to interactions similar to QED. This allows the introduction of a new gauge boson (the dark photon). It is important to note, that this addition can be done irrespective of what a potential dark sector can look like. The potential existence of a dark sector with dark matter particles does however provide a strong motivation and predictive targets as use case for this addition to the SM. The dark photon can then serve as a portal between the SM and possible dark matter particles. This works by adding the following terms in $\mathcal{L}_{A_\mathrm{D}}$ to the SM Lagrangian [4, 10]:

$$\begin{aligned}\mathcal{L}_{A_\mathrm{D}} = &-\frac{1}{4}F_{\mathrm{D}\mu\nu}F_\mathrm{D}^{\mu\nu} + \frac{1}{2}m_{A_\mathrm{D}}^2 A_\mathrm{D}^\mu A_{\mathrm{D}\mu} - \frac{\sin\varepsilon_Y}{2}F_\mathrm{D}^{\mu\nu}B_{\mu\nu} \\ &- g_D A_{\mathrm{D}\mu}J_D^\mu + \text{relevant DM mass terms.}\end{aligned} \tag{2.8}$$

In Eq. (2.8), $F_\mathrm{D}^{\mu\nu} = \partial^\mu A_\mathrm{D}^\nu - \partial^\nu A_\mathrm{D}^\mu$ is the field strength tensor of the new gauge field, m_{A_D} is the corresponding mass, J_D^μ is the current associated with dark matter scalars or fermions. The kinetic mixing parameter $F_\mathrm{D}^{\mu\nu}B_{\mu\nu}$ allows for interactions between the dark photon mass eigenstates A'_μ with mass $m_{A'} \approx m_{A_\mathrm{D}}$ and SM fermions with electric charge Q_f. The tensor $B_{\mu\nu}$ is not to be confused with $F_{\mu\nu}$ from Eq. (2.5). It describes the SM hypercharge field which is obtained with electroweak unification [25]:

$$B_{\mu\nu} = \partial_\mu B_\nu - \partial_\nu B_\mu \quad \text{, where} \tag{2.9}$$

$$B_\mu = \cos\theta_W A_\mu - \sin\theta_W Z_\mu. \tag{2.10}$$

Here A_μ and Z_μ are the photon and Z boson field respectively. θ_W is the weak mixing angle.

QED can hence be thought of a special case of electroweak unification. The SM fermion

couplings to the dark photon field can be expressed as [10]:

$$\mathcal{L} = i \sum_f Q_f \varepsilon \bar{f} \gamma^\mu f A'_\mu. \tag{2.11}$$

In Eq. (2.11) $\varepsilon = \varepsilon_Y \cos\theta_W$ is called the reduced kinetic mixing parameter. And the sum is to be understood to run over all possible fermion fields f.

2.4.1 Direct and Secluded Annihilation

One possible model to explain the DM abundance in the current universe which is well motivated is a thermal DM freeze-out model [4, 5]. In this model DM and ordinary matter are in equilibrium in the early universe. Particles are essentially transformed between the dark sector and the SM during this time. During the expansion of the early universe, temperatures decrease. Once the temperature reaches a critical point, this equilibrium is broken and so called freeze-out occurs[42, 43]. The fraction of DM to ordinary matter also does not change any more from this point. The current abundance of DM can be determined by observing the cosmic microwave background [4].

This fact places strict bounds on any kind of coupling parameters for a dark sector. In order to not overproduce DM in the early universe, the thermally averaged annihilation cross section $\langle \sigma v \rangle$ needs to be at least [4, 10]

$$\langle \sigma v \rangle = 3 \times 10^{-26}\,\mathrm{cm}^3\,\mathrm{s}^{-1} \approx 10 \times 10^{-9}\,\mathrm{GeV}^{-2}. \tag{2.12}$$

One now has to make an important distinction, which is important for the predictive power of this portal interaction model. So far a part of the dark sector was not highlighted. This part is hidden in the second line of Eq. (2.8). It contains the generalised current and mass terms of DM particles without specifying anything about these particles. There are two cases to take a look at:

Direct Annihilation Let m_χ be the mass of the hypothetical DM particle. It is assumed that $m_{A'} > m_\chi$. In this case the DM particles can decay via a mediator (e.g. the dark photon) to SM particles. The annihilation cross section in this case becomes (assuming the coupling is only to SM particles with unit charge) [10]:

$$\langle \sigma v \rangle \propto \frac{1}{6\pi} \frac{g_D^2 \varepsilon^2 m_\chi^2 v^2}{(m_{A'}^2 - 4m_\chi^2)^2 + m_{A'}^2 \Gamma_{A'}^2} \quad , \tag{2.13}$$

where $\Gamma_{A'}$ is the dark photon decay width. If one is reasonably far from the resonance and $m_{A'} \gg \Gamma_{A'}$, Eq. (2.13) can be simplified to [3, 4, 10, 44]:

$$\begin{aligned} \langle \sigma v \rangle &\propto \frac{g_D^2 \varepsilon^2 m_\chi^2}{m_{A'}^2} \propto \frac{\Upsilon}{m_{\chi^2}}, \\ \text{with } \Upsilon &= \varepsilon^2 \left(\frac{m_\chi}{m_{A'}} \right)^4 \text{ and } \alpha_D = \frac{g_D^2}{4\pi}. \end{aligned} \tag{2.14}$$

By specifying $m_\chi / m_{A'}$ and g_D (or alternatively α_D), one obtains lower bounds for the parameter space of Υ and m_χ. This space corresponds to minimum viable values of ϵ in order to not overproduce DM. The coupling is directly testable at accelerators and the bounds provide so called relic targets for the sensitivity of light dark matter search experiments [10]. The exact form of those targets depends on the respective dark matter particle (see Section 2.4.2 and [3, 4, 45] for an overview). This approximation only applies off resonance [10]. A more detailed discussion of the direct annihilation case including resonance effects can be found in [46].

Secluded Annihilation Let m_χ be the mass of the hypothetical DM particle. It is assumed that $m_{A'} < m_\chi$. In this case the DM particles can decay into dark photons, which has profound implications on the annihilation cross section. It scales as [3, 4, 10]:

$$\langle \sigma v \rangle \propto \frac{g_D^4}{m_\chi^2} \tag{2.15}$$

Eq. (2.15) shows, that the cross section does not depend on the coupling from the dark sector to the SM ε. There is thus no clear predictive target for accelerator based experiments. The coupling required to produce DM at accelerators could be arbitrarily small yet still satisfy the requirements imposed by the observed DM relic abundance.

In order to have a predictive target for an accelerator based light thermal dark matter search experiment, one has to assume the direct annihilation case.

2.4.2 Possible Dark Matter Particles

The dark photon as possible portal interaction from the SM to the dark sector has been introduced. While the dark photon is part of the dark sector, there are several possibilities for dark matter candidates. Eq. (2.8) describes interactions between dark photons and dark matter particles. Different possibilities of dark matter particles and the corresponding current $J_D^\mu$are highlighted below.

Majorana Dark Matter In this case the dark photon is a Majorana fermion. It thus couples via an axial vector current [45]:

$$J_D^\mu = \frac{1}{2}\overline{\chi}\gamma^\mu\gamma^5\chi$$

Pseudo Dirac Dark Matter χ can be a Dirac fermion. If the mass term for χ is $U(1)_D$ preserving, then the model is already constrained by cosmic microwave background data, unless there is a particle-antiparticle asymmetry. If the mass terms for χ include $U(1)_D$ breaking , then χ splits into two Majorana fermions (χ_1 and χ_2) which couple off-diagonally to the A' through [45]:

$$J_D^\mu = i\overline{\chi}_1\gamma^\mu\chi_2 \quad \text{(mass basis)}$$

Scalar Elastic Dark Matter In this scenario χ is a complex scalar with $U(1)_D$ preserving mass terms [45]:

$$J_D^\mu = i(\chi^*\partial^\mu\chi - \chi\partial^\mu\chi^*)$$

Scalar Inelastic Dark Matter χ is a complex scalar particle with $U(1)_D$ breaking mass terms. Therefore, χ couples to A' inelastically and must transition to a slightly heavier state in order to scatter through the current [45]:

$$J_D^\mu = i(\chi_1^*\partial^\mu\chi_2 - \chi_2\partial^\mu\chi_1^*)$$

Taking all of the considerations from this section allows for the visualisation of relic targets for different dark matter particles. The relic targets can be seen in Fig. 2.5. As mentioned in this section, one has to assume the direct annihilation scenario and fix the ratio of $m_\chi/m_{A'}$ as well as α_D. This was done to $m_\chi/m_{A'} = 1/3$ and $\alpha_D = 0.5$. Greyed out regions indicate existing bounds from experiments. In this parameter space, the region containing the relic targets has not been excluded by previous experiments. The relative position of the relic targets only depends on the potential dark matter particle used. They all have the same coupling between SM and dark photon. There is thus significant potential scientific value in new accelerator based light thermal dark matter search experiments contributing to this area.

2.4.3 (Dark) Bremsstrahlung

Bremsstrahlung is an electromagnetic process in which a charged particle interacts with the field of another charged particle and loses energy by emitting a photon. It is originally a german word made up of the two constituents *bremsen* "to break" and *Strahlung* "radi-

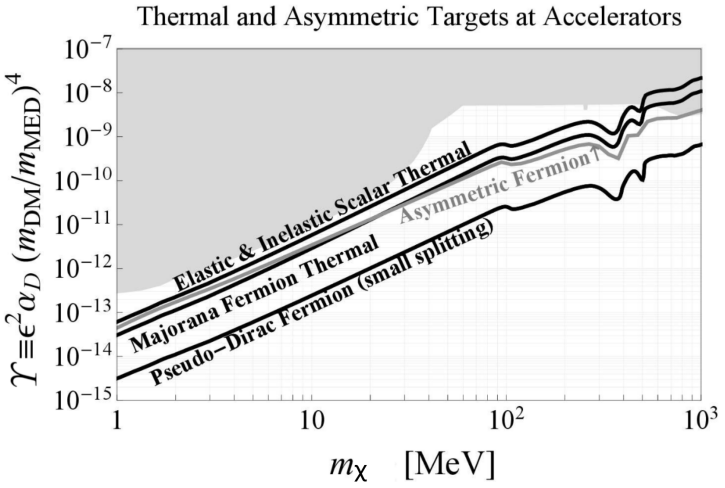

Figure 2.5: Thermal relic targets for the different dark matter particles described in Section 2.4.2. This assumes the direct annihilation scenario and a fixed ratio of $m_\chi/m_{\rm MED} = m_\chi/m_{A'} = 1/3$ as well as $\alpha_D = 0.5$. Greyed out regions indicate existing bounds from experiments. Adapted from [10].

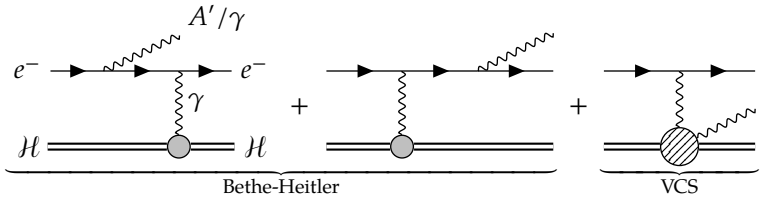

Figure 2.6: Feynman diagrams contributing to the lowest-order amplitude of (dark) photon production in collisions of an electron with an hadronic system (nucleus or quasi-free nucleons). The grey blob represents form factor evaluations while the dashed blob represents the non-trivial VCS amplitude, which in general involves structure dependent parameters. Taken from [10].

ation". Fig. 2.6 shows the corresponding Feynman diagram for an electron undergoing Bremsstrahlung in the field of a nucleus.

The electron interacts with the nucleus by exchanging a photon. It also radiates off another photon and the recoiling electron has less energy than the incoming electron. The two diagrams on the left can be categorised by the Bethe-Heitler process. The diagram on the right is referred to as virtual Compton scattering (VCS). While VCS happens on lowest order, its effects are practically negligible for the phase space relevant in this thesis [10]. If the radiated particle is a dark photon rather than a photon, this process is referred

to as dark Bremsstrahlung. Note that Bremsstrahlung can not occur in free space due to the necessary conservation of energy and momentum.

2.4.4 Kinematics

Due to the dark photon having a mass, the kinematics for both processes are different. Most notably, the dark photon carries away most of the beam energy and imparts a sizeable transverse momentum on the recoiling electron, if its mass is larger than that of the electron. The difference in energy of the recoiling electron can be seen in Fig. 2.7. It shows the distribution of simulated electrons from a 3.2 GeV beam traversing a $0.1X_0$ tungsten target. The dark photon events with 100 MeV dark photons were simulated by implementing the Lagrangian in Eqs. (2.8) and (2.11) in `MadGraph5_aMC@NLO` (see Appendix A.1 for a detailed description). The Bremsstrahlung events were simulated using the `QGSP_BERT` physics list in `Geant4` [47, 48]. The peak for both distributions is essentially on opposite ends of the graph. Fig. 2.8 shows the kinematics of the recoiling electron for dark photon production in more detail: The plots show the double differential cross section normalised to ε^2 and give information about the remaining energy fraction and scattering angle with logarithmic axis scaling. The difference between a large range of dark photon masses become apparent here.

The different kinematics for both processes will provide the main handle on the experimental rejection and analysis strategies. They will rely on measuring a significant amount of missing momentum without registering the mediator particle in any part of the proposed detector. The value of $\Upsilon = \varepsilon^2(1/3)^4/2$ is $\lesssim 10 \times 10^{-10}$ is comparatively small (see Fig. 2.9). So another interaction in the experimental assembly, after the initial dark photon production, is not expected.

The strength of this approach lies in the fact, that the sensitivity scales with ε^2 [10]. This is in contrast to a range of other beam dump and reappearance based experiments, e.g.[49–56]. The different scaling of those experiments is due to the fact, that the dark photon has to couple to the SM twice with the experimental strategies employed there.

The kinematics of dark Bremsstrahlung as presented here are independent of the interaction from the dark photon to the dark current. Thus searching for this process, is sensitive to any kind of a new $U(1)$ gauge coupling with a massive boson. This strategy will hence be able to test a multitude of possible models, including a dark photon like particle. The coupling to potential dark matter particles however is a very compelling possibility with predictive targets constrained by cosmological observations (see Section 2.4.2).

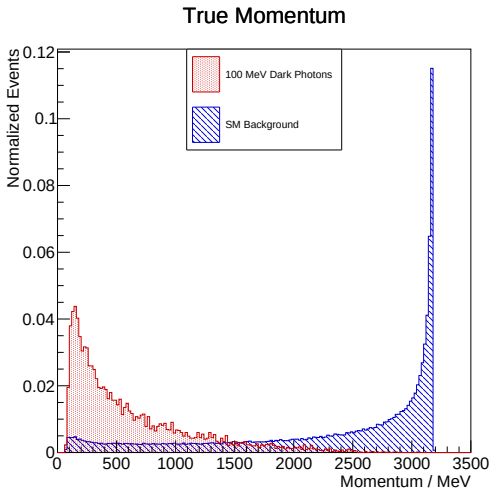

Figure 2.7: Simulated energy distribution for the recoiling electron from a 3.2 GeV beam after passing a $0.1X_0$ target of tungsten. Comparing SM Bremsstrahlung and dark Bremsstrahlung from a 100 MeV dark photon.

2.5 Overview of Possible Background Processes

The effective rejection of background events will be the main driver behind design the considerations of the detector (see also Chapter 3). Thus following the discussion in Section 2.4.4 it is useful to get an overview over possible background processes which could imitate the kinematics of dark bremsstrahlung. These would be events where the recoiling electron would only be left with a small fraction of the initial beam energy and no further particles are detected anywhere in the detector assembly. A non exhaustive overview is given below and also treated in [10].

2.5.1 QED Background Processes

Due to the relatively large cross section, SM bremsstrahlung will be the dominant process. Events where a hard Bremsstrahlung photon carries away most of the beam energy can constitute background events, if the photon evades any detection in the detector. This can happen either if no photon is emitted, or it is emitted, such that it will not intersect any detector components along its trajectory or, it is not detected due to inefficiencies of detector components.

Bremsstrahlung itself can be calculated fairly accurately in QED. The lowest order

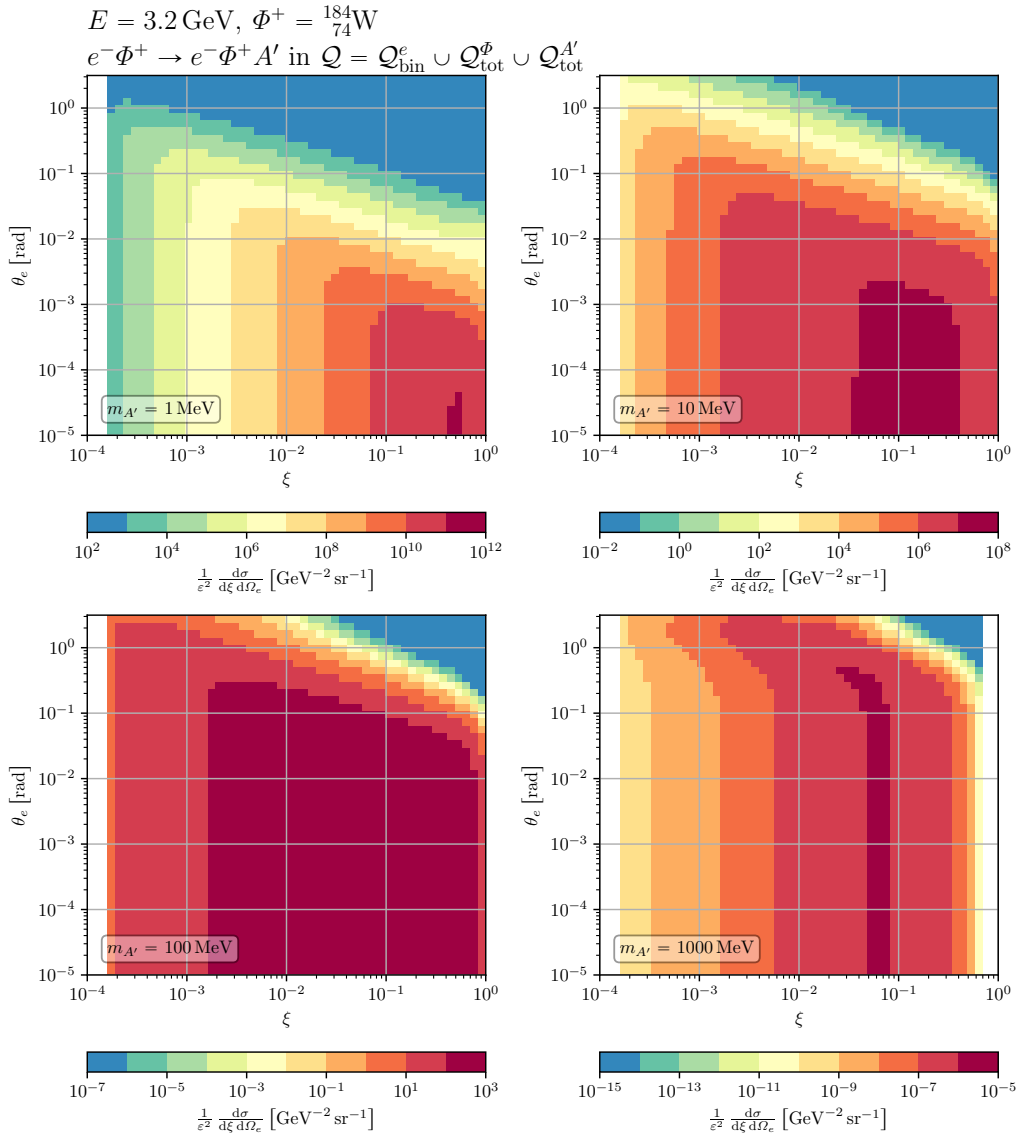

Figure 2.8: Double differential cross section of dark photon production w.r.t. the energy fraction ξ (recoiling electron energy/initial electron energy) and solid angle Ω_e of the recoiling electron. The result is fully inclusive and is shown for four different benchmark masses and normalized by ε^2. Taken from [10] courtesy of Martin Schürmann

process in QED at $O(\alpha^2)$ is

$$e^- + \text{nucleus} \rightarrow e^- + \text{nucleus},$$

which populates the elastic line set by energy momentum conservation [10]. The comparatively large nucleus mass however forces the recoiling electrons to regions high energy final states $\xi \sim 1$, with ξ being the the fraction of remaining electron energy after the interaction. This process will thus not be relevant for this discussion [10]. The leading background process is hence of $O(\alpha^3)$ [10]:

$$e^- + \text{nucleus} \rightarrow e^- + \text{nucleus} + \gamma\,, \text{(with } \xi \ll 1).$$

Corresponding Feynman diagrams are given in Fig. 2.6.

The main concern would be high energy photons missing any detector components, which are called out-of-acceptance backgrounds in the following. It is however well understood as the kinematics for this process can be accurately calculated [10], which will influence the detector design. Nevertheless these events constitute the main background source just due to the relatively large cross section.

2.5.2 Electro-nuclear Interactions

The electron can transfer large amounts of momentum to a nucleus in any detector component. In most of these cases, the respective nucleus will break up and emit one or more nucleons and/or other hadrons with large energy. This can become a problem if the resulting hadrons are not detected and it seems like most of the beam energy is missing in the observed event [10].

2.5.3 Photo-nuclear Interactions

In photo-nuclear reactions, a hard bremsstrahlung photon undergoes an interaction with a nucleus somewhere along its trajectory. Thus not necessarily being detected in the intended detector components. Similar to electro-nuclear interactions, the nucleus is expected to break and emit nucleons and/or other hadrons. The rejection strategies for both electro- and photo-nuclear backgrounds are similar as they rely on measuring the emitted hadrons for forming a veto for the respective event [10].

2.5.4 Neutrino Backgrounds

Neutrinos can also be produced. The key difference to the other backgrounds discussed so far is that this is not a background due to inefficiencies in detector design and instru-

mentation. Neutrinos are essentially invisible to most detector components unless they are highly specialised for that task. As such they can constitute an irreducible background [10, 45].

The neutrino production process with the largest cross section, charged-current electron-nuclear scattering, is not of concern. There is no electron in the final state of this process. It can thus be easily vetoed [45]. Other processes with an electron in the final state are of higher order and have a cross section low enough to not be of relevance for the lumiosities proposed here [45].

2.5.5 Possible Background Final States

A list of energetically possible background events considering a 3.2 GeV beam impinging on a tungsten nucleus has been compiled in Appendix A.2. The table is non exhaustive, but gives an overview over the most basic final events. Background event types which are thought to be particularly challenging are marked in red. The are characterised by containing neutral hadrons since they are usually not able to be measured apart from dedicated detector components like a hadronic calorimeter. These processes play a crucial role in the detector design.

2.6 Experimental Landscape and Existing Bounds

While the theory describing dark photons has been the focus of this chapter so far, an experiment like it is proposed here is expected to have sensitivity to other models as well. The experimental technique itself does not depend on the exact nature of possible DM particles. It is also sensitive (to varying degrees) to other mediator particles (an overview of examples is found in Section 2.3) [10]. These scenarios may include massive particle dark matter [57–59], elastically decoupling dark matter [60, 61], asymmetric dark matter [62, 63], freeze-in dark matter [64–66], axion-like particles [67], $B - L$ gauge bosons [68] and and sterile neutrinos [69].

Existing bounds from experiments have been compiled in in e.g. [9, 79]. A figure from [9] showing limits for dark photons in the direct annihilation scenario from existing experiments and experiments planned until 2026, and relic targets in a parameter space accessible to accelerators like ELSA is given in Fig. 2.9. The values for both α_D and m'_A/m_χ have been chosen to be pessimistic in terms of excluding the phase space with respect to the relic targets [44, 45]. An unexplored and well motivated region for new searches remains. The experimental proposal presented here is thus focussed on reaching this unexplored part.

With the missing momentum technique presented here, overlap in sensitivity is also expected with experiments looking for direct detection of dark sector dark matter like

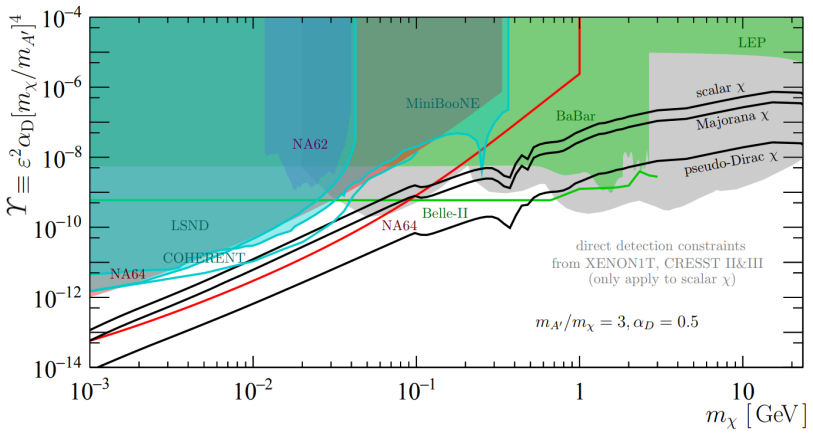

Figure 2.9: Constraints on the dark photon direct annihilation scenario in the $[m_\chi, \Upsilon]$ plane for a fixed ratio of $m'_A/m_\chi = 3$ and $\alpha_D = 0.5$. The fixed parameters are the same as in Fig. 2.5. The figure was slightly adapted from [9]. It includes constraints from existing experiments and experiments planned until 2026. Constraints are set by LEP [70–72], BaBar [73], MiniBooNE [52], NA62 [74], LSND [75], NA64 [49], CRESSTII [76], CRESSTIII [77], XENON1T [78]. Constraints from the latter three experiments only apply to the case of scalar elastic DM.

FUNK [80], and with collider based searches, e.g. at KLOE [81], BESIII [82], LHCb [83–85], BaBar [73], and FASER [86].

Chapter 3

Proposal for Lohengrin

This chapter serves to provide an overview over necessary detector components and their subsequent requirements to detect a possible and well motivated dark sector mediator particle introduced in Chapter 2 with a proposed fixed target missing momentum search experiment called Lohengrin.

This includes an introduction to the accelerator facility ELSA, additional theoretical considerations guiding the proposed design and an overview of the envisioned detector components. Emphasis is put on their role in the analysis chain and an overview of their necessary requirements is given. A similar overview can be found in [10]. The information found there is reordered and summarised in this chapter to better reflect the narrative of this thesis.

3.1 The Accelerator – ELSA

The Elektronen-Strecther-Anlage (ELSA) is an electron accelerator located at the physics institute of the University of Bonn (Physikalisches Institut). A schematic overview of the experimental hall with the beamline situated inside is given in Fig. 3.1. It also includes an overview of different experiments and magnet placement.

ELSA has the potential to provide a relatively clean electron beam with a mean energy of 3.2 GeV and energy spread of 0.8 ‰. ELSA enables the full potential of the proposed experiment as on average single electrons (see Section 3.1.1) per event can be extracted from the ring. This provides a uniquely well defined and clean initial state potentially allowing for minimal instrumentation at the front of the experiment.

A previous analysis of the optics of the test beamline at ELSA [88] revealed, that a reasonable approximation for the beam spot at the site of the target would be a Gaussian profile with a standard devation of 1 mm in both lateral dimensions and a divergence of less than 0.8 mrad in both dimensions [10].

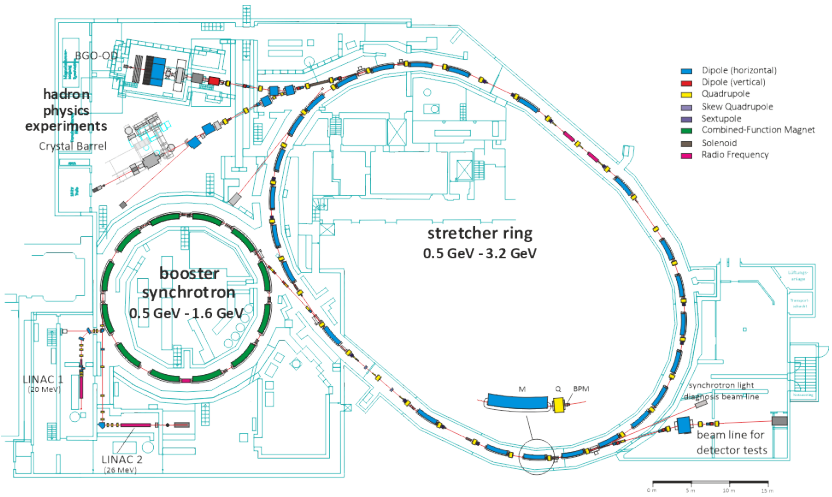

Figure 3.1: Schematic overview of the ELSA accelerator in the experimental hall at the Bonn physics institute. Different experiments and magnet placement are indicated. Taken from [87].

At ELSA electrons are extracted from their respective bunches by resonant extraction. This is a very controlled process which allows for the extraction of on average single electrons. Due to the importance of a clean initial state to the LOHENGRIN experiment, this process is explained in more detail below.

3.1.1 Resonant Extraction

The overview given here is based on the one provided in [17]. A detailed discussion can be found in e.g. [89, 90].

The normalised coordinate system for accelerators is given by a horizontal coordinate X defined perpendicularly to the beam axis, a corresponding vertical coordinate Y and a phase along the beamline μ. Primed versions of these coordinates indicate derivatives with respect to μ. The phase μ increases by $2\pi Q$ for each revolution, where Q is known as betatron frequency. For extraction, ELSA is driven at Q close to 14/3 [87].

Trajectories in the accelerator can be plotted in the X-X' plane. For stable trajectories the result is a circle. However if a sextupole field is introduced, this shape changes at the sextupole position. Depending on the strength of said sextupole field, the particles begin to trace out a triangular shape as seen in Fig. 3.2. The emerging triangle also defines sets of parameters with stable trajectories (Fig. 3.2(a)) and appears for particles close to a resonance with three in its denominator. The shape is outlined by so called separatrices. Particles with a parameter set within the separatrices are on stable trajectories

(Fig. 3.2(b)), while particles situated outside will move away from the main beam axis with each revolution (Fig. 3.2(c)) [89]. The size of the stable region can be finely tuned with the sextupole field and by changing how close the betatron frequency is to the resonance [89]. This allows for a precise control and selection of few particles with a well defined momentum.

Particles with a sizeable distance to the main beam can then be finally extracted and ultimately be guided to the site of an experiment with a septum magnet as depicted in Fig. 3.3 [90]. A dipole field in a localised region is used for this purpose.

Using this technique allows to extract on average single electrons at ELSA with a rate of 100 MHz. More specifically, the spacing at ELSA is 2 ns with an average extraction of 0.2 electrons following a Poisson distribution. A corresponding plot of said Poisson distribution is given in Fig. 3.4. These parameters yield the average numbers given previously. Given this configuration, more than one electron is only extracted with a probability of 1.75 % and exactly one electron is extracted with a probability of about 16.4 %.

3.1.2 Possible Dark Photon Production at ELSA

Given the parameters of ELSA with a beam energy of 3.2 GeV and an average electron extraction rate of 100 MHz, it is possible to take a look at the number of dark photons which could be produced in a given time frame. Assuming a tungsten target with a thickness of 0.1 X_0 ($\approx 0.35\,\mathrm{mm}$), the number of expected dark photons can be calculated based on the production cross section for dark bremsstrahlung given the parameters above.

The number of events with at least one dark photon in the final state for different dark photon masses and number of electrons on target (EoT) is given in Fig. 3.5. Only electrons going in the forward direction after interacting in the target are taken into account. The number of events is normalised by ε^2 as this parameter is not fixed.

Assuming dark photons masses in the range of 10 to 100 MeV and couplings between the SM and dark sector at strengths necessary to account for the relic targets (see Fig. 2.9) one would expect between one and 100 signal events for 4×10^{14} EoT [10]. The actual number with this set of parameters can also be higher given that the relic targets provide lower bounds for the coupling. The mentioned number of EoT can be achieved within about one year of runtime at ELSA considering a baseline rate of 100 MHz, the duty cycle and limited beam time. ELSA is able to provide single electrons at a higher rate, the baseline rate however is used for the remainder of this thesis. This baseline already poses a challenge considering the timing of required sub-detectors [10]. A lower rate would delay the conclusion of the experiment with the envisioned number of EoT.

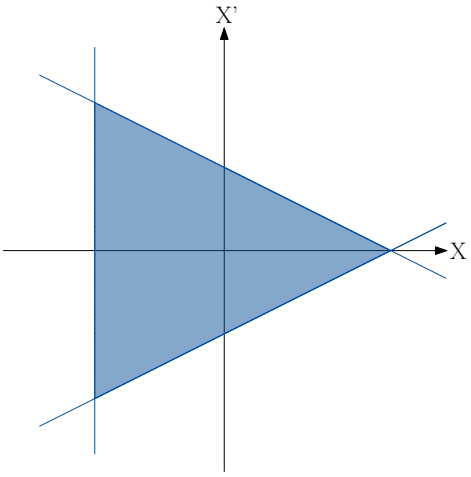

(a) Taken from [17].

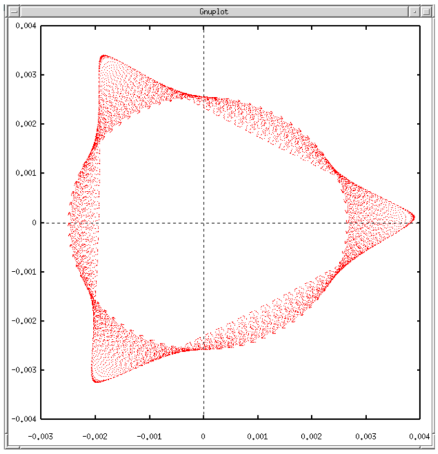

(b) Taken from [89].

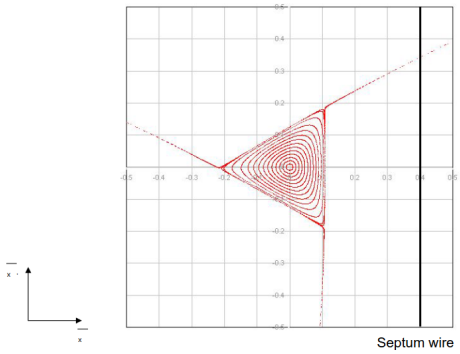

(c) Taken from [91].

Figure 3.2: Visualisation of resonant extraction. (a): Visualisation of Separatrices. Particles inside the shaded region are on stable trajectories. Particles outside of that region will move away from the main beam with each revolution in the ring. (b): Particle trajectory in an increasing sextupole field. The strength of the sextupole field is increased slowly (compared to the revolution time of the accelerator). The transition from circle to triangle can be nicely seen. (c): Trajectories with unstable particles. The increasing distance from the main beam axis is visible.

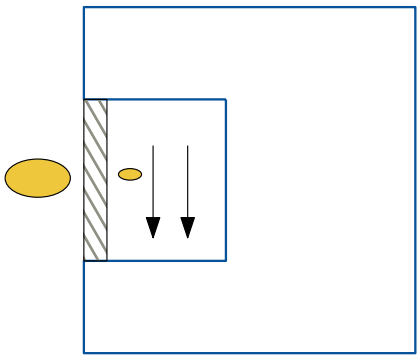

Figure 3.3: Visualisation of how electrons with a sizeable distance from the main beamline can be finally extracted to an experimental site with a septum magnet. Black arrows indicate the direction of a magnetic dipole field. Taken from [17].

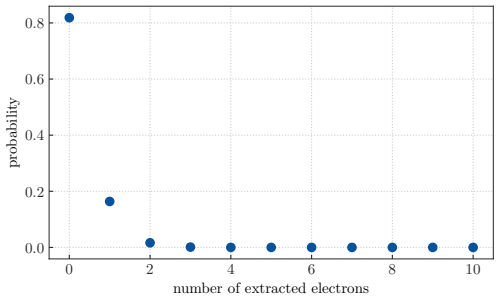

Figure 3.4: The probability to extract different numbers of electrons per event. More than one electron is only extracted with a probability of about 1.75 %.

3.2 Additional Theoretical Principles Guiding the Experimental Design

As already mentioned in Section 2.5, the dominant background process is SM Bremsstrahlung which can be accurately calculated. The dark photon production cross section can also be theoretically calculated given the Lagrangian in Eq. (2.8) and the beam parameters at ELSA. This makes it possible to theoretically look at interesting areas in the phase space a missing momentum search experiment should be optimised for, in order to maximise the potential for discovery.

Following the discussion in Section 2.4.4, this area should be situated at low recoil electron momenta and moderate scattering angles. This is verified by the results in [10]. Here the cross sections for SM Bremsstrahlung and dark photon production are normalised by ϵ^2 and used to obtain a rough idea on a potential value for $S/\sqrt{B}$. The

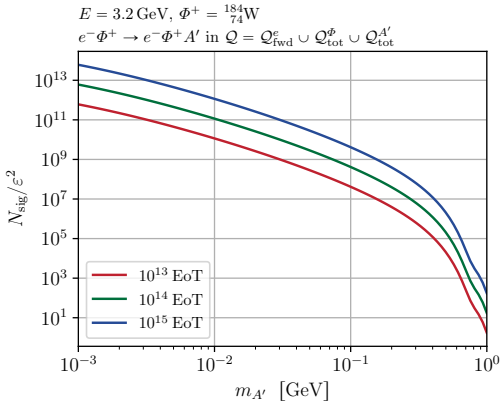

Figure 3.5: Number of signal events (events with a dark photon in the final state) N_{sig} for different dark photon masses and number of electrons on target (EoT). The number is normalised by ε^2 as this is a free parameter of the theory. Only final state electrons going in the forward direction after interacting with the target are taken into account. Taken from [10].

result is shown in Fig. 3.6 for different dark photon masses.

It has to be noted, that this assumes a perfect tracker as the values on the x-axis are showing the fraction of incoming momentum remaining in the recoiling electron, is a truth value. It also assumes some form of perfectly working calorimeter which is able to veto any events in which a photon is emitted within 0.1 rad of the beam axis as a background event. Photons emitted at larger angles are not detected and thus such events are classified as signal given the correct kinematics.

While this is a very crude approximation in many aspects, e.g. completely ignoring most detector effects, it is still useful to obtain an idea about the phase space, which is interesting for a missing momentum search experiment. This also outlines the goals for the design of Lohengrin: The detectors must be able to cope with incident electrons at a rate of about 100 MHz and do so at a high efficiency. There has to be some kind of tracking system which is able to accurately measure electron momenta down to a few MeV at moderate scattering angles. A calorimeter system is needed to detect SM photons created in the target. Since this discussion only takes QED backgrounds into account, additional veto systems will be needed to deal with so far neglected backgrounds.

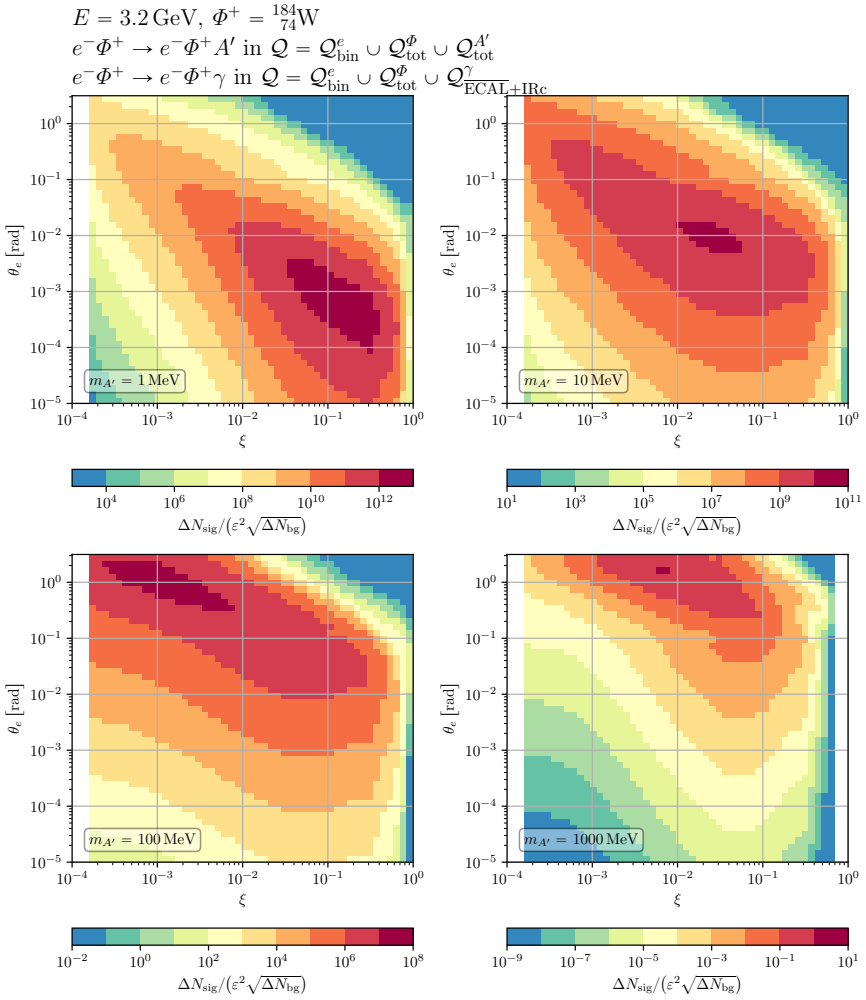

Figure 3.6: Expected sensitivity $S/\sqrt{B}$ for $\varepsilon = 1$ for four different dark photon masses as a function of the recoil electron energy and scattering angle. Taken from [10].

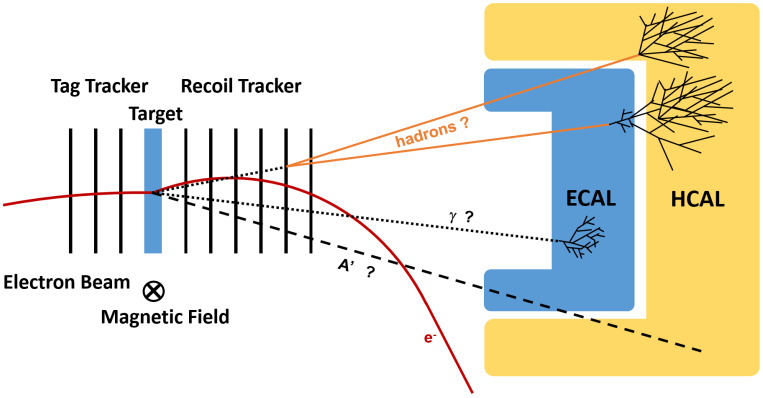

Figure 3.7: Schematic of the proposed detector setup for LOHENGRIN. The main sub detectors are (from left to right): the tagging tracker, the recoil tracker, the electromagnetic calorimeter, and the hadronic calorimeter. The trackers are embedded in a magnetic field enabling the momentum measurement for traversing electrons. Taken from [10]

3.3 Overview of the Proposal

As already introduced in Chapter 2, the idea behind LOHENGRIN is to find dark sector mediator particles with a missing momentum technique. General principles defining the main parameters concerning the design are given in Section 3.2. The general concept is summarised in Fig. 3.7. The two trackers (tagging and recoil trackers) are situated within a permanent magnet providing a nearly homogenous field along the negative y-axis deflecting electrons towards the positive x-axis. The mean of the incoming electron beam hits the target perpendicularly. The direction of motion at the location of the target defines the positive z-axis. The magnetic field allows for momentum reconstruction through the tracking layers. The electromagnetic calorimeter ECAL covers a large fraction of the solid angle opened up at the end of the magnet allowing the measurement of mainly final state photons. The hadronic calorimeter HCAL surrounds the ECAL and is used to veto events with hadrons in the final state.

For an additional overview, a three dimensional rendering of the setup described in Fig. 3.7 is shown in Fig. 3.8.

3.4 Detector Components and their Purpose

This section will give a more detailed description of the individual detector components and introduces the critical requirements and considerations which have a major impact

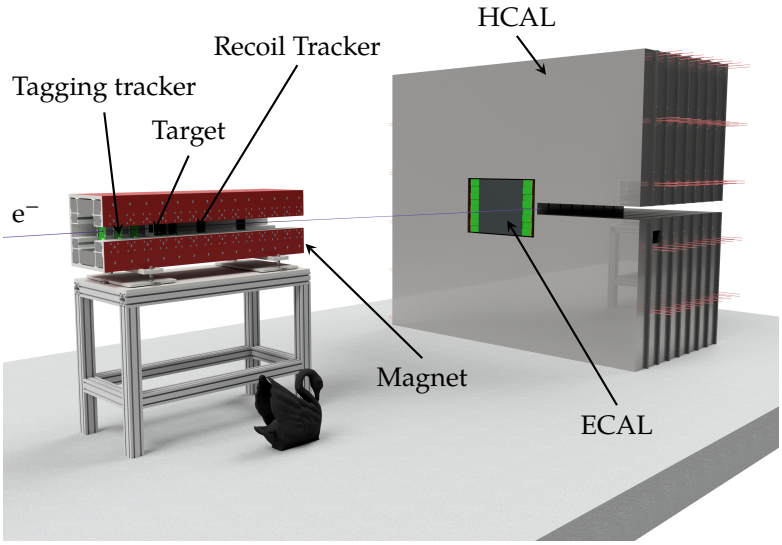

Figure 3.8: CAD rendering of the proposed detector setup for LOHENGRIN. It consists of the tagging tracker, target and the recoil tracker inside the magnet and also the electromagnetic calorimeter (ECAL), hadronic calorimeter (HCAL) towards the rear. The path of the non interacting electrons is indicated in purple. Cygnus atratus is added for size comparison. Taken from [10]

on the entire detector design.

3.4.1 Target

The target is situated inside a homogenous magnetic field and serves the purpose of generating signal events via dark Bremsstrahlung (see Section 2.4.3). It is supposed to be a 0.1 X_0 sheet of tungsten striking a balance of production cross section and unwanted effects such as regular Bremsstrahlung with high energy photons in the final state.

Tungsten is chosen as a baseline material, because it has a short radiation length and thus allows for a physically thin target. There are also some simplifications regarding the modelling of (dark) Bremsstrahlung: The main isotope of tungsten is a scalar nucleus which, in a first approximation (such as e.g. in Appendix A.1), allows for a rather simple interaction Lagrangian.

Other materials for the target are not studied in this thesis, but such investigations regarding the number of background events with hadronic activity in the final state have been done [10] in the scope of a master's thesis by Laney Klipphahn.

3.4.2 Trackers

Tagging Tracker

The tagging tracker is situated in front of the target inside a magnetic field. It is not supposed to facilitate a platform for electron momentum measurement as the beam from ELSA has a very well defined initial state. Any feasible measurement would be more inaccurate than the beam parameters given a well adjusted beam. It will therefore only consist of at most a few layers which will not be enough for an accurate momentum measurement. In the current proposal, three of those layers are included. They are used to determine the presence of an electron from the extracted beam and the number of extracted electrons. It is also used as an additional component able to veto events which might undergo hard bremsstrahlung, either in the medium before interacting with the target, or in the tagging tracker itself. Such events can be discarded due to their deviation from the expected path of beam electrons.

The requirements on this detector are nevertheless challenging. It has to deal with a high hit rate of approximately 100 MHz in a relatively small area as the beam is focussed on the target. Furthermore incoming electrons should be tagged with an efficiency of close to 100 % in order to avoid large losses in the form of effective luminosity requiring a longer runtime of the experiment.

Recoil Tracker

The recoil tracker is situated inside the magnetic field, but placed behind the target. It is used to facilitate an accurate momentum measurement. It will therefore consist of more layers than the tagging tracker. The main analysis strategy focuses on finding events with low momentum electrons behind the target and no other particles present. It thus has to work in tandem with the calorimeters for an efficient event veto.

In addition to the requirements placed on the tagging tracker, it has to provide an accurate momentum measurement over a large range of about 25 to 3 200 MeV. The tracker cannot be optimised to provide an accurate measurement over such a large range due to different requirements on lever arm, field strength and individual tracker placement. It has to be optimised to accurately reconstruct electron momenta to the lower end of this range in order to not falsely classify potential signal events. For electrons of about several hundred MeV, a high tracking efficiency is more important and sufficient to veto high energy events.

The material budget needs to be as small as possible as the accuracy of the momentum measurement is dominated by multiple scattering. A thin detector is thus critical to fulfil this requirement. For the reasons stated above, depleted monolithic active pixel sensors (DMAPS) such as the TJ-Monopix2 ASIC [92, 93] are considered as a baseline for the

geometry. They feature square pixels with a pitch of $33.04 \times 33.04\,\mu m^2$ in a matrix of 512×512 pixels. Each layer of the tracking detector can then be constructed out of four such ASICs covering a reasonable area. It has to be noted that ultimately a new ASIC has to be developed for LOHENGRIN. The shaping time of the TJ-Monopix2 is probably too long and has to be reduced for a successful execution of LOHENGRIN. The required modifications however should in principle be possible at the cost of energy and timing resolution [10]. Assuming this can be done, a suitable configuration would be a linear shape for the measured signals with a peaking time of 5 ns and a return to baseline within 95 ns after peaking. In this case the estimated single hit efficiency would be 99.86(5) % [10].

3.4.3 Electromagnetic Calorimeter

The ECAL serves as a pure veto detector. It is supposed to veto events which contain a high energy photon in the final state. Such events would produce low energy recoil electrons. Not registering the high energy photon could thus contribute significantly to background being falsely classified as signal events. It therefore must be able to accurately measure a large amount of energy being deposited by single photons over a constant background of events hitting the ECAL. It should also cover a decent solid angle in order to miss as few photons as possible to further reduce falsely classified background events[1]. Furthermore the ECAL has to be sufficiently radiation hard, still properly performing after $\geq 10^{14}$ EoT.

These requirements are very challenging considering the 100 MHz baseline rate. For this reason, the total magnetic bending power, the distance to the target and the angular size of the ECAL are chosen particularly such that the main electron beam misses the ECAL. This is achieved by placing it 3.5 m behind the target and using an active area of $48 \times 48\,cm^2$ [10]. Bending the main electron beam away severely simplifies the reconstruction of photons: Most electrons do not lose a significant amount of energy in the target and will thus be roughly deflected by the same amount. Also considering the small beam spot at the target, the main electron beam would mostly hit the same few ECAL cells, making an event based energy measurement extremely challenging[10]. Bending the main beam around the ECAL eliminates a lot of complexity and allows to solely focus on the reconstruction of photon energies. One implication of this choice is that the trackers provide the only information on the electrons in an event, underlining the importance of accurately reconstructing electrons with high efficiency.

[1] This type is called out-of-acceptance background

3.4.4 Hadronic Calorimeter

Similarly to the ECAL, the HCAL is used as a veto in the experimental strategy. It does not have nearly as strict requirements on the rate capability and energy resolution as the ECAL. Any event which produces a hadron in the final state did not only undergo dark Bremsstrahlung and can thus not be considered as a signal event. The HCAL hence only needs to cover large solid angle detecting any hadron in the final state with a high efficiency at low noise levels. An accurate energy measurement is not required for a pure veto approach. The horizontal slit depicted in Fig. 3.8 is required due to the path chosen for the electrons. The main electron beam is bent around the ECAL and would thus hit the HCAL depositing their entire energy. This would contradict the intended use as a veto detector registering only final state hadrons. The slit allows electrons to pass through without interacting.

3.4.5 Magnet and Magnetic Field

The magnetic field is required for an electron momentum measurement. A simple dipole field running along the y-direction is sufficient and can be realised with a permanent magnet eliminating all of the added complexity when operating superconducting magnets. The total bending power of the magnet and the size and distance of the ECAL to the target are chosen such that the main electron beam misses the ECAL. As a baseline approach, a magnet with a strength of 0.9 T over a length of 1 m after the target fulfils this requirement (see Fig. 6.2). The length behind the target is given, because the electron beam is adjusted such that it will hit the target perpendicularly. The diameter of the inner cavity is foreseen to be 20 cm. Along with the length of 1 m, this creates an opening angle (measured from the target) of 0.1 rad.

The magnet features an opening on the side electrons are deflected to, creating a c-shaped bore. This allows also low energy electrons from hard bremsstrahlung events to leave the assembly uninterrupted without creating secondary particles in interactions with the magnet bore.

Chapter 4

Simulation Framework – ExPlORA

This chapter gives a brief overview over the ExPlORA simulation framework used for this thesis. It will go over an example showing how detector geometries can be built and how this can then be used for a simple analysis with export of data.

4.1 Overview

ExPlORA (Extended PLuggable Object-Oriented Rootified Analysis) has originally been developed for the CBELSA/TAPS collaboration for use in the corresponding experiment [94]. A version of it was forked for the BGO-OD experiment in 2011. This version was then finally used in [17] for the first iteration of a detector simulation. The work in this thesis is based on the continued development of that version. The BGO-OD version of ExPlORA already contained a working detector simulation for the BGO-OD experiment at ELSA. Large amounts of code could be reused for [17] as it provided a base for the start of a simulation framework.

One unique feature of ExPlORA is that it can be used as a framework for both simulation and physics analysis. An application is configured via a markup language describing both the simulation setup and potential analysis of the raw data. This removes the need to recompile the entire code base in case a simple modification is made to the setup. The physics analysis is able to use ROOT, while event by event simulation is performed using Geant4 combining two powerful and widely used packages across high energy physics.

4.1.1 ROOT

ROOT is an open source software framework developed at CERN. It can be used to e.g. store, retrieve and analyse large amounts of data. Extensive plotting capabilities are also supported. It is used in the analysis workflow of many high energy physics experiments such as ATLAS and CMS [95]. A complete and extensive overview would be beyond the scope of this thesis. More information can be found on the official webpage [95].

For the results in this thesis it is mainly used for storing and retrieving data and simulation results, analysis with standardised classes and formats as well as describing the detector geometry. The integration of ROOT into ExPlORA simplifies the interaction with Geant4 for these purposes.

4.1.2 Geant4

Geant4 is a toolkit to create simulations of the passage of particles or radiation through matter [96]. It provides a complete set of tools for detector simulation. As is the case for ROOT, a complete and thorough description is beyond the scope of this thesis. More information can be found on e.g. the official website [96] or the book for application developers [47].

The toolkit is able to accurately simulate the traversal of particles through matter using Monte Carlo methods. This includes a representation of the detector geometry, the associated materials, response of sensitive detector components, interactions with electromagnetic fields, etc. It can be used to direct single electrons on a tungsten target and obtain results on their interaction within the target and interactions of recoiling electrons in the detector assembly.

4.2 General Simulation Architecture

4.2.1 Organisation into Plugins

ExPlORA is written in C++ and organised into individual modules referred to as plugins. It makes extensive use of the object-oriented nature of the language. Each plugin generally serves one specific task. This can be a plugin which only implements data structures to store information on specific parameters for the geometry of one detector component, or something much more complicated like a clustering algorithm. Plugins can be invoked at any point in the simulation. The programmer can specify which parameters of each self written plugin should be configurable via an XML file. This allows for flexibility in changing key parameters of the simulation e.g. detector placement, magnetic field strength or beam energy without having to recompile the entire project.

Since everything is configured via XML files, plugins can also be called from XML files of other plugins. This naturally leads to a hierarchical structure: One master XML file is passed to ExPlORA at runtime which sequentially includes the entire description of the application.

4.2.2 Data Transfer between Plugins

The process described above can only work if data can be exchanged between plugins. In ExPlORA this is achieved via containers. Containers are specific classes created to hold data. They are uniquely identifiable by their name given to them in the XML configuration. The data inside a container is basically arbitrary and can be used for whatever is benefitial to the goal of the user. An example of this is a digitizer plugin of a pixel detector which creates a custom hit object. This hit can then be used by e.g. a clustering plugin for further analysis. It could contain information on the hit location, time, amount of energy deposited and the detector component being hit.

These classes should ideally be generic such that they can be used for multiple plugins by using the inheritance feature of C++. Another advantage of this approach is that already written analysis plugins can be used with either simulated or measured data, provided the data is internally handled in the same format and with interchangeable classes.

4.2.3 Simulation

Once everything is configured, ExPlORA can be used for a full detector simulation of the described setup. It uses Geant4 for Monte Carlo simulation of particle interaction with the detector components. User generated plugins are then required to turn the results of Geant4 into digitised data of the detector and run further analysis. Each event is simulated individually. In order to reach the desired statistical significance or luminosity, one has to run the appropriate number of events.

It has to be noted that ExPlORA can also specifically be used solely for analysis of data. The Monte Carlo simulation can be turned off and the program can also be run with previously generated or measured data provided that the plugins used for both parts are written such that the data can be seamlessly read in and transferred between plugins.

4.3 An Example

Section 4.2 gave a general explanation on how to set up a simulation application with ExPlORA. This section provides a simple example and shows how to actually implement the ideas above. It shows how to place the target in simulation, set up an electron beam and finally save some useful data. Detailed code listings are not provided and omitted where appropriate. However key steps in how to set up the simulation are given. The ExPlORA source code for the Lohengrin project can be found on the university's bitbucket server: [97].

ExPlORA is called by using the console command *explora simulation_DM.xml*. Where *simulation_DM.xml* is the master file setting up the key parameters and setting up the chain calling all of the needed plugins. An exemplary excerpt of the file is included in listing 4.1. It shows some key concepts.

CBTGeant4MC sets up the key parameters for the usage of Geant4, where *CBTGeant4MC* is its own plugin interacting with Geant4 and being designed such that it can be called with the parameters given in the listing. Some examples are the possibility to disable multiple scattering (*multiplescattering*) in certain materials (*changedphysicsmedia*) or the possibility to export the detector geometry (*savegeometry*) by providing a command line argument.

```
<CBTGeant4MC
   detailedmode="${DetailedMode}"
   debug="0"
   changedphysicsmedia="Silicon,Polyethylene"
   multiplescattering="true"
   montecarloinfoclass="BTMonteCarloInfo"
   savegeometry="${SimulationExportGeometryToFile}"
   savegeometryallformats="${SimulationExportGeometryAllFormats}">
  <![CDATA[
   /mcVerbose/all 0
   /mcEvent/printMemory false
]]>
 </CBTGeant4MC>
 <CBTIncludeXML
   file="./../simulation/DetectorGeometry.xml"
   />
```

Listing 4.1: Exemplary excerpt of a of an ExPlORA master XML file. The complete file is purposefully not listed. This helps to undertsand and underline some key concept in the usage of ExPlORA.

The other key concept which can be seen here is the usage of *CBTIncludeXML*. This is used to include other XML files and can be used recursively to set up the entire application. In this case it is used to include the detector description, which in case of this example, is just the target.

4.3.1 Building Detector Components

Detector components are configured and built across two XML files and usually have two classes/plugins associated with them: One detector geometry data class and one builder class. The data plugin holds all of the parameters necessary to describe the respective detector part. The builder plugin then uses this data to construct and describe the actual component using the ROOT geometry interface. For the simple case of the target, an example can be found in listings 4.2 and 4.3.

```
<BTSolidBoxGeometry
  debug="0"
  name="Target"
  detector="target"
  boxlength="13"
  boxwidth="13"
  boxheight="0.03504"
  origin="(0,0,200)"
  material="Tungsten"
    />
```

Listing 4.2: Exemplary target data description in ExPlORA. Since the target is just a sheet of tungsten, it can be fully described by a simple box.

```
  <BTSolidBoxGeometryBuilder
  detector="target"
/>
```

Listing 4.3: Exemplary target geometry builder description in ExPlORA. It uses the *detector* attribute to obtain all of the necessary construction information from the gemeotry data plugin.

The target is a tungsten sheet of 0.1 X_0 and can be fully described by a box. Hence the geometry data plugin holds information about the side lengths in cm, the material, and the position to place the box's centre (*origin*). It is also possible to provide a set of Euler angles to describe a possible rotation. If no angles are given, the parameters *boxlength*, *boxwidth* and *boxheight* correspond to the measurement along the x-, y- and z-axis respectively. The content of *detector* is used to match the geometry data to the appropriate geometry builder. The *name* attribute is used for formatting debug output on the console.

This is all which is needed to construct the target in ExPlORA. Fig. 4.1 shows a rendering of the geometry in this case. It shows what is to be expected: A thin sheet of tungsten surrounded by nothing.

4.3.2 Particle Cannon

The next step is the introduction of beam electrons. This is realised with a particle cannon. The cannon is essentially a plugin which takes parameters about the beam and places single electrons with the correct momentum and direction into the simulation, where Geant4 can do the remaining transport and interaction with material.

An example for this is given in listing 4.4. The electron is placed at *electronradiatorposition*, which in this case is directly in front of the target. The opening angle of the beam can be configured with *electronbeamdivergencex* and *electronbeamdivergencey*, where ExPlORA expects the final value to be in mrad. For each electron the respective opening angles are sampled according to a Gaussian distribution with standard deviations given by parameters for

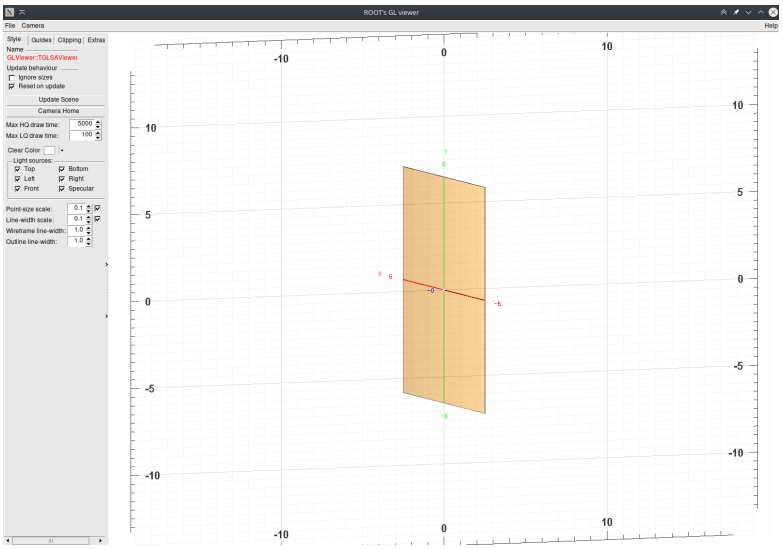

Figure 4.1: The constructed target in ExPlORA with a software which allows for the rendering of the configured geometry.

the beam divergence. Similarly the energy of the electron is sampled according to the probability density function (PDF) described in *BTNumberGenerationFormula*. This theoretically allows for any arbitrary PDF to be included when sampling the electrons. In this case a Gaussian has been chosen. The *ElectronBeamEnergy* and *EnergyDeviation* are defined elsewhere and set to 3 200 MeV and 2.56 MeV (corresponds to 0.8 ‰) respectively.

```
1  <BTVirtualMCElectronBeamGenerator
2    electronradiatorposition="(0,0,199.5)"
3    electronbeamdivergencex="0.0458 * TMath::DegToRad() * 1000"
4    electronbeamdivergencey="0.0458 * TMath::DegToRad() * 1000"
5    generatedparticlecontainer="generatedparticles">
6   <BTNumberGeneratorFormula
7      name="Energy"
8      formula="1/(2.5066*${EnergyDeviation})*exp(-(x-${
           ElectronBeamEnergy})^2/(2*(${EnergyDeviation})^2))"
9   min="${ElectronBeamEnergy}-40*(${EnergyDeviation})"
10  max="${ElectronBeamEnergy}+40*(${EnergyDeviation})"
11  />
12 </BTVirtualMCElectronBeamGenerator>
```

Listing 4.4: Example of the description for a particle cannon in ExPlORA. It uses information of the beam parameters to generate electrons at place them into the Geant4 simulation.

Created electrons are placed into the *generatedparticles*. This allows for the exchange of data between plugins. Once all parameters are set, single electrons are placed into the simulation and then propagated through the detector geometry with particle interactions simulated by `Geant4`.

4.3.3 Data Export

The last step for this example is the export of interesting data for further analysis. In this case a plugin was written which uses the container of all Monte Carlo tracks as input. These contain the full truth information of any particle generated during an event. A fictitious layer can be placed and the full kinematic information of any particle passing this layer is extracted from the Monte Carlo track container and saved in a `ROOT` tree. This is done by just creating and then writing the relevant data into the `ROOT` file in the `C++` source code of the plugin.

This fictitious layer is placed 3.5 m behind the target. It is now possible to record the positions of scattered electrons and generated Bremsstrahlung photons at this distance. One would expect a very simple broadened distribution around the centre as the photons are created mostly collinearly and the electrons are not deflected due to the inexistence of a magnetic field in this example. The distributions for 5×10^5 EoT are displayed in Fig. 4.2. This is exactly what is seen.

It has to be noted that the setup for this example was deliberately chosen to be simple and as such the result is easy to predict. It does however provide an intuitive overview on how `ExPlORA` and the underlying simulation works and can produce results for further analysis. This general workflow in setting up the simulation will be used for the remainder of this thesis.

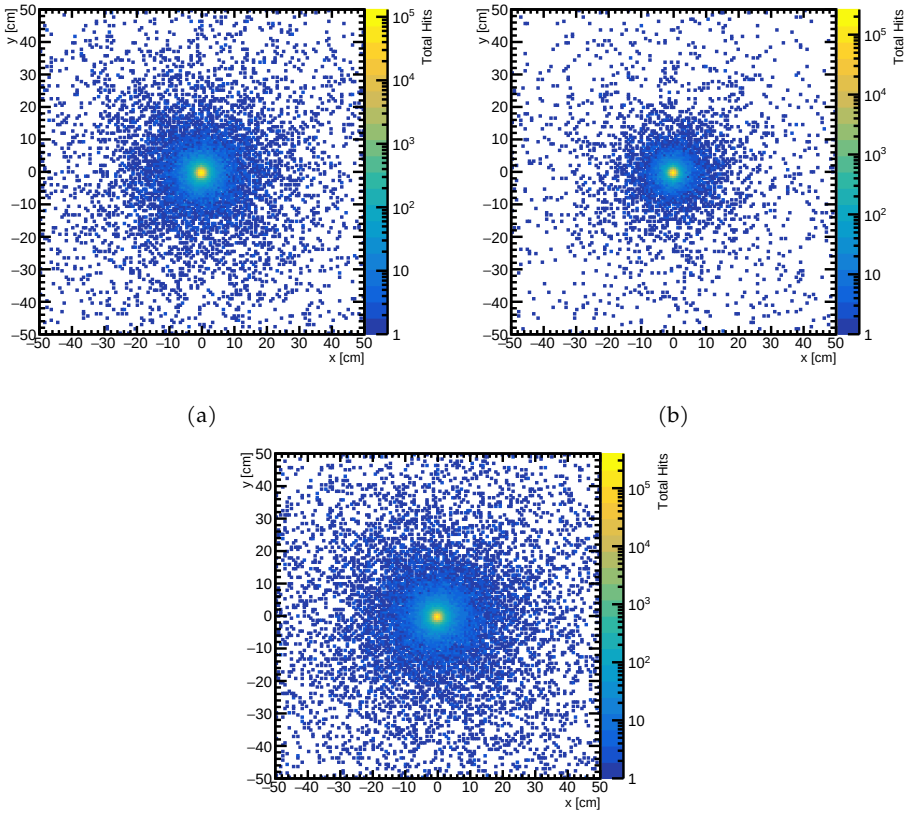

Figure 4.2: Hit distribution of electrons and photons 3.5 m behind the target with just the target constructed for 5×10^5 EoT. (a): Only electrons shown. (b): Only photons shown. (c): All hits of electrons and photons shown.

Chapter 5

Proposal for a L0 Trigger

As already mentioned in Chapter 3, the potentially high hitrate poses a significant challenge for the success of the experiment. It is therefore necessary to implement a system which is able to efficiently select interesting events, while reducing the overall rate by about a factor of 100 to 1 MHz. The trigger system is proposed and explained in [10]. It is however summarised here for completeness. Additional information is provided where appropriate.

5.1 Overview

The rate reduction is done in a two-stage process. The first stage of this system is referred to as L0 trigger. The second stage is foreseen to make a selection based on machine learning techniques implemented on FPGAs currently being investigated in the scope of a PhD thesis by Patrick Schwäbig. The goal of the first stage is to reduce the event rate by a factor of $\sim$ 10 to 20.

The kinematics of the recoiling electron, which should pass the L0 trigger, can be obtained from Fig. 3.6: The trigger mainly needs to select electrons at low energy with high efficiency and accuracy. This has to be done at the baseline rate of 100 MHz. It is understood, that this poses a significant challenge on the hardware side. The proposed trigger makes use of the relatively fast pixel trackers. The ASICs can be configured to provide a hit-or signal in a specified region of the sensitive area. Due to this being a relatively simple operation it should be considerably faster than an accurate position measurement. The idea is that a certain ASIC would provide a high signal after a hit is registered in a specified region. The signal can then be reset to low after e.g. 2 ns [10]. It is however understood that the implementation of such a signal over the full pixel matrix is challenging. The following considerations assume that such a signal can be implemented sufficiently fast to cope with electrons every 10 ns [10].

5.2 Tracker Placement and Trigger Algorithm

5.2.1 Tracker placement

Since the triggering algorithm uses the hit-or signal of the tracking layers, their positioning plays a vital role. Table 5.1 lists the z-coordinate (axis along the beam direction) of the target and the tracking layers behind the target.

Layer	Target	1	2	3	4	5	6	7	8	9
z Position [cm]	200	181	184	190	201	203	204.5	207	210	213

Table 5.1: Positions of the middle of the tracking layers as well as the middle of the target for the LOHENGRIN detector geometry. Note that for the trigger considerations in this chapter, only the trackers behind the target (i.e layer 4 and onwards) are relevant.

5.2.2 Triggering Algorithm

The algorithm needs to be simple in order to be quickly processed. As already stated, the triggering system should select low-energy electrons. Fig. 5.1 shows the rate of events with any number of electrons, where the leading electron has a maximum energy of $E_{e,\mathrm{cut}}$. Designing an algorithm that will select for electrons with an energy below 150 MeV should fulfil the above requirement in terms of rate reduction. This includes a margin of safety considering a transition region where the trigger will have varying efficiencies.

The proposed algorithm uses the horizontal deflection of low-energy electrons in the magnetic field. An event passes the trigger if:

- a hit is registered anywhere on plane 4 AND
  - a hit is registered on plane 5 with $x > 1.99\,\mathrm{mm}$ OR
  - a hit is registered on plane 6 with $x > 2.3\,\mathrm{mm}$ OR
  - a hit is registered on plane 7 with $x > 3.1\,\mathrm{mm}$
- AND no hit is registered on plane 9.

The efficiency of such a trigger will depend mainly on the final state electron energy by design. However it will also depend on the electron's position emerging from the target as well as the polar angle (θ_e) and azimuthal angle (ϕ_e). Assuming a Gaussian beam spot with a lateral size of 1 mm in both x and y on target, it is possible to simulate the trigger efficiency for SM events. Taking the considerations from Section 3.4.2 into account,

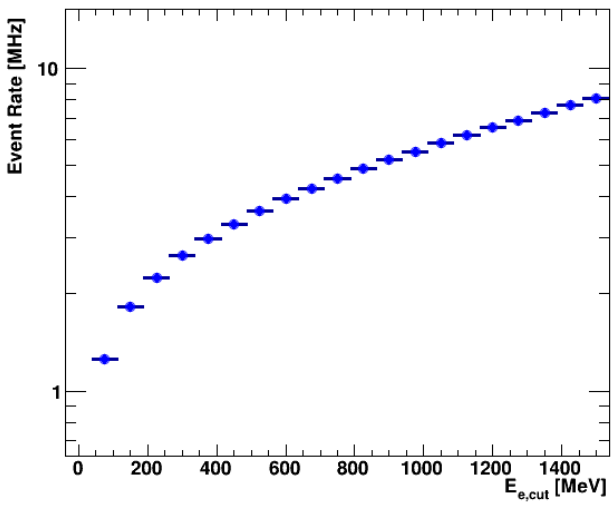

Figure 5.1: Event rate for different maximum energies of all electron(s) in the final state for SM bremsstrahlung events. Taken from [10].

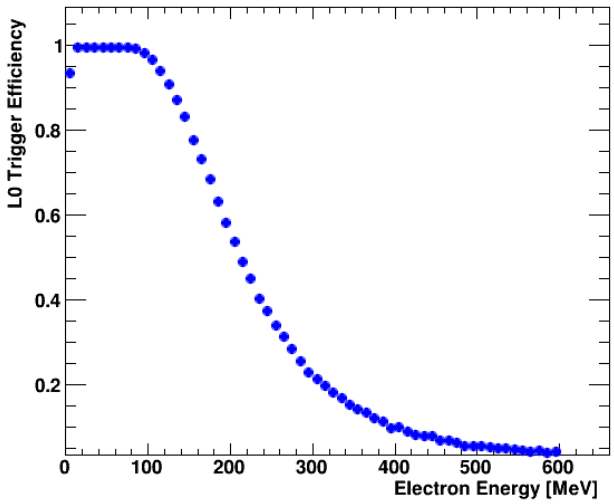

Figure 5.2: Efficiency of the proposed L0 trigger as a function of the electron energy, assuming $\theta_e < 0.05$. Taken from [10].

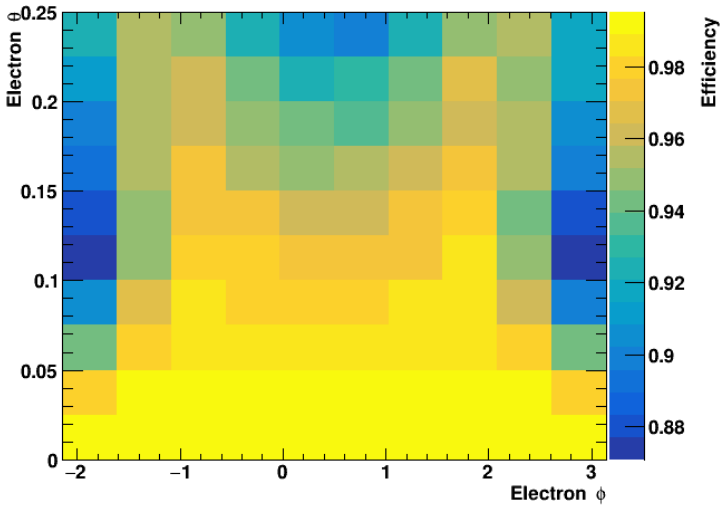

Figure 5.3: Efficiency of the proposed L0 trigger as a function of $\theta_e < 0.05$ and ϕ_e for $E_e < 100\,\text{MeV}$. Taken from [10].

a single hit efficiency of 99.5 % is also used. The result of this can be seen in Figs. 5.2 and 5.3.

For final state electrons below 100 MeV an effciciency of about 99 % is achieved[10]. The efficiency begins to decrease for electrons above that energy. The total event rate is reduced to about 3.7 MHz.

The origin of the unique structure in Fig. 5.3 is a combination representing the cartesian cuts for the trigger (e.g. $x > 2.3\,\text{mm}$) in polar coordinates and a shift due to the magnetic field and the corresponding deflection of electrons.

Chapter 6

Calorimeter Studies

6.1 Overview

This chapter contains an overview over different studies concerning the calorimetry for LOHENGRIN which have been performed. As already mentioned in Chapter 3, the calorimeters play a crucial role for LOHENGRIN as veto detectors. The electromagnetic calorimeter has to reliably measure the energy of (or the non-existence) of photons in the case of a low energy electron behind the target. The hadronic calorimeter has to be able to detect the presence of any hadron in the final state.

The work was mainly focused on the electromagnetic calorimeter with some considerations for the hadronic calorimeter also being included in this chapter. As will be described in this chapter, the requirements on the electromagnetic calorimeter are much more stringent considering existing technologies, particularly due to the high rate of electrons on target. Additionally, the consideration of hadronic interactions for LOHENGRIN is non trivial. Measurements are planned for the future, but have not been performed yet [10]. That leaves simulation of events for initial considerations. However standard simulation frameworks (e.g. `Geant4`) seem to be not optimised for the energy range LOHENGRIN operates at. A more detailed analysis of hadronic interactions with standard simulation frameworks for LOHENGRIN has been performed by Laney Klipphahn in her Master's thesis.

Nevertheless a first study estimating the detection efficiency of a potential hadronic calorimeter considering the detection of K_0^L has been performed by Hazem Hajjar in his Bachelor's thesis and is presented in [10].

6.2 Theoretical Background for Calorimeters

Calorimeters are usually used to facilitate an energy measurement in particle physics experiments. This is done destructively: Calorimeters are designed such that traversing

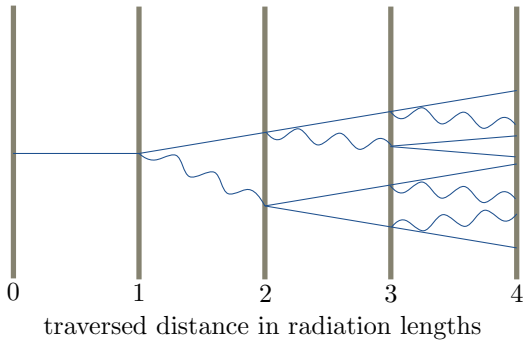

Figure 6.1: Representation of a simplified electromagnetic shower development. After traversing one radiation length, the number of particles is doubled. Wavy lines represent photons, solid lines represent electrons. Inspired by [98], adapted for use in this thesis.

particles and their energy are ideally completely contained within the volume of the calorimeter. Particles hitting a calorimeter initiate a chain of inelastic interactions in which their energy is distributed among many secondary particles undergoing subsequent inelastic reactions. this leads to the formation of a particle shower. At the end of this cascade, particles are stopped by ionising the detector medium [98].

6.2.1 Electromagnetic Showers

Electrons, positrons and photons with high energy develop electromagnetic showers when traversing a dense medium. It can be thought off as radiation of photons by electrons and positrons and pair creation of the photons [98].

A simplified model of shower development was introduced by Heitler [99] (see also [98]). This model assumes that electrons and photons only interact with matter through Bremsstrahlung and pair production until the critical energy E_c is reached. This energy describes the point where energy losses from ionisation of the surrounding material become the dominant form of energy loss. The remaining energy of the electrons and photons is then lost by ionisation [98].

It is also assumed that after one radiation length one such interaction occurs and that each of the two emerging particles carries half of the energy of the incoming particle. A schematic of this simplified development of a shower is depicted in Fig. 6.1.

This simplified model already encapsulates the most fundamental characteristics of electromagnetic showers and gives an idea how a particle's energy can be measured by studying the corresponding shower inside the calorimeter volume. Direct consequences of these considerations are, that the number of particles in the shower increases linearly with the initial particle energy and the length of the shower increases logarithmically with

the energy of the initial particle [98]. The maximum number of particles N_{max} depends on the initial energy E_0 and critical energy E_c like [98]

$$N_{max} = \frac{E_0}{E_c}$$

and the length of the shower t_{max} is given by (in units of radiation lengths) [98]

$$t_{max} = \frac{\ln E_0/E_c}{\ln 2}.$$

The number of particles in a shower can hence be used for an energy measurement [98].

6.2.2 Hadronic Showers

Highly energetic hadrons also form showers inside dense material. However many more processes contribute to their formation compared to electromagnetic showers, making theoretical modelling and simulations much more difficult [98]. Fluctuations of different contributing reactions and their different detection efficiencies make an energy measurement generally more difficult [98].

For Lohengrin however, an exact energy measurement of hadrons in the final state is not needed. The hadronic calorimeter is used purely as a veto detector. Any measured signal in the hadronic calorimeter will lead to the assumption of hadronic activity in the final state, hence vetoing the corresponding event. It has to be noted, that this is a simplified representation. Punch-through from electromagnetic showers in the ECAL into the HCAL has to be expected. This complicates the HCAL veto. This complication is however not addressed here and left for future studies.

The general principle of hadronic calorimetry for Lohengrin thus simply relies on placing material with active areas around the electromagnetic calorimeters and observing whether any kind of hits are registered there. For more details on studies performed with the proposed Lohengrin hadronic calorimeter see Section 6.6 and [10].

6.3 Importance of the Electromagnetic Calorimeter for Lohengrin

As already presented in Chapter 3, the ECAL is used as a veto detector. Its purpose is to detect and veto any events with a high energy SM photon. If this is not done correctly, SM events where a low energy electron is reconstructed by the trackers and passes the trigger, might fake dark photon events.

Hence it must be able to accurately distinguish single high energy photons, while being exposed to a large rate of low energy photons depositing their energy inside the ECAL [10].

It also has to be sufficiently radiation hard as it has to remain operational after shooting approximately 4×10^{14} electrons on target. This requirement is eased somewhat by the fact, that the experiment is designed such that the main electron beam, carrying most of the energy in an event, misses the ECAL. A simulation study showing the distribution of hits and deposited energy in the respective region of the calorimeter is presented in Section 6.4.

The separation of single high energy photons over a background of low energy photons poses strict requirements on the hardware and data acquisition side of a potential ECAL. Possibilities and limits concerning current technological limits on the hardware are presented in [10] and summarised in Section 6.5.2. A first simulation setup in `ExPlORA` with an implementation of a clustering algorithm and energy calibration showing the potential energy resolution capabilities is presented in Section 6.5.1.

6.4 Hit and Energy Distibution

It is possible to set up the Lohengrin experimental setup with the parameters described so far. This includes knowledge of the placement of the target, the trackers and the ECAL. This allows studying the distribution of hits on the ECAL. Additionally the energy of the incoming particles can be recorded and used for an estimate on required radiation hardness for different parts of the calorimeter. All of this information can be used for finding the most suitable technologies for the Lohengrin ECAL.

6.4.1 Simulation Setup

A simulation is set up as described in Section 4.2. The target is placed a the position given in Table 5.1. Tracking layers are also placed at the position given in Table 5.1.

For the study in this section they are not used for reconstructing electron tracks, but are included for the material they introduce into the path of electrons and photons (see Chapter 7 for a dedicated tracking study). The trackers consist of a sandwich of 100 µm of silicon and 1 000 µm of polyethylene. While this is a rough approximation of a real tracking layer, it gives reasonable values in terms of total material budget for a layer of TJ-Monopix2 pixel sensors including support structures (see Section 3.4.2).

A homogenous magnetic field of a length of 1 m behind the target and a strength of 0.9 T is also introduced. Electrons are shot perpendicularly at the target with an energy of 3.2 GeV respecting the size of the beamspot and spread of the beam given in Section 3.1. The `QGSP_BERT` physics list in `Geant4` is used to simulate interactions in matter. In this case the intearctions consist mostly of SM Bremsstrahlung.

For collection of data at the site of the ECAL, the plugin described in Section 4.3.3 is used. It collects the truth level information of every particle passing a fictitious layer. The

ECAL is foreseen to be placed 3.5 m behind the target. Hence this plugin is configured to collect the truth information of any particle traversing this layer at the potential location of the ECAL.

6.4.2 Distribution of Hits and Energy

The resulting distribution of hits simulated with the setup described in Section 6.4.1 can be seen in Figs. 6.2 and 6.3. They show the expected number of hits scaled to 5×10^7 electrons on target. This corresponds to about 0.5 s of runtime. This also gives an idea whether the goal of steering the main electron beam away from the ECAL is fulfilled. For this reason, the outline of the foreseen ECAL is also shown. The differentiation between "Baseline" and "Extended" ECAL is relevant for Chapter 8 and also shown here for illustrative purposes.

Fig. 6.2 shows this distribution assuming the entire setup is surrounded by air. This corresponds to the actual conditions found in the ELSA experimental hall. For the setup described above one would expect the main collection of photons to hit the ECAL in the centre and the main electron beam missing the ECAL. The electron beam would have a tail to the right as this is the deflection direction inside the magnetic field. The electron beam consists of a spectrum of energies after the electrons have undergone Bremsstrahlung. Thus a distribution around a single point is not expected. However using air as a surrounding medium introduces some curious effects.

There are two distinct regions of electrons hitting the calorimeter: One distributed around the centre of the ECAL and the main beam mostly missing the ECAL. Additionally, there is a tail of photons extending to the right of the centre.

Both of these effects can be explained by the surrounding medium. Fig. 6.3 shows the same setup, but with vacuum as the surrounding medium for comparison. The collection of photons is not distributed symmetrically around the centre. This can be attributed to secondary photons being created inside the tracking layers by Bremsstrahlung. Since the electrons have a measurable deviation from the central axis when hitting the tracking layers, the secondary photons created there follow this distribution. Even though they are not affected by the magnetic field. Apart from this, the expected behaviour described above is observed.

The electrons hitting the ECAL in the centre are created by the photons in the surrounding air via pair-production (behind the magnetic field). Since the photons are not affected by the magnetic field, there is no deviation to the right observed here.

The tail of photons is explained by additional Bremsstrahlung reactions in the surrounding air. This is visualised in Fig. 6.4. It shows the exemplary case for a single electron (blue curve) being part of the main beam. The electron is deflected by the magnetic field and misses the ECAL. Along its path several Bremsstrahlung photons (yellow arrows) can be

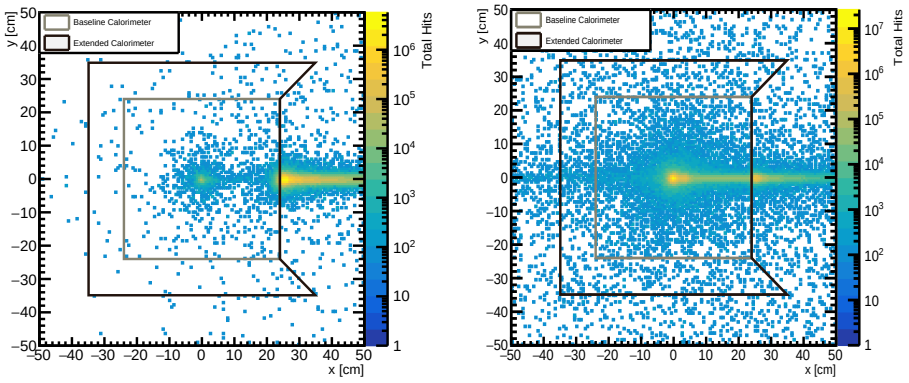

(a)

(b)

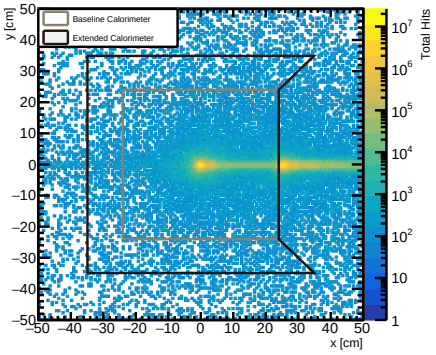

(c) Also available in [10].

Figure 6.2: Distribution of hits of different particles at the foreseen location of the ECAL. The entire detector assembly is placed in air. This simulates the conditions inside the ELSA experimental hall. The differentiation into baseline and extended calorimeter is used in Chapter 8 and included for illustrative purposes. (a): Hits of electrons. (b): Hits of photons. (c): Hits of all particles.

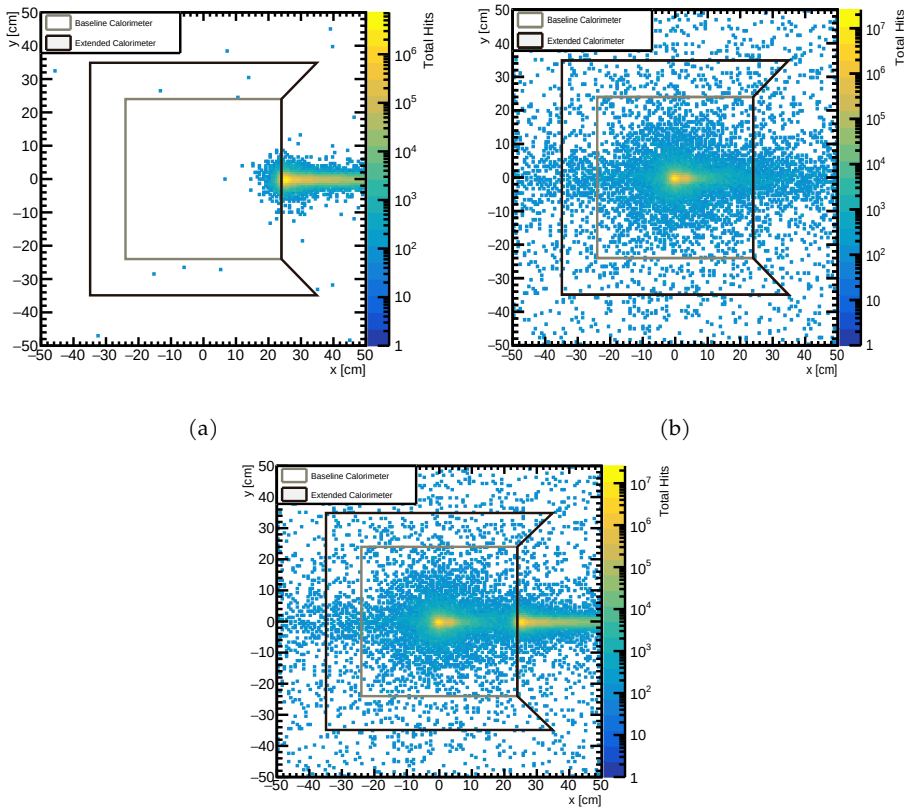

(a) (b)

(c)

Figure 6.3: Distribution of hits of different particles at the foreseen location of the ECAL. The entire detector assembly is placed in a vacuum. This does not correspond to the conditions inside the ELSA experimental hall. However it allows for the study of the effects of air as a surrounding medium. The differentiation into baseline and extended calorimeter is used in Chapter 8 and included for illustrative purposes. (a): Hits of electrons. (b): Hits of photons. (c): Hits of all particles

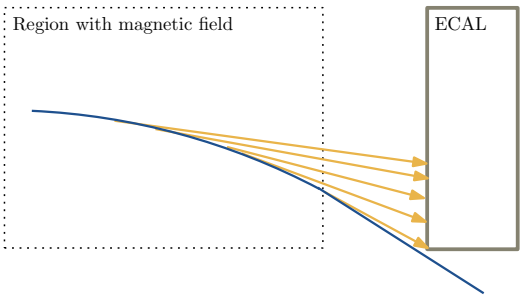

Figure 6.4: Visualisation of additional Bremsstrahlung in the surrounding air creating the tail of photons at the site of the calorimeter. The electron is shown in blue and created photons are depicted as yellow arrows.

created in the surrounding air. Due to the relevant cross section (see also Section 2.4.3), most of these photons are created with little energy and emitted almost collinearly from the beam. Hence creating the tail seen in Figs. 6.2(b) and 6.2(c).

Each hit can be scaled with its respective energy. This can be used to estimate the total radiation being deposited in different parts of the calorimeter. Since the electrons mostly miss the ECAL, the main contribution is from photons. These will mostly hit the centre of the ECAL (see Fig. 6.2). This is also seen in Fig. 6.5. It shows the total energy deposited per area at the ECAL position scaled to 4×10^{14} events on target. As expected, most of the energy will be deposited inside the photon cone.

6.4.3 Potential Considerations Concerning the Use of Crystal Calorimeters Regarding Radiation Hardness

Scintillating crystals are widely used in the construction of electromagnetic calorimeters. Here a scintillating crystal such as $PbWO_4$ is used as the absorber material. The light created by the showers inside the crystal is detected by photomultipliers. This signal can then be used for the energy measurement.

Calorimeters constructed in this way usually provide excellent timing and energy resolution [10, 98]. However one has to consider the crystal's degrading performance with irradiation. This is especially relevant for the central region of the foreseen calorimeter. Common designs (see [98] for examples) feature long crystals extending the entire or most of the length of the calorimeter. Spatial resolution in the perpendicular plane is obtained by segmenting the calorimeter into multiple crystals.

For Lohengrin this would mean that the energy of a particle is mostly deposited in the same crystal which is initially hit at the front of the ECAL. The size of the main photon beam spot is however relatively small such that the entire energy is deposited in at most a

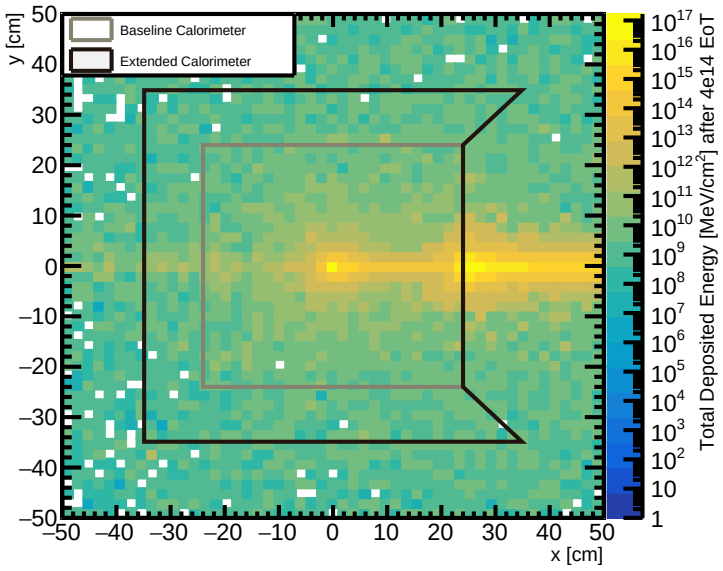

Figure 6.5: Total energy deposited at the position of the ECAL scaled to 4×10^{14} electrons on target.

few crystals located at the centre of the ECAL. This would mean significantly differing rates of crystal degradation with the central crystals potentially having to be replaced an unfeasible number of times. Though this would depend on the material and exact geometry which is chosen.

Due to the potential complications that would arise from choosing crystal calorimeters, this option is not studied in more detail in this thesis. It is noted however that the complications listed above are much less significant for the non central part of the ECAL. The feasibility of using a mixed technology ECAL with scintillating crystals in the non central region is an interesting topic for further research.

6.5 The Calice Electromagnetic Calorimeter Prototype

As an alternative to the crystal calorimeter described above, a prototype silicon tungsten calorimeter has been studied in more detail. Here the calorimeter is constructed as a sandwich of passive absorber layers (such as iron or tungsten) and active layers (such as silicon). The shower mainly develops in the passive layers and is sampled in the active layers where electronic signals from the shower can be registered.

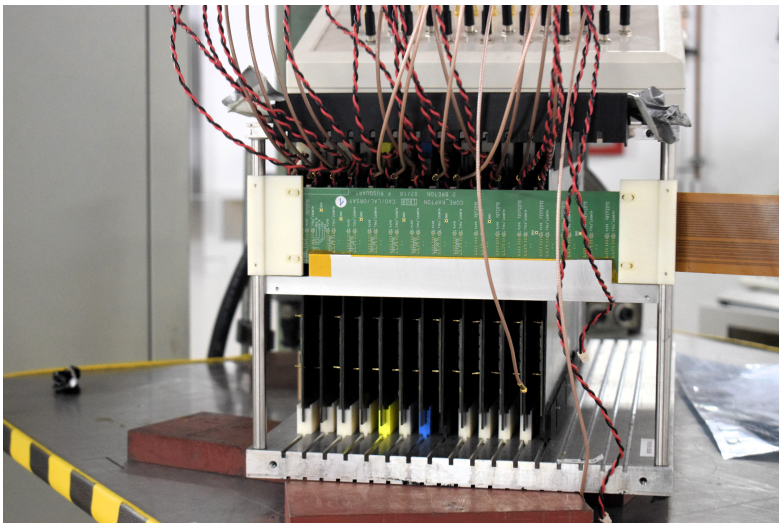

Figure 6.6: Photograph of multiple layers of the CALICE prototype from 2021. The modularity and the individual layers can be seen. Active and passive layers are arranged in an outer frame making the individual distances and arrangement customisable. Taken from [10].

The CALICE collaboration has developed a prototype for such a sampling calorimeter constructed mainly from tungsten as passive and silicon as active material [100]. CALICE provides a modular platform where the arrangement of passive and active layers can be chosen freely depending on the need of the experiment. Fig. 6.6 shows a photograph of several layers of the prototype from 2021. The individual layers can be seen. The modularity stems from the construction method of embedding the layers inside an outer frame. The distances and arrangements of the individual layers can be chosen by providing the respective outer frame.

For preliminary studies a prototype based on the CALICE prototype has been included in simulation. The setup described here consists of 30 layers. Each layer is a stack of three sublayers:

- A 2 mm thick tungsten sheet as passive absorber material
- A 500 µm thick silicon sheet representing the active material. The silicon sheet is further segmented into pads
- A 1 cm gap of air taking into account the construction of the CALICE prototype with modular layers (see also Fig. 6.6).

The dimensions for each of the sublayers are inspired by values given in [100]. The total thickness of the prototype as discussed above is about 17.3 X_0. Each of the layers[1] covers an area of $38.5 \times 38.5\,\mathrm{cm}^2$, while each of the pads has a size of $5.5 \times 5.5\,\mathrm{mm}^2$.

A simulation implementing a clustering algorithm with a subsequent energy measurement was performed during work on [10], where the results are also shown. The study is described in more detail in Section 6.5.1. Requirements on the analog signal processing of the ECAL are discussed in [10] and also reviewed in Section 6.5.2.

6.5.1 Simulation Setup in ExPlORA and Energy Measurement

The ECAL prototype as described in Section 6.5 is implemented in ExPlORA. This includes the layered structure and the possibility to digitize energy deposits in the silicon layers of the ECAL. A rendering of the completed ECAL in simulation is shown in Fig. 6.7.

The construction of the ECAL then allows for a full Geant4 simulation of the setup with particle interactions. Fig. 6.8 shows an electromagnetic shower developing inside the calorimeter volume simulated with Geant4 due to an electron beam hitting the first layer of the ECAL.

Digitisation

The next step towards a simulated energy measurement is a digitization of the created energy deposits. This is done in ExPlORA by registering the silicon sublayers as sensitive detector elements. Energy deposits created by Geant4 inside these sensitive detector elements are then subsequently digitised into hits.

This is a multi step process in ExPlORA. The idea of the framework is that it can be used as a simulation and analysis tool. Hence the creation of digitised hits cannot be done in a single step.

First, every energy deposit inside a sensitive detector element is assigned information which would be available if the detector would actually measure the hit and not be simulated. This includes a channel number (representing the pad) and an ADC value depending on the size of the energy deposit. No real calibration of the chip is done here and the ADC values are also not used in this analysis. The information relevant here is merely whether a pad of the ECAL was hit. The step is nonetheless necessary due to the way ExPlORA handles simulated data.

In the next step, the channel number created in the first step is combined with information provided by the geometry plugin for the ECAL. After this, each pad which registered

[1] The size does not correspond exactly to the values given in Section 3.4.3. It is however cleanly divided by the size of the pads for the prototype and large enough to fully contain a shower laterally. Hence this size is chosen for the study here.

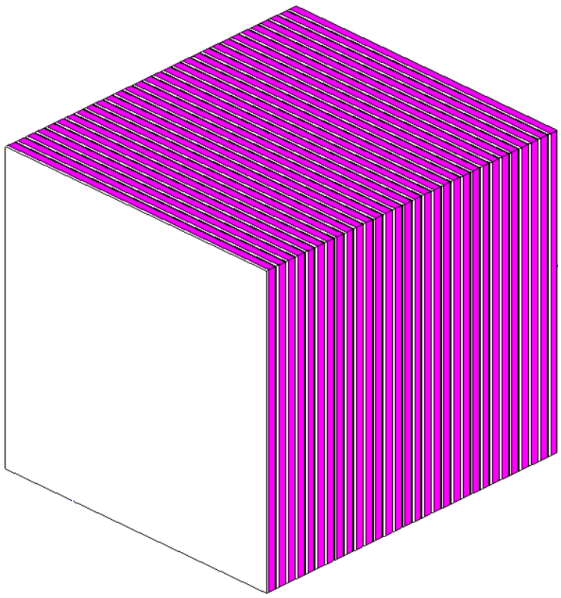

Figure 6.7: The ECAL as described in Section 6.5 modelled in ExPlORA. The 30 distinct layers are clearly visible. The silicon sublayer may not be visible due to its relatively low thickness compared to air and the absorber sublayers.

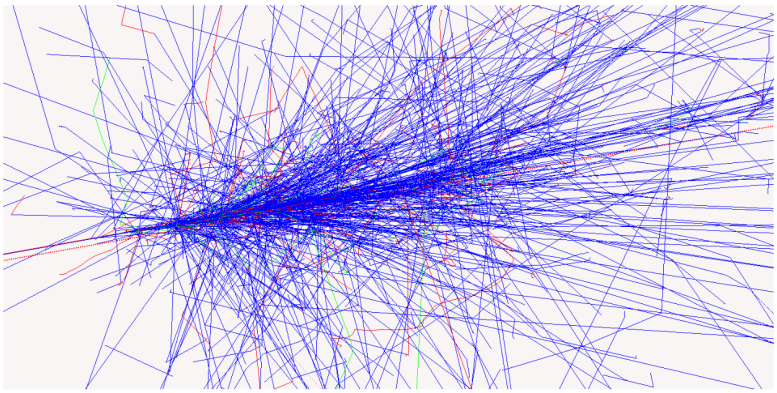

Figure 6.8: An electromagnetic shower developing inside the calorimeter volume simulated with Geant4. The calorimeter volume is deliberately not shown to allow for a clearer observation of the shower development. Different particles and the z-axis are represented by unique colours and line styles: photons (solid blue), electrons (solid red), positrons (solid green), and z-axis (dashed red). Also found in [10].

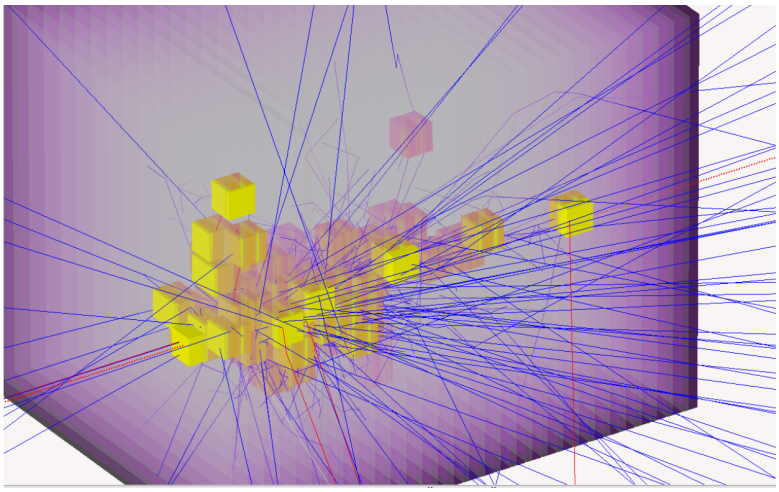

Figure 6.9: A simulated electromagnetic particle shower inside of the ECAL. This time the digitised hits are also shown. They are visualised by boxes, where the box's centre is located at the position of the digitised hit. Also presented in [10].

an energy deposit creates a hit object which contains the physical location of that pad and can be used for further analysis. This step can also be performed with measured data to assign physical locations once the detector is built and placed. This also allows for readjustments to be taken into account should some parts of the detector be moved during the runtime of the experiment. Fig. 6.9 shows a particle shower with the digitised hits in the same picture. The hits are represented by boxes, where the box's centre is located at the digitised position of the hit.

There is another point to consider when simulating individual pads and or pixels in `ExPlORA`. The easiest way to implement a simulation like described above in this section is to build each silicon sublayer such that each pad is registered as its own volume. This way the channel number can be easily assigned when digitising energy deposits as it is just the index of the corresponding pad volume. This however comes with a significant disadvantage. Each volume has to be registered and creates a lot of overhead when running the program and occupies RAM storage. It thus reduces simulation performance and scalability should simulations for larger detector components with even more volumes be needed. Implementing the ECAL this way is thus not advisable.

Instead, each silicon sublayer is implemented as a single volume. The individual pads are simulated with fictitious channel numbers. This minimises the total number of required volumes and does not cause the problems written above. The idea behind this approach and the comparison to the simplified digitisation described above, is shown in

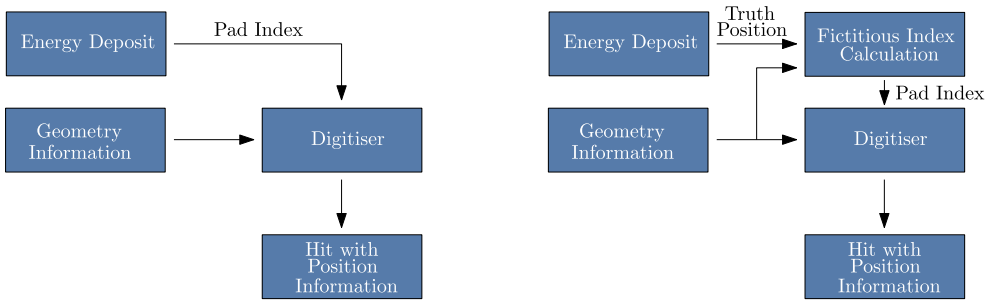

Figure 6.10: Schematic showing the necessary steps for digitising energy deposits in ExPlORA. It also compares the way it would be done if every pad is its own volume (left) and the more efficient way of introducing a fictitious layer and simulating all of the pads as a single volume (right).

Fig. 6.10. Simulating the pads as a single volume does however create the need for another method of assigning channel numbers when digitising energy deposits. For this truth information is used at the point of assigning the channel number. An algorithm takes the true position of the simulated energy deposit and overlays a grid corresponding to the positions of the pads. The grid location which contains the true position of the energy deposit corresponds to the pad which would have been hit. Consequently the channel number of this fictitious pad is then assigned to the energy deposit. This is then used in the second step for a position assignment. The hit is then assigned a position which corresponds to the centre of the fictitious pad. This recreates the desired behaviour while minimising the amount of needed volumes.

Clustering

The next steps towards an energy measurement is the implementation of a clustering algorithm. As already introduced in Section 6.2.1, the number of particles in a shower can be used for an energy estimate in a simplified model for the shower development. The clustering algorithm thus aims at creating clusters of digitised hits where the size of the cluster can be used for estimating the energy of the beam responsible for that cluster.

A simple clustering algorithm was included in ExPlORA. Each hit in the ECAL is treated as a potential seed for a cluster. A function relying on the geometry information is able to determine adjacent calorimeter cells. Adjacency can be modified by providing an additional radius parameter. This radius parameter is an integer and is to be understood in units of cells. Any hit that is inside of a "sphere" of this radius of pad sizes is treated as adjacent. It has to be noted that this works across all three cardinal directions i.e. also across layers. Consider the following example: The radius is set to one. A hit which was

digitised in one of the calorimeter cells can have up to six adjacent hits. This includes four potential hits from the immediate neighbouring cells in the same layer and potentially two additional hits from a cell in the same position, but on different layers to each side of the layer of the original hit. The actual number of adjacent hits depends on whether a hit exists in that position and whether the original hit is on the edge of the ECAL, in which case there are fewer possible positions for adjacent hits.

Next, any cluster seed which is adjacent to another cluster seed is added to the larger of the two clusters (if both cluster seeds have the same size, one of them is added to the other. The ordering is arbitrary in this case). This is done recursively until no adjacent cluster seeds are left and thus all clusters have been found. The total size of the cluster i.e. the number of hits contained inside of it can be used for an energy measurement in the next step.

Energy Measurement and Calibration

With all of the steps described in this section it is now possible to perform a calibration of the calorimeter and as subsequent energy measurement using the `Geant4` simulation. For this events are simulated with differing beam energies and the number of hits in the resulting cluster is used as basis for the energy measurement. With N being the number of hits in the silicon layers in a cluster, the uncalibrated energy E is calculated for each cluster in `ExPlORA` by using Eq. (6.1).

$$E = N \cdot 2\,\mathrm{MeV\,cm^2\,g^{-1}} \sum_{i=1}^{3} \rho_i d_i \tag{6.1}$$

Here i represents the sublayer i.e air, silicon and tungsten (see also Section 6.5), ρ_i is the density of the respective material in the sublayer, and d_i the corresponding thickness.

It has to be noted, that the energy resulting from this procedure is uncalibrated and should not be understood as the actual energy deposited in that cluster. This formula merely serves as a starting point to convert the number of hits to an energy and leverages on ideas given in Section 6.2.1 and the energy loss of minimum ionizing particles in matter (see also [98]).

Next, 10 000 events are simulated for energies of 200 to 3 800 MeV, the clustering radius is set to one, and the reconstructed uncalibrated energy is recorded. The true beam energy can then be divided by the uncalibrated energy to obtain a calibration function. This is depicted in Fig. 6.11

A linear function was chosen, because it represents the simplest function which still feasibly encapsulates the trend of the data. Whether more sophisticated calibrations are better suited will have to be determined in a future study. The fit resulted in the calibration

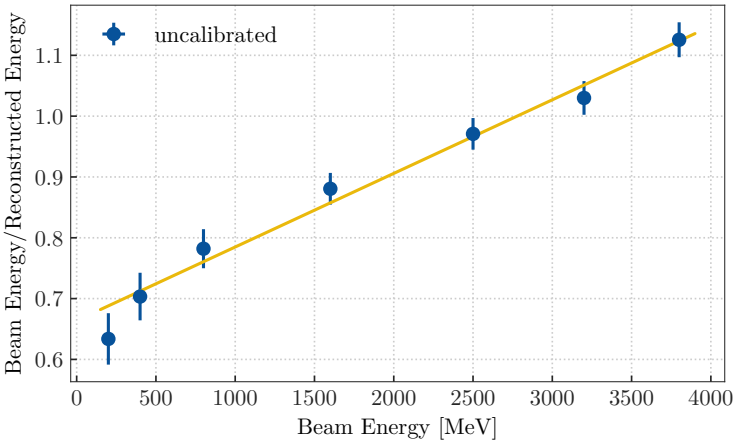

Figure 6.11: Uncalibrated reconstructed energies in relation to the true beam energy. A linear function has been fitted to the data points. Uncertainties in the reconstructed energy are given by the standard deviation of reconstructed energies from the sample of simulated events.

function given in Eq. (6.2) with a χ^2/NDF of 0.71.

$$f(x) = 1.25(8) \cdot x + 0.65(2) \tag{6.2}$$

The calibrated energy for each cluster $E_{\text{calibrated}}$ is then given by Eq. (6.3).

$$E_{\text{calibrated}} = f(E) \cdot E \tag{6.3}$$

The functionality of `ExPlORA` was extended to support the application of a calibration function to the energy measurement in a cluster. Fig. 6.12 shows a comparison of the calibrated and uncalibrated energies. The effect of the calibration is clearly visible. Fig. 6.13 shows the calibrated reconstructed energy versus the true beam energy and a line trough the origin with unit slope. A perfect energy reconstruction would lead to all points being located on that line. It can be seen, that there is a bias towards reconstructing energies which are too low for beam energies in the upper half of the studied range. However this setup is in general able to distinguish between low and high momentum clusters.

Fig. 6.14 shows the ratio of the energy reconstruction resolution σ_{Reco} and the true beam energy E_{Beam}. The resolution is estimated by the standard deviation of reconstructed energies from the respective simulated sample. One would expect this to follow a function

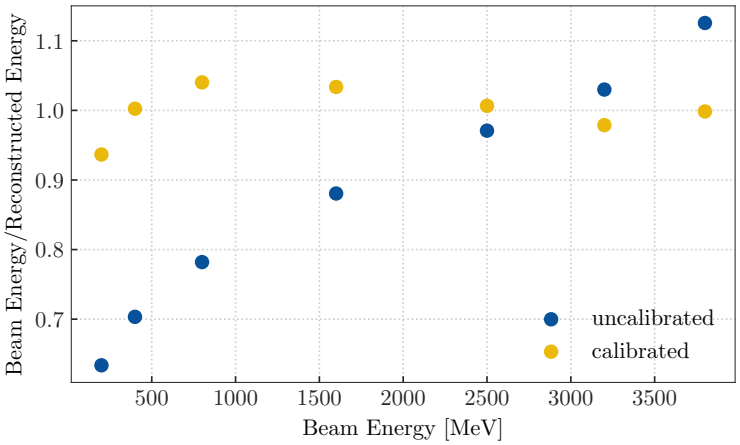

Figure 6.12: Comparison of calibrated and uncalibrated energy measurement. Error bars are not shown here to not distract from visible effect of the calibration.

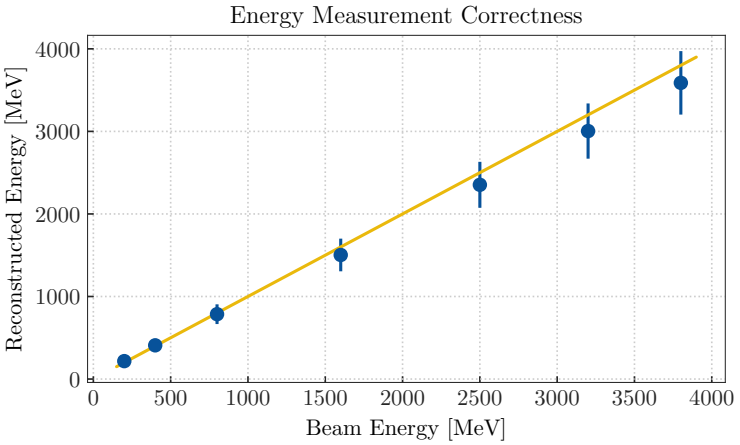

Figure 6.13: Reconstructed beam energy against true beam energy after the calibration. The solid line represents a line through the origin with unit slope. Also available in [10].

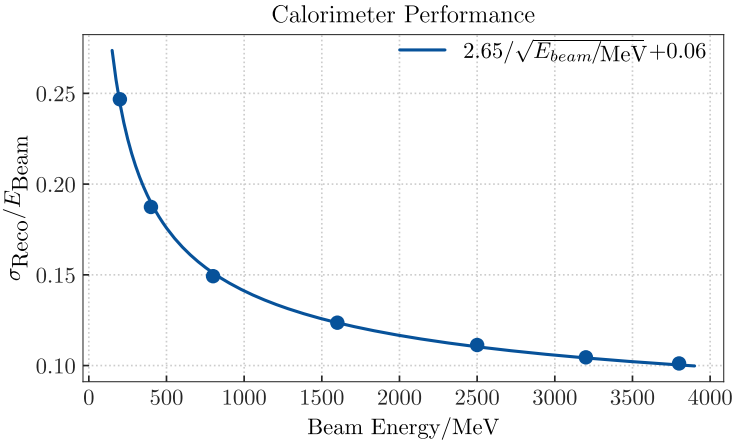

Figure 6.14: The ratio of energy reconstruction accuracy to beam energy with corresponding fit. Also available in [10].

of the kind given in Eq. (6.4) [10, 98].

$$\frac{\sigma_{\mathrm{Reco}}}{E_{\mathrm{Beam}}} = \frac{a}{\sqrt{E_{\mathrm{Beam}}}} + b \tag{6.4}$$

This is fulfilled by the procedure described in this section. A potential noise term has been neglected here since the signal-to-noise ratio of the CALICE prototype is at least 10 and is not as relevant as the other contributions [10, 100].

The procedure described here successfully implemented a version of the CALICE ECAL prototype in a simulation framework and studied some key parameters with a `Geant4` simulation. A digitisation and clustering algorithm were implemented along with the first iteration of a working energy measurement where the typical beahaviour of ECALs could be reproduced.

6.5.2 Requirements on the Analogue Signal Processing

The ECAL is subject to a constant stream of photons. As already presented in Section 6.4.2, Fig. 6.2 shows the distribution of hits at the foreseen ECAL position 3.5 m behind the target for a runtime of 0.5 s. The average rate of hits in the centre of the calorimeter (where it is highest) is about 10 MHz. This means that the average time in between hits is 100 ns. The most probable time between hits is however significantly shorter than that [10]. This places hard limits on the shaping time of the readout chain as a high detection efficiency is vital for the foreseen veto strategy of LOHENGRIN. A feasibility study with simplified

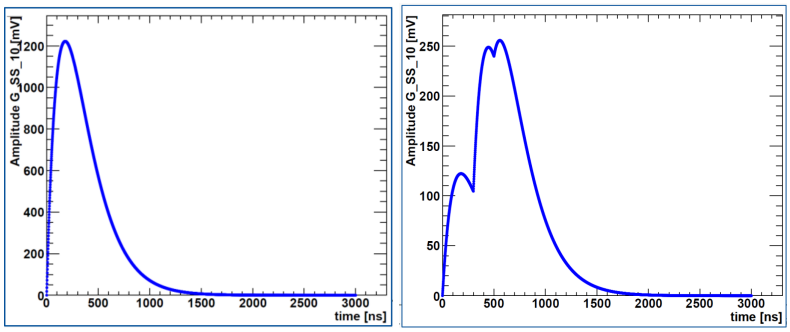

Figure 6.15: Left: Response of the CRRC shaper for a single photon hitting a calorimeter cell. Right: Shaper response for multiple photons hitting the same calorimeter cell before the response can return to baseline. Plots provided during private communication with Matthias Hamer.

assumptions for the analogue front-end in the calorimeter readout ASIC was done in [10]. The main results and key points are summarised here for completeness.

A total of 8×10^5 SM events were simulated in `Geant4` and their energy deposition inside the ECAL recorded and digitised using an approximation of a CRRC shaper with variable peaking times τ in an analogue front-end with a track-and-hold readout. This deliberately includes pile-up, i.e. two particles hitting the same calorimeter cell before return to baseline [10]. Fig. 6.15 shows the effect of pile-up on the shaper's response. The multiple peaks stem from multiple particles hitting the cell before the response can return to baseline.

For each event window $\Delta\tau = 2\,\text{ns}$ the number of electrons hitting the target is randomised according to a Poisson distribution with mean $\mu = 0.2$ (see also Section 3.1). For events occurring at time $t = t_0$ and passing the L0 trigger (see Chapter 5), the readout of the ECAL is simulated. This means that the response of all cells at time $t_0 + \tau$ is integrated over the entire calorimeter. This provides the response of the entire ECAL for events with low energy electrons and high energy photons [10]. The same was done in a second sample, however this time removing energy deposits from photons. This simulates the response for events with low momentum electrons and no photons [10]. These two samples essentially recreate the most important features of background- and signal-like events. The signal shaping time must thus be fast enough to sufficiently distinguish these two cases.

This response was simulated for peaking times of $\tau = (10, 30, 60, 180)\text{ns}$. Fig. 6.16 shows the uncalibrated calorimeter response for a shaping time of $\tau = 30\,\text{ns}$. The shown *pseudo measured energy* is not to be confused with the uncalibrated energy in Section 6.5.1. It is merely used here to refer to the calorimeter response to show the ability of distinguishing

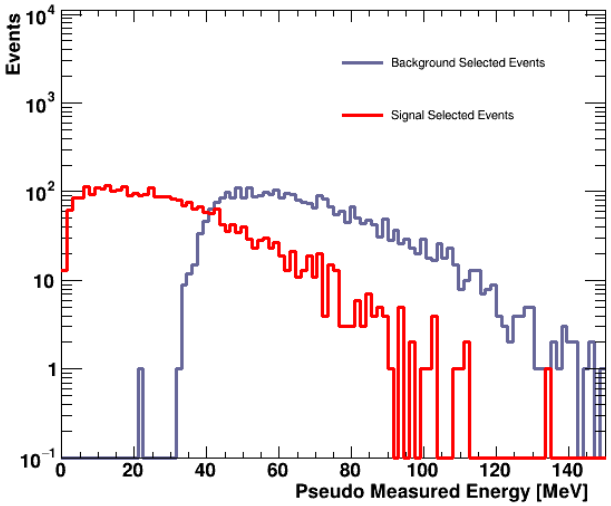

Figure 6.16: Calorimeter response for SM events with a high energy photon in the final state that pass the L0 trigger and for the same events where the energy deposited in the calorimeter by the photon is removed. A peaking time of $\tau = 30\,\text{ns}$ has been assumed for the CRRC shaper in the analog frontend. Analogue signal information was used for this plot. Taken from [10].

the two samples of events described above. It is possible to introduce a cut based on this parameter which removes $\approx 100\,\%$ of SM background events while maintaining a signal efficiency of 68 %.

Increasing the peaking time to $\tau = 60\,\text{ns}$ leads to a cut that preserves a signal efficiency of only 4.5 %, while removing any SM background event [10]. The ASIC which is currently implemented in the SiW ECAL CALICE prototype offers a peaking time of $\tau = 180\,\text{ns}$. The requirements for the analogue signal processing in the readout ASIC are thus rather challenging for a calorimeter with square cells of $5.5 \times 5.5\,\text{mm}^2$. It is understood that significant improvements are required for a potential use in LOHENGRIN [10].

6.6 Hadronic Calorimetry

The hadronic calorimeter (HCAL) plays a crucial role in vetoing possible backgrounds. It is most important in vetoing neutral hadrons as they will not leave a signal in other parts of the detector. A feasibility study regarding the effectiveness of different HCAL thicknesses with simplified assumptions was performed in [10]. The key results and main points are reiterated here for completeness.

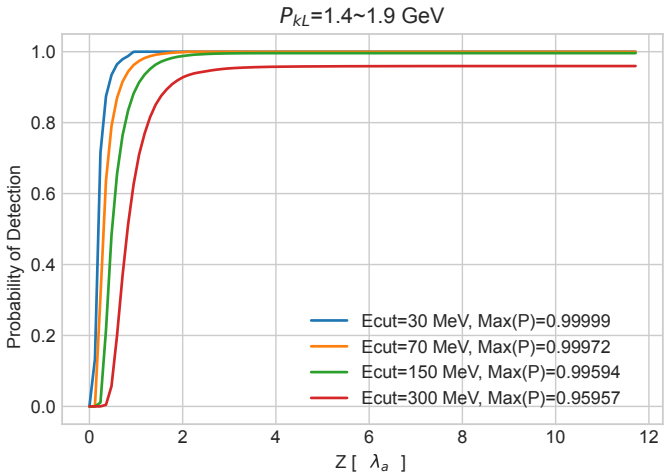

Figure 6.17: Expected detection probability of neutral hadrons (in this example K_L) for different E_{Cut} and hadron momenta considering calorimeter thickness (Z) in absorption lengths (λ_a). Taken from [10].

Hadrons can be created in relevant numbers and traverse the detector undetected before decaying into more visible decay products [10]. The HCAL needs to cover as large an angle as possible in order to achieve the maximum veto efficiency. In a first step this is achieved by constructing it around the ECAL (see Chapter 3 and Fig. 3.7). It might also be feasible to extend the coverage of the HCAL even further outside of the photon cone in the future. This is in principle possible, if one takes care to avoid the electron beam as it will lead to unwanted hits in the HCAL [10].

Given the concept described in Section 6.4.1, a simple hadronic sampling calorimeter is constructed in `ExPlORA`. It consists of a sandwich of iron absorber layers (2 cm) and active silicon layers (0.05 cm). The number of layers is not given since the study was performed to estimate the detection efficiency given the thickness of the HCAL.

The following simplifying assumptions have been made in the study. The particles used are K_L[2]. Results for neutrons are expected to be similar once mass differences in momentum and energy of the particles being shot at the HCAL are accounted for [10]. The particles hit the HCAL perpendicularly in the centre. Consequences of non perpendicular impacts are discussed below. A particle is considered as detected and thus the event vetoed if a minimum energy of E_{Cut} is deposited in the HCAL up to the studied thickness/depth.

[2] Other hadrons could also be used for this estimate. K_L are expected to be similarly hard to detect as other neutral hadrons.

The result of the feasibility study is shown in Fig. 6.17. The expected veto efficiency is displayed for K_L of a uniform distribution of forward momenta in the range [1.4 GeV, 1.9 GeV]. The detection probability increases with increasing HCAL thicknesses as is to be expected. The veto efficiency is expected to be higher than 99.999 % for a calorimeter with a thickness of at least three nuclear interaction lengths (λ_a) for a wide range of neutral hadron momenta, if the detection threshold E_{Cut} can be decreased to 30 MeV [10]. In the baseline scenario (see Chapter 8 for explanation of baseline), the HCAL is assumed to have a size of $2.5 \times 2.7 \times 1.45\,\text{m}^3$ (also the dimensions depicted in Fig. 3.8) [10]. These dimensions will likely be have to revised in the future once more accurate studies have been performed and their impact evaluated. One example looking at a more accurate simulation of hadronic backgrounds is the master's thesis by Laney Klipphahn.

The hadrons will likely not hit the HCAL perpendicularly but at an angle. This effectively reduces the thickness of the calorimeter depending on that angle. Actual distributions for hadronic backgrounds are hard to simulate (see above mentioned thesis by Laney Klipphahn) and measurements of hadronic backgrounds are planned in the future (see [10]). A final HCAL design will have to take these points into account [10].

Chapter 7

Tracking for Lohengrin

7.1 Overview and Importance of Tracking for LOHENGRIN

Tracking plays an important part in the LOHENGRIN experimental strategy. The hits of the electron in the tracking layers are used to reconstruct a trajectory and determine the electron momentum in an event. This momentum measurement is one of the key ingredients for the definition of a signal region (see Chapter 8).

It will become apparent in Chapter 8 (see also [10]), that the tracking algorithm needs to be able to reconstruct electrons with a high efficiency and down to the lowest possible momenta. A first iteration of an electron tracking chain based on `Geant4` simulations was realised for this work. It allows for an estimate of possible limitations and performance considering currently available algorithms and was realised with **A**CTS **C**ommon **T**racking **S**oftware (ACTS) [101, 102]. One of the main goals is showing that the reconstruction of low-momentum electrons is at all possible to a feasible degree with ACTS, as the algorithms were not designed for this range[1].

This chapter is dedicated to describing the entire tracking chain. It covers a wide range of topics. Therefore a quick overview of sections in this chapter is given in the following: Section 7.2 contains information on necessary steps to obtain a track fit and summarises the broader topic of track fitting in general. A quick overview of the ACTS software package used for electron tracking is given in Section 7.3. Section 7.4 introduces a basic fitting algorithm (Kalman Filter) and introduces an extension (Gaussian Sum Filter) to deal with electrons in particular. They need extra considerations concerning their energy loss in material. The implementation of the LOHENGRIN geometry and simulation setup within ACTS is described in Section 7.5. Section 7.6 shows the results of performance studies done with the setup described in previous sections. Results obtained there are ultimately used for a final sensitivity estimate in Chapter 8 and [10].

[1] This was the result of personal communication with Benjamin Huth.

7.2 Tracking in a Nutshell: Necessary Steps

This section serves to place the explanation about tracking algorithms in Section 7.4 and the implementation of the LOHENGRIN setup into ACTS in Section 7.5 into a broader context. The points raised here are revisited in more detail in those sections. It is therefore non-exhaustive and more detail is also given in the relevant literature (such as [98, 102]). An interactive overview with references for each topic can also be found in the ACTS online documentation [101].

7.2.1 Particle Propagation

A key part of tracking is the ability to propagate a particle through space given the particle's current position, momentum and charge. The collection of these values is referred to as state vector. The trajectory can be determined by the state vector, the surrounding magnetic field and possible material. In the absence of material and a completely homogenous magnetic field, this trajectory is described by a helical path and is analytically solvable. In a more general case though with inhomogeneous magnetic fields and material affecting the trajectory, this has to be solved numerically [103].

7.2.2 Geometry Description

A detailed and relevant model of the detector assembly is required for tracking. This is necessary to associate signals from sensitive detector elements to a position in the global coordinate frame of the experiment. This concept was already introduced in Section 6.5.1. A detailed geometry description is also needed to adequately account for material effects along the particle's trajectory.

7.2.3 Material Modelling and Material Effects

Particles passing through detector material can interact through various mechanisms. The most relevant effects for a tracking detector are multiple scattering and energy loss through ionisation and Bremsstrahlung. Multiple scattering describes the repeated deflection of a charged particle due to interactions with the Coulomb fields of atomic nuclei within a material. This process is random and is usually accounted for by increasing the uncertainty of the relevant propagation angles/direction in the track state. The energy lost when traversing material is accounted for by adjusting a particle's momentum and the corresponding uncertainties of the track state.

7.2.4 Clustering

In this step, the raw readout data from the sensors is converted to meaningful objects which can later be used in tracking algorithms [103].

In the special case of pixel detectors, such as the ones foreseen for the LOHENGRIN tracker (see Section 3.4.2), this concept was also already introduced in Section 6.5.1[2]. When a traversing particle leaves a signature inside the detector, multiple pixels can measure a signal from the same particle. These then have to be combined into a single cluster object since they were also created by the same particle. This usually also includes algorithms to disentangle close-by or joint clusters that originate from more than one hit [103].

7.2.5 Pattern Matching - Track Finding

Once all the measurements are acquired, they have to be combined into track candidates. For LOHENGRIN this is relatively simple, because the track multiplicity in LOHENGRIN is expected to be small. As an example, in signal events and the most dominant background contribution, only a single track is expected in the initial and final state (see also Section 8.1). It is therefore assumed, that only one track is to be found per event. In general however, multiple particles pass through the detector in the same event. Clusters then have to be assigned to track candidates by a track finding routine before any track fit can be done. Fig. 7.1 shows this conceptually: Two tracks generate clusters in the tracking planes. A track finding algorhithm needs to be able to accurately determine which cluster belongs to which track. Methods for track finding can be classified into local methods and global methods. Local methods start with a small number of hits (seed) and then reconstruct the track from that. This already contains information about the curvature of the trajectory. A very flexible algorithm that combines track finding and track fitting is the Combinatorial Kalman Filter [103].

Global methods try to cluster the hits into track candidates without iterating through them. An example of this is the Hough transform which applies a global coordinate transformation that maps curves in the original coordinate system to straight lines in the transformed system [103]. More information on this can be found in e.g. [104].

7.2.6 Track Fitting

The task of track fitting is to obtain an estimate of a particle's state vector and corresponding uncertainties from already found track candidates. In order to do this accurately, the particle must be propagated properly through the detector and material effects have to be taken into account [103].

[2] This deals with calorimeter cells, but the concept works analogously for a single layer of pixel detectors.

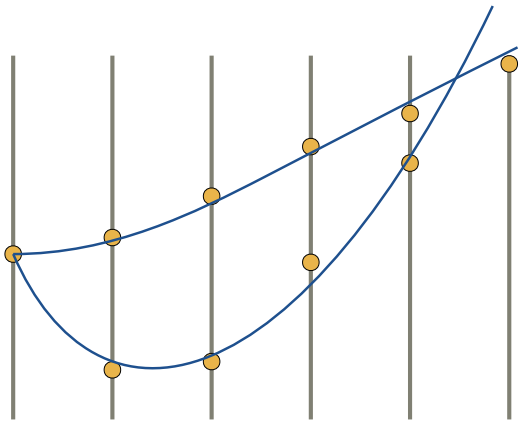

Figure 7.1: Visualisation of track finding for two simultaneous tracks. Yellow dots represent clusters in the tracking planes and blue curves the actual trajectory of the particle. A track finding algorithm needs to be able to accurately determine which cluster belongs to which track.

If one assumes Gaussian uncertainties, a global χ^2 fit is the optimal solution[103]. As is discussed in Section 7.4.3 this is assumption is generally not valid for electrons due to their unique form of energy loss in matter. Section 7.4 introduces an iterative equivalent to a global χ^2 fit and an extension which can deal with non Gaussian uncertainties.

7.3 Overview of ACTS– Usage for Lohengrin

The ACTS project [102] aims at providing high-level experiment independent tools for track reconstruction. It draws from experience of track reconstruction algorithms in the ATLAS experiment and is in active development. It is developed with the understanding that while tuning of reconstruction algorithms is very experiment specific, the actual algorithms for reconstruction share many common features [102]. Future experiments are expected to put high computational stress on track reconstruction software. Thus the development of highly performant algorithms is also one of the main goals of the project [102].

As was highlighted in Section 7.2, track reconstruction is a complex process with many steps. Having a toolkit with basic algorithms, which can be employed also for Lohengrin, brings multiple advantages. Large community support and active development means that potential errors in code are found and addressed much more quickly, than with a small team developing the tracking framework for a single experiment individually. It also creates opportunities for collaboration and exchange with researchers from other

experiments. The usage in as many experiments and collaborations as possible further strengthens the points above and encourages the development of standards regarding to tracking across particle physics in general.

The steps highlighted in Section 7.2 are already implemented in working algorithms in ACTS. Additionally, ACTS provides capable implementations of the Kalman Filter and Gaussian Sum Filter (see Section 7.4 and [103]). For all of these reasons, ACTS is used as toolkit for the tracking studies in this chapter[3].

7.4 An Overview of Algorithms: Electrons as Special Case in Track Fitting

This section deals with the introduction and overview of two widely used algorithms for track fitting, the Kalman Filter (KF) and an extension to it the Gaussian Sum Filter (GSF). The GSF is interesting for electron fitting, because it is specifically designed to deal with non-Gaussian process noise. This can be used in case of electron tracking for the parametrisation of energy loss in material. This is explained in more detail in Section 7.4.3.

7.4.1 The Kalman Filter Conceptually

The KF describes an iterative procedure to combine information from a measurement and a prediction of a system. Consider as an example a physical system, where the state of this system is measured with some uncertainty. This system evolves in time according to a known physical law. If at another point in time another measurement with some uncertainty is performed, there are two estimates for the state of the system: The propagated state based on the initial measurement and the state based on information of the new measurement. The KF describes a procedure which combines these two pieces of information into a weighted combined state estimate. This combined state estimate is referred to as filtered state.

In the case of tracking, each tracking layer represents such a measurement surface and each cluster is another measurement. This is schematically shown in Fig. 7.2. The estimate of the true position of the particle becomes progressively better as more measurements are included.

7.4.2 Mathematical Formulation of the Kalman Filter

This part is based on the discussion in [17] and [103]. More information can be found there and in references given there. The basic mathematical formulation of the KF is

[3] More specifically: ACTS v37 with necessary modifications (see Section 7.5).

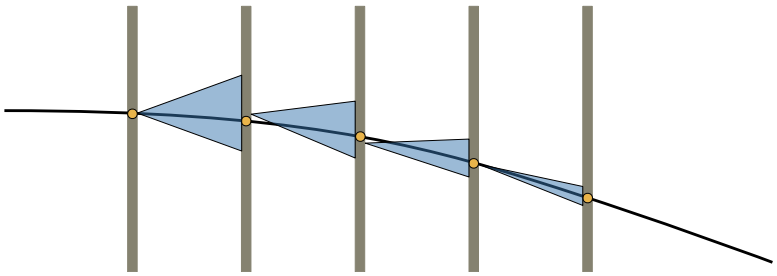

Figure 7.2: Schematic showing the principle of the KF applied to track fitting. Yellow dots represent clusters in the tracking layers (shown in gray). The particle trajectory is shown in black. Estimates of the track position and their corresponding uncertainty are indicated as shaded blue regions. This only shows the forward pass, i.e the prediction and filtering step (see Section 7.4.2). Inspired by [98].

included here, however the detailed description of how the propagation and integration of the equation of motion is done within ACTS, is not necessary for the understanding of this thesis. It can be found in e.g. [101–103].

Assume some general state at time k is represented as $\boldsymbol{x}_k$ with the corresponding covariance matrix C_k. Also assume, that the evolution of this state with respect to time is known and follows a physical law, such that said evolution can be written as in Eq. (7.1) [17].

$$\boldsymbol{x}_k = f(\boldsymbol{x}_{k-1}, k-1) + \boldsymbol{w_{k-1}} \tag{7.1}$$

In Eq. (7.1), $f(\boldsymbol{x}_{k-1}, k-1)$ refers to the state propagator and $\boldsymbol{w_{k-1}}$ is the process noise used to parametrise random disturbances. Its covariance matrix is given by $Q_k = \boldsymbol{w}_k \boldsymbol{w}_k^T$[17].

Measurements of certain quantities can be performed at specific points. This yields some kind of observables $\boldsymbol{m_k}$. They are in general arbitrary and do not need to have the same dimension as the state vector. However the state vector completely describes the system. The observables are thus related to the state by a projection operator given in Eq. (7.2) [17].

$$\boldsymbol{m}_k = h(\boldsymbol{x}_k, k) + \boldsymbol{v}_k \tag{7.2}$$

Here, $h(\boldsymbol{x}_k, k)$ is the projection operator, giving the measurement vector without any measurement uncertainties. The corresponding uncertainties are given by $\boldsymbol{v}_k$ with corresponding covariance matrix $V_k = \boldsymbol{v}_k \boldsymbol{v}_k^T$ [17].

This sets up the general framework for the KF. The KF does however generally allow the estimation of states for linear dynamic systems. Thus the linearised versions of the corresponding operators given above are used. In the case of track reconstruction, the system is not linear (see Eq. (7.15)). It can however be linearised by using a Taylor

expansion around the filtered estimate [103]:

$$f^*(\boldsymbol{x}, k) = f(\boldsymbol{x}_k, k) + F_k(\boldsymbol{x} - \boldsymbol{x}_k). \tag{7.3}$$

The linearised versions of Eq. (7.1) and Eq. (7.2) are given by Eq. (7.4) and Eq. (7.5) [17].

$$\boldsymbol{x}_k = F_{k-1}\boldsymbol{x}_{k-1} + \boldsymbol{w}_{k-1} \tag{7.4}$$

$$\boldsymbol{m}_k = H_k\boldsymbol{x}_k + \boldsymbol{v}_k \tag{7.5}$$

The propagation and projection are then determined by the corresponding Jacobi matrices [17]:

$$F_k = \frac{\partial f}{\partial \boldsymbol{x}_k} \tag{7.6}$$

$$H_k = \frac{\partial h}{\partial \boldsymbol{x}_k}. \tag{7.7}$$

There are three distinct steps to the Kalman filter: The propagation, filtering and smoothing steps. In propagation, the state is simply propagated according to Eq. (7.4). This also requires an update to the covariance matrix of the step [17]:

$$C_k = F_{k-1}C_{k-1}F_{k-1}^T + Q_{k-1}. \tag{7.8}$$

The filtering step is used to combine information from the predicted state and a measurement. Consequently, the state vector and its covariance matrix need to be updated to reflect the new measurement information. For both of these updates, the Kalman gain K_k is needed [17]:

$$K_k = C_k H_k^T (H_k C_k H_k^T + V_k)^{-}1. \tag{7.9}$$

The filtered step $\boldsymbol{x}_k'$ and its covariance matrix C_k' are then determined according to Eq. (7.10) and Eq. (7.11) [17].

$$\boldsymbol{x}_k' = \boldsymbol{x}_k + K_k(\boldsymbol{m}_k - H_k\boldsymbol{x}_k) \tag{7.10}$$

$$C_k' = (I - K_k H_k)C_k \tag{7.11}$$

Here, I refers to the identity matrix of the correct dimension. The filtered state is then used for the propagation of the next step.

The final state vector $\boldsymbol{x}_N$ and its corresponding covariance matrix contain all information on the N measurements. However, to also include the information on "future" measurements into the estimates of previous filtered steps, a smoothing pass is done [103]. This is done by going through the states in reverse order and computing the smoothed estimate

$\boldsymbol{x}_k^N$ [103]:

$$A_k = C'_k F_k^T (C_{k+1})^{-1} \tag{7.12}$$
$$\boldsymbol{x}_k^N = x'_k + A_k(\boldsymbol{x}_{k+1}^N - \boldsymbol{x}_{k+1}) \tag{7.13}$$
$$C_k^N = C'_k + A_k(C_{k+1}^N - C_{k+1})A_k^T. \tag{7.14}$$

Equation of Motion

To run the fitting algorithm, the trajectory of the particle has to be computed. There is no closed form for the trajectory of a charged particle in an inhomogeneous magnetic field[4]. This is the usual case for experiments. For Lohengrin, the inner cavity of the proposed magnet is designed such that it is mostly homogeneous. However inhomogeneities always exist and the regions at the edges of the magnet bore will always be inhomogeneous. A general fitting routine needs to be able to cope with inhomogeneous fields.

The equation of motion is parametrised by the arc length s [103]:

$$\frac{\mathrm{d}^2\boldsymbol{r}}{\mathrm{d}s^2} = \frac{q}{p}\left(\frac{\mathrm{d}\boldsymbol{r}}{\mathrm{d}s} \times \boldsymbol{B}(\boldsymbol{r})\right) = f(s, \boldsymbol{r}, \boldsymbol{d}). \tag{7.15}$$

Here, $\boldsymbol{r}$ is the cartesian position in the detector system, $\boldsymbol{d} = d\boldsymbol{r}/\mathrm{d}s$ the normalised tangent vector, and $\boldsymbol{B}(\boldsymbol{r})$ is the magnetic field at position $\boldsymbol{r}$.

Eq. (7.15) is not linear. Hence the aforementioned linearisation has to be performed. Additionally, numerical integration is done to propagate the state vector through space. This is done via a Runge-Kutta-Nyström algorithm of fourth order. The details of which can be found in e.g. [103] or [101].

7.4.3 Gaussian Sum Filter

The discussion on the fundamentals of the GSF is based on [103]. For more details, see the given reference and references therein.

The KF algorithm is optimal in the case, that all involved uncertainties can be assumed to be Gaussian [103]. Electrons for example lose energy primarily via Bremsstrahlung, which is described by the Bethe-Heitler distribution (see Figs. 7.4 and 7.5 as well as the explanation given below). This distribution is clearly non Gaussian. A track state where one assumes Gaussian uncertainties via the covariance matrix would only be able to represent this fact poorly. For this reason a modification to the already described KF algorithm exists, which is able to represent states with non-Gaussian uncertainties and process noise.

[4] In this case it has to be solved numerically [103].

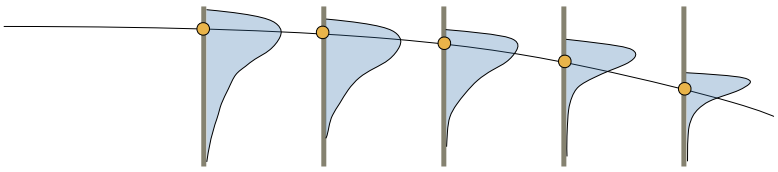

Figure 7.3: Visualisation of the idea behind the GSF. The true particle trajectory is shown in black. Measurements are shown as yellow dots. The shaded blue area indicates the Gaussian sum of the state at the site of the measurements. This distribution is no longer symmetric.

This modification is the GSF. The idea is that the state can be represented by a weighted mixture of single Gaussian states. The KF algorithm can then be used on each Gaussian component individually. This idea is visualised in Fig. 7.3. It shows the actual particle trajectory and its associated measurements. The Gaussian mixture is indicated by the shaded blue area which shows a deliberately asymmetric and non-Gaussian distribution.

Mathematical Description

A Gaussian mixture $p(\boldsymbol{x})$ is the weighted sum of normal distributions with weights w_i, means $\boldsymbol{\mu}_i$ and covariance matrices C_i [103]:

$$p(\boldsymbol{x}) = \sum_i^N w_i \mathcal{N}(\boldsymbol{x}, \boldsymbol{\mu}_i, C_i), \quad \sum_i^N w_i = 1 \ . \tag{7.16}$$

In Eq. (7.16), $\mathcal{N}(\boldsymbol{x}, \boldsymbol{\mu}_i, C_i)$ refers to a multivariate Gaussian distribution with the input $\boldsymbol{x}$ and the means and covariance matrix defined above.

Each component of the Gaussian mixture essentially transports a different track hypothesis through the detector. This means, that most considerations applying to the KF hold as the components are propagated individually. The propagation step can thus be performed as described in Section 7.4.2.

For the filtering step, the introduction of measurements is required. These can generally also be described as Gaussian mixtures. Most detectors are however constructed such that the assumption of Gaussian measurement uncertainties is a reasonable approximation. They are thus represented by a single multivariate Gaussian [103]. This also means, that the filtering step remains unchanged for each component of the Gaussian mixture and can be done according to the description in Section 7.4.2 [103].

The algorithm does apply an update to the weights when encountering a measurement. Each weight essentially determines how well each of the components represents reality. New information from the measurement thus has to be considered accordingly. The new

weights are then given by[5] [103]:

$$w_k'^i \propto w_k^i \mathcal{N}(\boldsymbol{m}_k, H_k \boldsymbol{x}_k, V_k + H_k C_k^i V_k^T), \quad \sum_i^N w'^i = 1 \ . \tag{7.17}$$

One consequence of Eq. (7.17) is, that components are exponentially suppressed with the χ^2 contribution of the measurement [103]. This emphasises the point about the reevaluation of component weights stated above.

The smoothing technique also has to be adapted. One possibility to adapt it is called weighted mean method. It relies on a backward pass of the filter, applying all the methods described above. Weighted mean smoothing just combines mean and covariance of the forward predicted and backward filter pass [103, 105]:

$$x_k^N = \left(C_k^N\right)^{-1} \left(C_k^{-1} \boldsymbol{x}_k + \left(C_k'^N\right)^{-1} \boldsymbol{x}'^N_k\right) \tag{7.18}$$

$$\left(C_k^N\right)^{-1} = C_k^{-1} + \left(C_k'^N\right)^{-1} . \tag{7.19}$$

In the version of ACTS used in this thesis, smoothing for the GSF was not yet implemented. Instead the filter is run backwards and filtered state of the backward pass is used for this purpose [103]. It is however saved as a smoothed estimate in the ACTS output files to ensure future compatibility once this is implemented.

Electron Energy Loss

The different contributions to the energy loss for electrons when traversing material (in this case lead as an example) are shown in Fig. 7.4.

Bremsstrahlung becomes by far the most dominant contribution to the energy loss of electrons above $\approx 10\,\mathrm{MeV}$. The energy loss due to Bremsstrahlung can be described by the Bethe-Heitler distribution. It gives the probability $f(z)$ for an electron to have a remaining energy fraction z after traversing t radiation lengths of material [107]:

$$f(z) = \frac{[-\ln z]^{c-1}}{\Gamma(c)}, \quad \text{with } c = t/\ln 2 \tag{7.20}$$

The remaining energy fraction z in Eq. (7.20) is defined as the ratio of the initial energy of the electron E_i (before Bremsstrahlung) and final energy E_f (after Bremsstrahlung). This distribution is shown in Fig. 7.5 for an exemplary material thickness. The approximation of the distribution with one and six Gaussians is also represented. It is evident that the Bethe-Heitler distribution is poorly represented by a single Gaussian. This would

[5] This determines them up to a normalisation factor, which is given by the second condition.

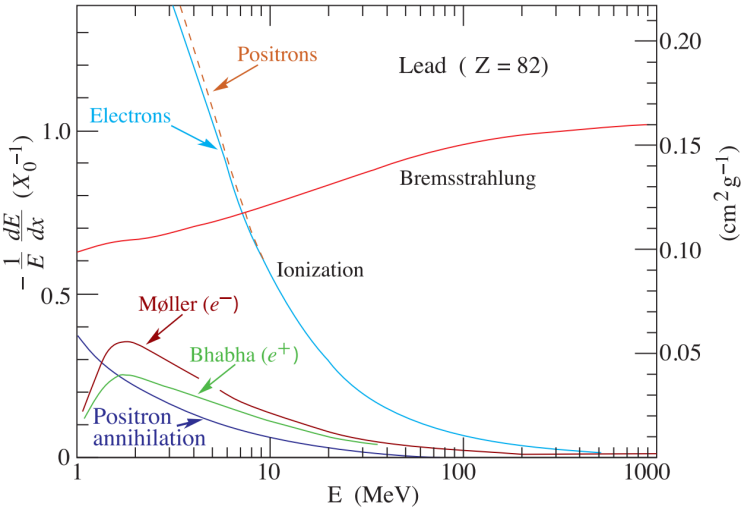

Figure 7.4: Fractional energy loss per radiation length in lead as a function of electron or positron energy. Taken from [106]

correspond to the parametrisation of the KF. The key advantage of the GSF in modelling this energy loss lies in the representation of the track state as a Gaussian mixture. When a state described by a Gaussian mixture traverses material, non-Gaussian energy loss is applied to each component. A formalism to determine the values for the Gaussian components in the Bethe-Heitler approximation is described in [103, 107] and references therein. It is not reiterated here as it is not required for the understanding of the rest of this chapter.

Assume the Bethe-Heitler distribution is approximated by N_b Gaussians and the current state of the GSF has N_c components. Energy loss is then treated by updating the components of the track state: the components of the new state are created by applying the energy loss of each Bethe-Heitler component to to each track state component[6] [103]. The new mixture thus contains $N_c N_b$ components [103].

The GSF is a computationally rather expensive algorithm (as each component can be thought of as an individual KF). An exponential increase in the number of components after each interaction with material thus has to be avoided. This is done by applying a component reduction after each each application of energy loss. The simplest form would be to just keep the N components[7] with the highest weight and omit all of the

[6] As each track state contains the full kinematic information, it also has a component relevant for the energy/momentum of the particle. The energy loss is then applied to this component.

[7] The number of components is configurable during the setup of the fitting algorithm

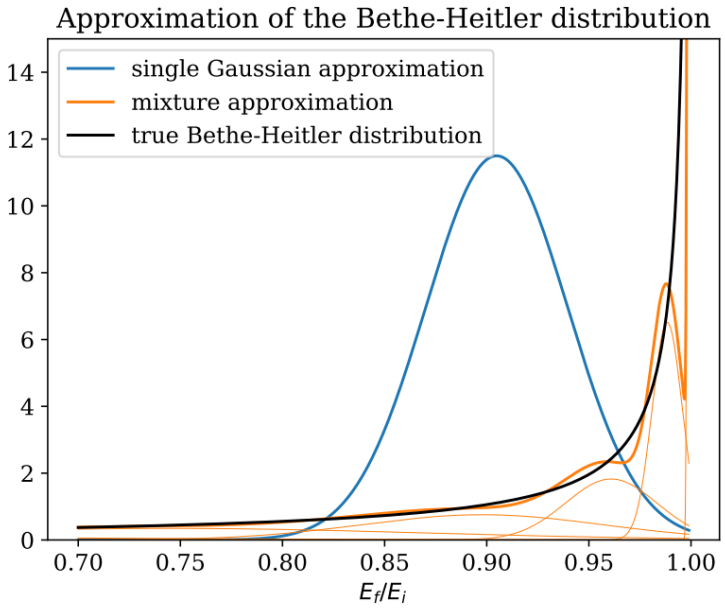

Figure 7.5: Approximation of the Bethe-Heitler distribution with Gaussian mixtures. It shows the true Bethe-Heitler distribution and an approximation with one and six components respectively. E_f/E_i represents the fraction of initial electron energy (i.e. before traversing the material) and final electron energy (i.e. after traversing the material). Taken from [103].

other components [103]. Thus keeping the total number of components in the Gaussian mixture constant.

7.5 Implementing the Lohengrin Setup in ACTS

ACTS is designed such that it can be integrated into and used directly in possibly already existing tracking frameworks [102]. This is however an involved process regarding necessary software environments, data type and coding standards. Using `ExPlORA` as an example, one of the main challenges would be differing compiler standards. ACTS makes use of the most recent features in `C++` to deliver performant code and algorithms. An inclusion into `ExPlORA` would have necessitated rewriting large parts of the `ExPlORA` codebase. Additionally, the results presented here are on the level of a feasibility study of the tracker design and the proposed experiment as a whole. The inclusion of ACTS into another software framework such as `ExPlORA` is therefore beyond the scope of this

work.

Instead, the examples framework within ACTS is leveraged to obtain a working simulation of the Lohengrin tracking detector and a resulting track fit. Nevertheless all of the necessary steps to obtain a working track fit are performed and the usage of ACTS is explained. These steps would also have to be performed if ACTS would be integrated in another simulation framework. This becomes apparent at the respective places.

7.5.1 Geometry Description

Geometry Export

The first step towards a successful track fitting routine is the implementation of experiment specific detector geometry into a tracking geometry. The geometry description of an experiment can usually be exported into some widely used format within the particle physics community. In the case of Lohengrin, a geometry description exists in `ExPlORA`. This description can be exported as a GDML [108] file. It contains the placement of all components of the detector and their associated material. As the calorimeters are not part of the tracking assembly, they are not included in this step.

ACTS natively provides support for the construction of tracking geometries from GDML files. For this reason, the tracker was assembled in `ExPlORA` and then exported into a GDML file. The trackers and the target are placed according to Table 5.1. In order to improve the coverage of the trackers for low energy electrons, their centre is placed 1 cm towards the positive x-axis. The target is a 0.1 X_0 sheet of tungsten and the trackers are a sandwich made up of 100 µm silicon and 1 000 µm polyethylene (see also Section 6.4.1).

The geometry can however not be exported directly from `ExPlORA`. The trackers are aligned along the z-axis. Consequently, this would also be the main propagation direction for a tracking algorithm. ACTS uses experience collected during the the work on reconstruction code for the ATLAS experiment [102]. Thus the coordinate system used in parts of the application is inspired by the ATLAS coordinate system. One of the variables used in this system is the pseudorapidity η as a measure of the angle between the beampipe and the y-axis [109]:

$$\eta = \ln\left(\tan\frac{\theta}{2}\right) \ . \tag{7.21}$$

The variable θ in Eq. (7.21) is defined as the angle between z- and y-axis. The pseudorapidity is a convenient choice for collider experiments, because the particle flow is constant in pseudorapidity intervals of the same size. This variable however becomes infinite for particles going along the z-axis. It is therefore advisable to rotate the geometry such that the main propagation direction is either along the x- or y-axis. Without loss of generality,

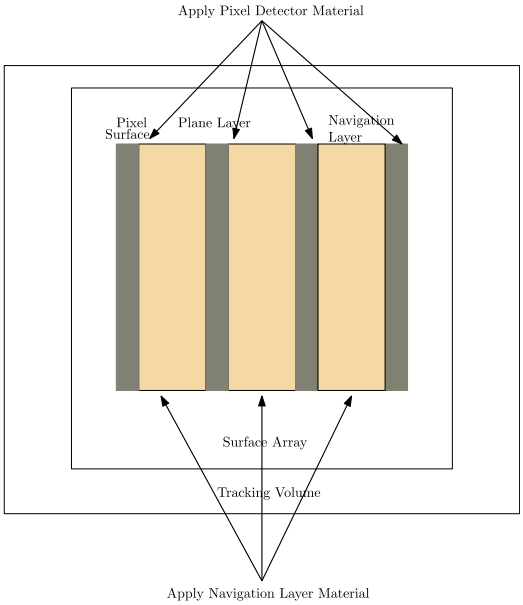

Figure 7.6: Schematic showing the contents of a simple tracking volume: Tracking layers and their connecting navigation layers are arranged in a stack. Material effects can be bound to the layers. The stack of layers is then packed inside a layer array which comprises the tracking volume.

the entire geometry is rotated around the x-axis such that the new propagation direction is along the y-axis. After that rotation is performed, the geometry is exported as GDML.

Construction of Tracking Geometry

In order to perform any kind of track reconstruction, the experiment's detector geometry needs to be converted into an ACTS tracking geometry. This is a special format and is used to tell the algorithms how to navigate through the detector. In the case of telescope detectors this is rather simple: The passive material can first be disregarded and the tracking planes are arranged in layers. A sketch showing the concept behind the tracking volume is given in Fig. 7.6. Material is classified as either passive or active. Active material is expected to provide some kind of detector response while passive material is just used to simulate particle interactions with matter without detector response.

Assuming the tracking planes are made up of pixel detectors, each tracking plane is referred to as pixel surface. These surfaces can be described as plane layers in ACTS. However, each tracking plane can consist of many surfaces. This might be the case if each tracking plane is made up of multiple chips. Each tracking plane is thus described as an

array of surfaces - the surface array (note that this can also contain just one entry).

Different pixel layers are connected by navigation layers. The stack of layers can then be represented by a layer array. The encompassing tracking volume then contains this layer array. Material can be bound to the layers. If this is done the possible effects the material could have on particles are applied at this layer. More information on this can be found in Section 7.5.2.

The example framework within ACTS comes with code to build a generic telescope like tracking geometry based on inputs. It is possible to use this as a starting point to write a specific `C++` class for the own geometry. One advantage is that this tracking geometry class can then later be used in a desired simulation framework and also within the ACTS examples by adding a `Python` binding. `Python` bindings are a way of interfacing the `C++` code of ACTS with simple standalone scripts which can be completely written in `Python`.

The Lohengrin tracking geometry was realised as a `C++` class with its own `Python` binding allowing for maximum flexibility in the usage of the ACTS examples framework. The tracking geometry can be created on demand by providing the respective GDML input file.

It has to be noted, that ACTS is going to move to a different navigation scheme. The plan is to move from surfaces to volumes for the navigation algorithms. While work is actively being done on this rewrite, it is not yet production ready [101]. The creation of tracking geometries will thus have to be adjusted in the future.

7.5.2 Material Handling

ACTS provides a sophisticated way to handle the description of material inside the tracking geometry. A summary with the focus on points relevant for the specific implementation of Lohengrin is given here. More information can be found in [101].

The input GDML can usually not directly be used to build a material map in ACTS. This is because each change in material requires a step to be taken. Otherwise it would not be possible to determine how much material a particle has traversed along its trajectory. However this is computationally expensive, especially for complicated detector geometries with many parts and material transitions. For this reason, a simplified material map has to be created in ACTS. The concept is visualised in Fig. 7.7.

The passive components of the detector are summarised into a representative layer, which contains the material. A precise description of the active layers is required as they contain the measurements. A simplification can however be done for the passive detector elements. During the tracking, effects related to interactions within the material are then only applied when crossing this representative layer. The degree of simplification is defined by the user and typically a trade-off between performance and modelling accuracy.

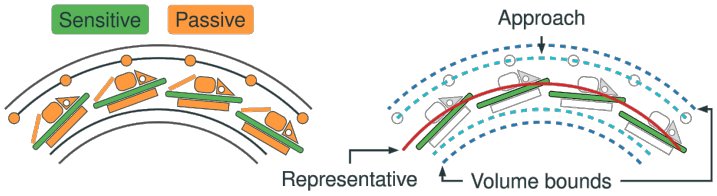

Figure 7.7: Idea of the simplified ACTS material map. Several parts of the detector can be summarised into one layer, which contains the combined material of the original geometry. Taken from [101].

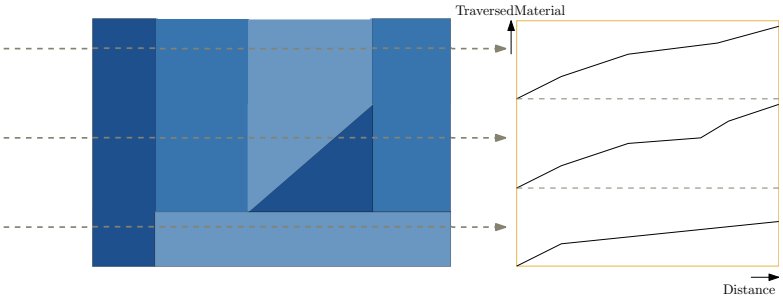

Figure 7.8: Idea behind the geantino scan in ACTS. Each geantino accumulates the amount of material traversed, which is shown on the right. Dense materials are depicted in darker shades of blue. Both distance and material are given in arbitrary units.

How the simplification is done in detail, is described in [101].

For Lohengrin, the representation of the tracking layers is very simple. Each tracking layer only consists of three components: the active silicon layer, the passive polyethylene layer, and the air between the current and the next tracking plane. A further simplification into representative layers is therefore not required and the material from the GDML is bound to the respective layers directly.

In order to check whether the tracking geometry accurately reflects the material distribution of the detector, ACTS provides the geantino scan. The concept is visualised in Fig. 7.8.

Geantinos are fictitious particles provided by `Geant4`, which do not interact with matter. They do however record how much material they traversed along their trajectory. This allows for a comparison of the material description in the tracking geometry and the original GDML file. Geantino scans are performed for both and the result is shown in

Fig. 7.9. It shows the encountered material along the geantino propagation direction[8]. Different parts of the detector (tagging tracker, recoil tracker and target) are colour coded. This allows for an easy identification of the impact of different detector components on the total material budget. "Geant4" geometry shows the geantino scan based purely on the provided GDML with full detector information. "Tracking Geometry" shows the result of the geantino scan of the tracking geometry constructed from the GDML file. The material matches well, which is expected due to the simple construction of the tracking layers.

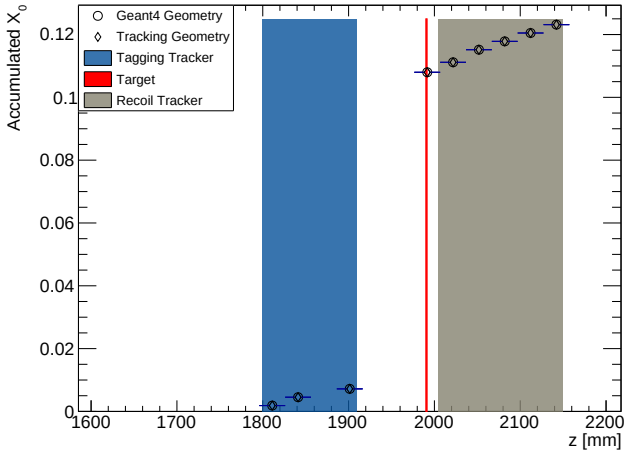

Figure 7.9: Material along the propagation direction. Compared is the material encountered by just reading the GDML with full information about the detector construction, and the material as it is described in the tracking geometry and thus also used for the resulting track fit. Also available in [10].

Remarks on the Material Validation for Telescope Detector Geometries

The geantino scan in ACTS is usually represented as material encountered along one of two coordinates (usually η and ϕ - See [109] for the ATLAS coordinate system and also Section 7.5.1 for an explanation of η) representing the direction from the interaction point. This also ensures, that the geantinos have traversed the entire detector. One then obtains the distribution of material based on directions from the interaction point.

[8] ACTS requires a rotation of the geometry around the x-axis, making the y-axis the propagation direction within ACTS. For the purpose of Fig. 7.9, the propagation direction is referenced as z-axis. This ensures consistency with the rest of the thesis.

For a telescope-like geometry, this is not an adequate choice. The detector covers only a small solid angle around an "interaction point" or origin of the coordinate system[9]. It is much more natural to show the material along the propagation direction, which is how it is also displayed in Fig. 7.9. For this reason the geantino scan in ACTS was modified to include information on the material along the propagation direction.

If a geantino scan is taken where the geantinos traversed the entire detector, it is possible to compare the tracking geometry to the GDML description by looking at the ratio of both geantino scans (ratio plot). This is possible, because the entire material along one direction was integrated. However, this approach is not feasible when the material is displayed along the propagation direction. The reason is that it is not possible to ensure that geantinos performed the same steps across the two simulation runs[10].

7.5.3 Simulation Setup

The `Geant4` simulation is set up with the tracking geometry described in Section 7.5.1. The added `Python` binding to the Lohengrin tracking geometry allows for a seamless integration into the ACTS examples framework. This already contains a collection of code and useful routines for the setup of a simulation.

Particle Emission

The main focus of this study is to determine the tracking capabilities over a large range of momenta behind the target. The energy resolution from ELSA is much better, than the resolution which would be achievable with particle tracking (see Section 3.1). For this reason, the trackers before the target are not considered in this study. Instead the electron beam starts just behind the target.

A configurable particle cannon is provided by the examples framework in ACTS. The origin is set to the centre of the back surface of the target. The momentum is sampled from a uniform distribution between 25 MeV and 500 MeV and 500 000 electrons are shot along the propagation direction.

It is understood, that this includes many simplifications concerning the distribution of beam electrons in the final setup and that the size of the simulation sample can be increased. The goal of this chapter however is to obtain an estimate of the capabilities of the proposed tracking setup. Observing the performance in isolation with a uniform distribution of that many electrons allows for such an estimate without the inclusion of

[9] In fact, there would be multiple sensible definitions for an origin of the coordinate system for a telescope detector geometry, like the end of the accelerator or the beginning of the tagging tracker

[10] This was the result of personal communication with Andreas Salzburger.

other effects. The actual distribution expected in the experiment can be folded into this at a later point.

Magnetic Field

The magnetic field can be provided either by a field map or by choosing one of the pre-existing configurations from the ACTS examples framework. Since the trackers behind the target are located well inside the magnet bore, it is reasonable to assume a constant magnetic field of 0.9 T over the length of the tracking assembly. A completed magnet and thus a field map also does not yet exist for LOHENGRIN.

Particle Smearing

Individual pixels are not simulated with this setup. Instead hits are built from energy deposits by using a smearing algorithm provided by ACTS. During the digitisation, the digitised position of the hit is smeared by a uniform distribution in both lateral directions with a standard deviation of $33.04\,\mu\text{m}/\sqrt{12}$. This corresponds to the resolution of one pixel. While being a simplification, this is also a conservative estimate. The resolution is expected to improve with a full simulation of pixels and a dedicated clustering algorithm.

Pattern Matching and Seeding

ACTS provides several choices of algorithms for pattern matching and seeding. In this case the `TruthEstimated` algorithm is used. This algorithm uses truth information for pattern matching. Single electrons are expected to pass through the detector in each event. This drastically simplifies the pattern matching aspect as hits generally belong to that single electron track. It is therefore reasonable to assume, that this choice does not introduce unrealistically high seeding efficiencies [10]. The starting values for the track state (seed) are estimated based on the first three hits in a track. No truth information from the simulation is used in estimating the starting values of the track seed. The estimate is obtained purely from the positions of the hits.

Gaussian Sum Filter

The GSF uses all of the information from the hits and seed to perform the track fit. The number of components is set to six and the mixture is reduced by discarding the lowest weight components.

As an illustrative example, a filtered track state at the last tracking layer is shown in Fig. 7.10 as debug output. The Gaussian mixture representing the track state is shown for each of the parameters. Noteworthy is the asymmetric distribution in *qop* (lower middle in

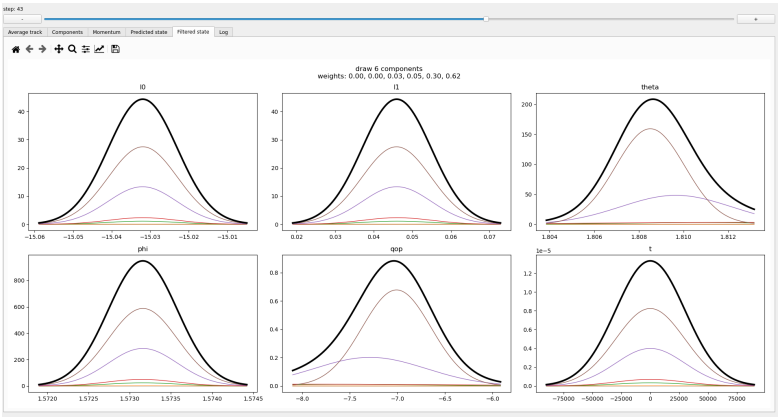

Figure 7.10: GSF debug output showing the filtered track state as a Gaussian mixture at the last tracking layer.

Fig. 7.10). In ACTS the momentum is represented in the track state in terms of curvature of the track (charge/momentum). Hence *qop* is the parameter responsible for the electron momentum (shorthand for q over p). The individual Gaussians are shown in colour, whereas the mixture is shown as solid black curve. It clearly shows the effect of different track hypotheses being used in the Gaussian mixture to produce a more complex overall distribution.

7.6 Tracking Performance and Comparisons

This section collects and discusses the main tracking results from the simulation set up according to Section 7.5.3. Fig. 7.11 shows a histogram of the reconstructed momentum[11] and the true electron momentum for a uniform distribution of electrons between 25 MeV and 500 MeV. Fig. 7.12 depicts the corresponding tracking efficiency. The tracking efficiency is defined as the ratio of reconstructed tracks to total tracks. It is less than or equal to one. The efficiency decreases if no viable track can be reconstructed from an electron. Such a scenario might occur if, for example, less than three tracking layers were hit and thus no seed for the track fit could be determined.

The tracking efficiency stays almost constant and close to one for a large part of the observed momentum range. It decreases sharply for low momentum electrons as the radius of curvature eventually becomes too small to facilitate a track fit. The tracking efficiency for higher momenta than 500 MeV is expected to behave similarly as there is no

[11] As the GSF is used here, this means the smoothed value in the ACTS output file.

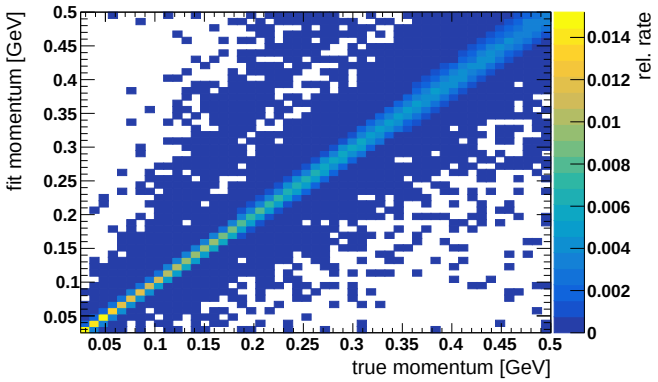

Figure 7.11: Fitted and true momentum for a uniform distribution of electrons between 25 MeV and 500 MeV. Also available in [10].

problem concerning the radius of curvature of the electrons. This is expected to improve with future work on the optimisation of positioning and size of the tracking layers [10].

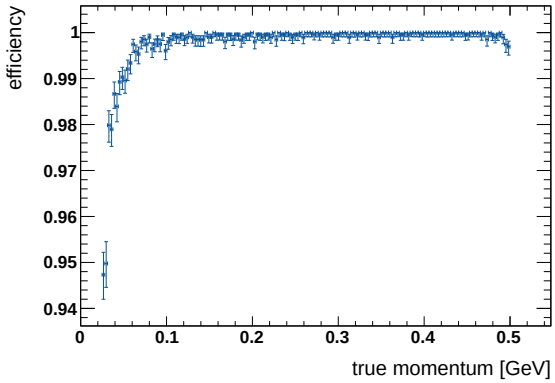

Figure 7.12: Tracking efficiency for a uniform distribution of electrons between 25 MeV and 500 MeV. Also available in [10].

Fig. 7.11 shows a nice correlation between fitted and reconstructed momenta over the entirety of the examined momentum range. The results are shown without any quality cuts applied as such a criterion is difficult to define for a GSF [10, 103]. Noteworthy are

the regions far off the diagonal: these contain potential for fake signal events, because they imply a large difference between fitted and true electron momentum. This is especially problematic in case a high momentum electron is reconstructed to have a low momentum. This would correspond to the lower right portion of the plot. An explanation along with potential solution strategies are given in Section 7.6.1.

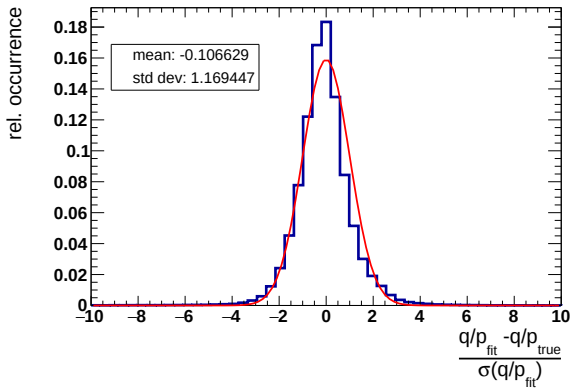

Figure 7.13: Pull of the reconstructed charge/momentum (q/p) at the target with fitted Gaussian.

Fig. 7.13 shows the pull of the parameter in the state vector, used to encode the electron's momentum[12]. The pull of a variable α is defined as [103]:

$$\text{pull}_\alpha = \frac{\text{res}_\alpha}{\sigma_{\alpha_{\text{fit}}}}, \text{ where} \tag{7.22}$$

$$\text{res}_\alpha = \alpha_{\text{fit}} - \alpha_{\text{true}} \ . \tag{7.23}$$

It is the ratio of the residual res_α and the uncertainty of the fit $\sigma_{\alpha_{\text{fit}}}$. The residual is the difference of the fitted and true value. If the fit has no bias and all of the uncertainties were estimated and propagated correctly, the resulting distribution is a normal distribution. There is a bias towards negative values and the distribution is too sharp and has more significant outliers than a normal distribution. This is a behaviour, which was also observed in [103]. This might be improved with updates to the ACTS code base, which could easily be implemented in the workflow described in this chapter.

[12] The parameter in the state vector which describes the momentum is actually charge over momentum (q/p). As this is the fitted value, this is shown in the figure.

Comparison of Different Tracking Layer Thicknesses

A useful figure of merit to get a general idea of the tracking capabilities of relative resolution σ_p/p [98]. This is estimated in momentum bins by:

$$\frac{\sigma(\text{res}_{p_{\text{fit}}})}{p_{\text{true}}}. \tag{7.24}$$

This is depicted in Fig. 7.14. It shows this relative resolution for three different scenarios:

- Small material budget scenario: trackers consist of a sandwich of 50 µm silicon and 0 µm polyethylene.
- Normal material budget scenario: trackers consist of a sandwich of 100 µm silicon and 1 000 µm polyethylene.
- Large material budget scenario: trackers consist of a sandwich of 400 µm silicon and 1 000 µm polyethylene.

This allows for an estimation of the tracking capabilities of this setup in extreme cases compared to the normal scenario. The large material budget is a pessimistic scenario, where the thickness of the silicon part of the tracking layers is increased by a factor of four. The thin material budget scenario represents an optimistic case, where most of the support structures can be removed and very thin monolithic tracking sensors provide useful detection efficiencies. The normal scenario represents a realistic case, where the values of the layers are inspired by existing values for pixel detectors (see also Section 3.4.2).

This figure of merit can be used to compare the resolution achieved with this setup to a rough estimate of what could be achieved theoretically. This estimation was done in [110] and is summarised in [98]. In the momentum regime considered here, the resolution is dominated by limitations arising from multiple scattering. Assuming evenly spaced tracking layers, propagation perpendicular to the magnetic field, and an average of five tracking layers being hit one obtains [98, 110]:

$$\frac{\sigma_p}{p} = \frac{0.0136\,\text{GeV}}{0.3B[T]L[m]}\sqrt{\frac{L}{X_0}1.26}\,. \tag{7.25}$$

In Eq. (7.25) the magnetic field has to be used in units of T and the length of the tracking assembly L has to be used in m and units of radiation lengths of the tracking assembly. Assuming a length L between 7 cm and 10 cm[13] one obtains the following estimates for

[13] This depends on the number of tracking layers being hit. This is in general different for each electron and the values given here provide estimates which are valid for most cases.

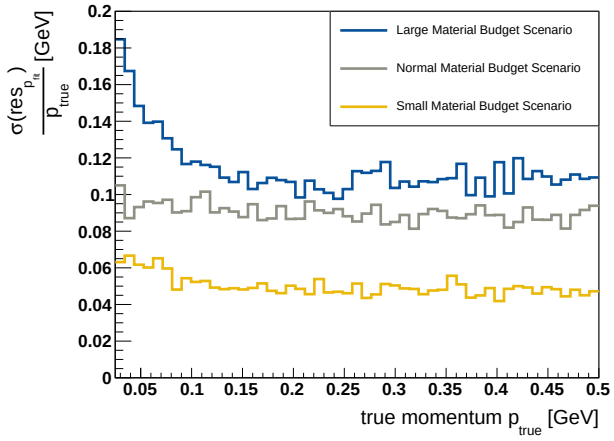

Figure 7.14: Relative resolution of fitted momenta for different true momenta and possible tracker configurations considering the total material budget. The legend is to be interpreted as follows: 400 µm(100 µm) silicon and 1 000 µm polyethylene for the large (normal) material budget scenario and 50 µm Silicon and 0 µm polyethylene for the small material budget scenario. Also available in [10].

σ_p/p [10]:

- Small material budget scenario: ≈ 3 to 5 %.
- Normal material budget scenario: ≈ 8 to 10 %.
- Large material budget scenario: ≈ 11 to 17 %.

These values are mostly reproduced in Fig. 7.14. It should be noted, that also tracks with fewer than five tracking layers are included in this figure. This changes some values in Eq. (7.25), notably the length L. This becomes evident in particular for electrons toward the lower end of the studied momentum range and the large material budget scenario. Thereby clearly demonstrating the effect of multiple scattering on the momentum resolution [10].

7.6.1 Addressing the Potential for Fake Signal Events

The Lohengrin experiment needs a reliable way to differentiate low- and high momentum electrons. A signal region is defined in Section 8.1, where the electron needs to have, among other cuts, a momentum/energy < 75 MeV. As already mentioned in Section 7.6, there exists a potential for fake signal events in the lower right part of Fig. 7.11. Events where the track fit resulted in a comparatively low momentum even though the true

momentum is high (i.e. the lower right area) were examined individually and their exact kinematics studied by stepping through the GSF fitting routine layer by layer. It was found that those events are caused mainly by significant Bremsstrahlung occuring in the second and third layer behind the target. Here "significant" means, that the electron loses the majority of its initial energy in this single interaction.

If the significant Bremsstrahlung event happens in the second layer behind the target, the additional curvature is only registered in the third layer (i.e. the next measurement surface). It works completely analogously for Bremsstrahlung happening in the third layer behind the target. The first three hits are used for the seeding algorithm, which determines the starting values for the fit. If such a Bremsstrahlung event occurs, the seeding algorithm initialises with values which are consistent with a different track hypothesis as the radius of curvature changes abruptly either outside of the range of the seeding algorithm or for the last point used to obtain initial values. In these cases the initial values for the track fit are far off the true values and the fit returns an inadequate result. This is expected to be addressed in potential future work being done on the seeding algorithm which extends the functionality to the specifics of electron tracking. It should also be noted, that the ECAL is likely to detect the created Bremsstrahlung photon, decreasing the severity of these events. They become problematic, if no viable mitigation strategy can be found and a significant number can not be vetoed by the ECAL.

Nevertheless an attempt is made at reducing these events. The following cuts are applied to the sample from Fig. 7.11:

- The fitted momentum has to be larger than 0 MeV. This eliminates cases, where the fit returns an obviously nonsensical result.
- The ratio of initial(fitted momentum in the first layer) and final momentum (fitted momentum in the last layer) has to be smaller than two. This eliminates tracks with a large discrepancy of momenta in the beginning and end of the tracker, indicating the possibility for a significant Bremsstrahlung event described above.
- The maximum residual in the x-direction in all of the tracking layers is smaller than 1 cm. This eliminates tracks with a large discrepancy between predicted deflection from the fit and actual measurement. This might also indicate a problematic track fit.

It has to be emphasised, that these cuts are not optimised. They serve merely as a first look into what a potential cut-flow could look like if it is employed for Lohengrin. They have to be optimised and have to be evaluated in more detail if such an approach is chosen for the final Lohengrin reconstruction chain. Implementing these cuts preserves about 97 % of events. All of the events examined by hand were eliminated by applying the

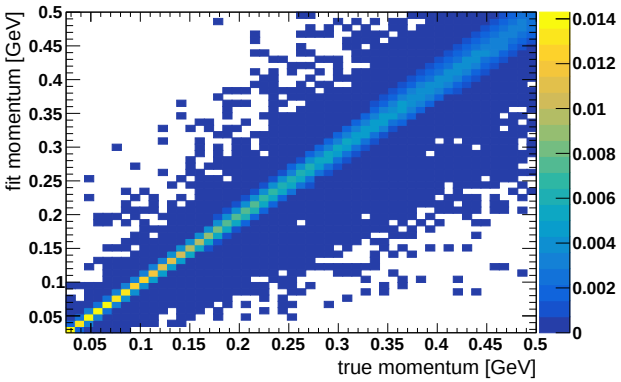

Figure 7.15: Fitted and true momentum for a uniform distribution of electrons behind the target between 25 MeV and 500 MeV. Cuts have been applied for this figure.

aforementioned cuts. Implementing these cuts and plotting the fitted and true momentum in a histogram yields Fig. 7.15.

The problematic areas are far less populated than in Fig. 7.11. This demonstrates, that these events can be addressed either by improving the seeding algorithm or introducing suitable cuts.

7.6.2 Comparison to a Kalman Filter

The GSF is a more general version of a KF. More specifically, running a GSF with just one component can be considered as a KF which estimates the energy loss by the mean and standard deviation of the Bethe-Heitler distribution [103]. Given the infrastructure set up in this chapter, it is therefore rather trivial to run a KF with the same simulation parameters as given above. The fitted and true momenta are shown in Fig. 7.16 and the pull is displayed in Fig. 7.17.

The distribution in Fig. 7.16 is visibly broader than in Fig. 7.11. There is however also a noticeably strong correlation of fitted and true momenta. The pull has a larger bias, but a standard deviation closer to one. This also indicates that a pure KF is worse at reconstructing the electron momentum albeit with better estimated uncertainties. It was however already shown, that the KF performs significantly worse than the GSF for higher electron momenta [103]. The KF does provide a significant performance advantage as the GSF is essentially running multiple KFs in parallel [103].

Which of the two algorithms ends up as the one used for the Lohengrin reconstruction

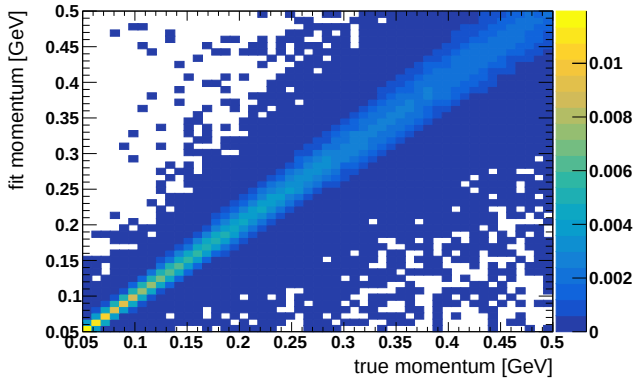

Figure 7.16: Fitted and true momentum for a uniform distribution of electrons behind the target between 25 MeV and 500 MeV using a single component GSF.

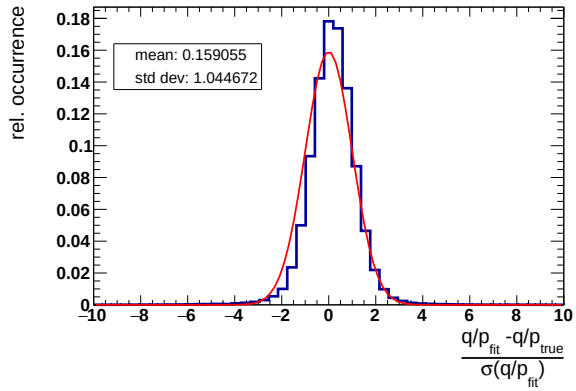

Figure 7.17: Pull of the reconstructed charge/momentum (q/p) at the target for a single component GSF with fitted Gaussian.

chain remains to be seen. The performance benefits of the KF might be the key advantage. The better tracking resolution of the GSF might be worth the additional computing cost. A combination of both fitting algorithms might also be used for different aspects of the reconstruction chain.

7.7 Conclusion of the Tracking Studies

This chapter introduces the basic idea and concepts behind the tracking for Lohengrin. The KF and GSF are introduced as viable tracking algorithms. The GSF caters specifically to electron tracking as it is able to deal with non Gaussian process noise. This allows for a parametrisation of electron energy loss. The KF offers performance improvements as it is the more lightweight algorithm. For the final sensitivity estimate in Chapter 8 and [10], the tracking efficiency and reasonable momentum reconstruction down to 25 MeV of the GSF are used as computational cost was not the primary limiting factor for the level of this study.

ACTS is introduced as toolkit to perform the first iteration of tracking for Lohengrin. The experimental setup is prepared and included into ACTS. Steps specific to the inclusion of the Lohengrin geometry are highlighted. The general workflow for handling material in a tracking geometry is described and the Lohengrin tracking geometry material is validated.

The tracking results are studied and compared to theoretically achievable values. Potential outliers, which could be a source for fake signals, are addressed. The tracking resolution obtained with this setup matches with the resolution one would expect theoretically. It can therefore be concluded that the tracking, as it is described in this thesis, can in principle be performed with ACTS, also down to momenta of 25 MeV. It therefore provides a feasible base for the overall sensitivity estimate in Chapter 8 and [10].

Chapter 8

Combined Sensitivity Estimate

This chapter ties together the previous work described in this thesis by providing a sensitivity estimate of the proposed experiment based on the capabilities of the detector components. It is a summary of the sensitivity estimate given in [10]. Key points and results are reiterated here for completeness. For more information see [10]. A layout optimisation concerning the dimensions and properties of magnet and ECAL has been performed in [10]. This optimisation is not reiterated here. The discussion here is limited to the baseline scenario in [10]. This corresponds to the setup and description of detector components as they are written in the rest of this thesis. The most important parameters for this chapter are (non-exhaustive) [10]:

- The trackers are placed according to Table 5.1 and Section 7.5. For the trackers behind the target, this means they are placed at distances of (1, 3, 4.5, 7, 10, 13) cm from the target.
- The magnet has a strength of 0.9 T over a length of 1 m behind the target. It is assumed to be homogeneous. The opening of the magnet has a diameter of 20 cm, such that the opening angle measured from the target is 0.1 rad. This value effectively provides a cut on the solid angle in which photons can be measured.
- The ECAL is placed at a distance of 3.5 m from the target. It has a size of $48 \times 48\,\mathrm{cm}^2$.

8.1 Defining a Signal Region

The baseline analysis of LOHENGRIN is designed to be a counting experiment in a predefined signal region, maximising the sensitivity for dark photons in the mass window $m_{A'} \in [1\,\mathrm{MeV}; 40\,\mathrm{MeV}]$ [10]. The experiment in general and the signal region in particular is designed such that the rejection of SM events is maximised. Rare SM processes however

can mimic background events [10]. A description of the estimation of such backgrounds for the sensitivity estimate is given in Section 8.2.

The signal region for LOHENGRIN is defined by [10]:

- The presence of exactly one beam electron in the initial state. This is inferred from hits in the tagging tracker.
- The presence of exactly one (baseline candidate signal region) or at most one (second candidate signal region) electron in the final state. This is inferred from hits in the recoil tracker.
- No significant energy deposition in the ECAL (<640 MeV above the photon pedestal)
- The absence of any hadronic activity in the final state
- The absence of any charged tracks apart from the signal electron final state

Here, a signal electron is defined as a charged track that is compatible with an electron hypothesis and meets the following selection cuts [10]:

- $25\,\text{MeV} < E < E_{\text{e,cut}} = 75\,\text{MeV}$. The cut requiring electrons to have a higher energy than 25 MeV accounts for the limited tracking efficiency for electrons below that value (see also Section 7.6).
- $\theta < \theta_{\text{e,cut}} = 0.25\,\text{rad}$

Here, θ_e is the scattering angle of the electron just behind the target. This value is chosen, because it is approximately the maximum angle at which electrons can still be feasibly tracked [10]. Given the foreseen ECAL design and the high rate of electrons on target, the energy measured in the ECAL for an event passing the trigger will be subject to a substantial background pedestal from SM Bremsstrahlung events [10]. This is discussed in Section 6.5.2. The cut on the measured energy in the ECAL for events with low energy electrons in the final state has to be significantly higher than the average value of this pedestal in order to preserve as much signal as possible and completely suppress any SM background [10]. The HCAL is used to veto any events with hadronic activity in the target. An accurate energy measurement is not needed. A low noise HCAL is used to efficiently veto any events in which the total energy that is measured in the hadronic calorimeter that can not be interpreted as the extension of a shower that started in the ECAL is above a low threshold. This allows the implementation of a relatively small HCAL around the ECAL [10]. The tracking information can be used to veto any event with additional tracks apart from the track created by the signal electron [10].

8.2 Background Estimation

SM backgrounds are estimated depending on the mechanism responsible for them passing analysis cuts. Three cases of backgrounds are considered in [10] and here:

- Out-of-acceptance backgrounds: These arise from the limited coverage of the detector. High energy Bremsstrahlung photons that are emitted at large angles can miss the ECAL, leading to a large amount of missing energy. These comprise the dominant background contribution [10].
- Neutral hadrons: These backgrounds arise from the production of of neutral hadrons in the target or the first layers of the ECAL. Stable neutral hadrons like long lived kaons and neutrons can escape the experiment if they miss the HCAL or only deposit little energy in the ECAL [10].
- Neutrino backgrounds: Neutrinos can be produced through the interaction of final state particles with matter in the tracking detector or calorimeter. In the case of high energy neutrinos, this can lead to a significant amount of missing energy. They are not expected to play a significant role for the planned 4×10^{14} electrons on target for LOHENGRIN [10].

8.2.1 Out-Of-Acceptance Backgrounds

These have been estimated based on theoretical modelling of SM Bremsstrahlung (for more info on this process see [10]). Additional assumptions have been made to obtain the number of remaining background events. The ECAL is assumed to have a size of $48 \times 48\,\mathrm{cm}^2$ (Baseline). This also corresponds to the size of the Baseline ECAL in the hit distribution studies of Section 6.4.2. Another case is studied where the ECAL is extended and covers the entire opening angle of the magnet for $|\phi| > \frac{\pi}{4}$[1](Extended). This also corresponds to the size of the Extended ECAL in the hit distribution studies in Section 6.4. For 4×10^{14} electrons on target, 293 (82) out-of-acceptance backgrounds remain for the baseline (extended) calorimeter scenarios. This illustrates the extreme importance of the angular coverage of the ECAL[10].

8.2.2 Hadronic Backgrounds

Hadronic backgrounds are harder to estimate for several reasons. The cross sections for the relevant interactions are small, and usually a large number of neutral and charged

[1] $|\phi|$ denotes the absolute value of the azimuthal angle in a spherical coordinate system. It is given by: $|\phi| = \arccos \frac{x}{\sqrt{x^2+y^2}}$, where x, y, z represent the usual Cartesian coordinates.

particles emerge from the reaction. The master's thesis by Laney Klipphahn deals with a the estimation of neutral hadronic backgrounds in more detail as simulation results using `Geant4` are not always reliable (see below). Four different classes of events are considered in [10]:

Electro-nuclear interactions in the target The incident electron transfers a large fraction of it's energy to the target nucleus, thereby emerging from the target with a very low momentum and not having radiated a real photon. The target nucleus is expected to break up in most of these cases emitting nucleons with significant energy. A sample was simulated with `Geant4` and no event passed the signal region cuts. The simulation with `Geant4` is however not reliable due to the low recoil electron energy cut. Nevertheless it is assumed that this background can be well suppressed [10].

Electro-nuclear interactions in the tracker or ECAL With thin silicon tracking planes, the probability for an electro nuclear interaction that leaves no energy in the calorimeters is very low. Such interaction is more likely to happen in the ECAL. The bulk of scattered electrons is however bent around the ECAL. For the case discussed here, about 0.5 % of electrons still hit the ECAL. Compared to electro-nuclear interactions in the target, these reactions are suppressed by additional factors from happening in the ECAL: if the interaction occurs in the ECAL, the electron must have had a high energy, and the tracking algorithm must have failed to find the track. It is unlikely for such an event to pass all signal region cuts [10]. The same argument holds for interactions in the tracker. Only events where the electro-nuclear interaction occurs in one of the first two planes are unlikely to pass the signal region cuts [10]. This contribution is hence assumed to be almost negligible [10].

Photo nuclear interactions in the target and tracker A simulation of 1×10^7 events being shot at the target was performed. No event with a photo-nuclear interaction passes the signal region cuts [10].

Photo-nuclear interactions in the first layers of the ECAL A simulation of this class of events was done using a photon beam and the previously determined detection efficiency of the HCAL (see Section 6.6). No event passed the signal region cuts [10].

The overall number of background events is assumed to be dominated by SM Bremsstrahlung, where the photon misses the ECAL [10]. Due to a lack of a precise estimate of the remaining backgrounds, apart from the considerations given above, a contamination of 10 additional background events in the signal region is assumed [10]. This is considered to be a conservative estimate [10]. A considerably higher number of background events

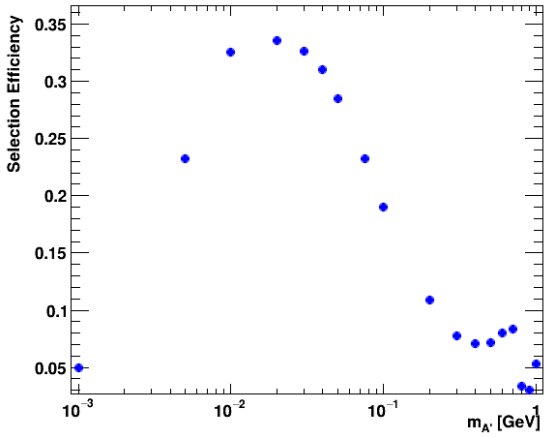

Figure 8.1: Expected selection efficiency for a range of dark photon masses. See also [10].

would decrease the discovery potential for LOHENGRIN significantly. If it turns out to be necessary, additional veto detectors like an additional HCAL can be added to the experiment [10].

8.3 Signal Efficiency

The selection efficiency depends on the kinematics for the electron. Simulations based on theoretical calculations (see [10] for details) have been performed to determine the expected number of dark photon events in the signal region. For electrons with an energy between 25 MeV and 75 MeV, the average trigger efficiency for $\theta_e < 0.25$ rad is 99 % and the average tracking efficiency is 98 %.

The selection efficiency (with trigger and tracking efficiency) for signal events is shown in Fig. 8.1. It is dominated by the trigger efficiency for low dark photon masses. For high dark photon masses the recoil energy spectrum is shifted towards low values, which limits the tracking efficiency [10].

8.4 Sensitivity Estimate

It is now possible to provide a sensitivity estimate for the LOHENGRIN experiment based on the considerations in previous parts of this thesis. Two distinct signal regions are considered (see also Section 8.1): A baseline candidate signal region and a second candidate signal region. The second candidate signal region is a more aggressive signal region.

It enhances the selection efficiency for signal events, but might lead to an unacceptable number of background events if the veto efficiency for high energy electrons is not close enough to 100 % [10]. This region is included, because it provides insight into the physics potential for the case that the lower threshold for electron tracking can be reduced compared to the benchmark value of 25 MeV.

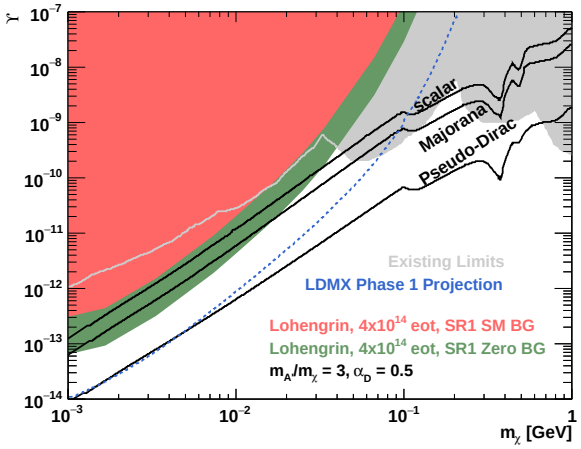

Figure 8.2: Estimated sensitivity of the Lohengrin experiment for the extended ECAL coverage and the baseline signal electron phase space. The red area shows the expected sensitivity including the estimated number of background events, the green area indicates the statistical limit for the sensitivity assuming a background free search (both limits are calculated at the 90% CL). The gray area shows existing limits from various experiments - this information is taken from [111] and includes limits from LEP [70–72], BaBar [73], MiniBooNE [52], NA62 [74], LSND [75], NA64 [49] as well as CRESST II [76], CRESST III [77] and XENON1T [78]. In blue the expected limit from Phase 1 of LDMX is shown [112]. Taken from [10].

The two different scenarios for the ECAL (baseline and extended) are also considered. The expected sensitivity for the baseline signal region and the extended ECAL is shown in Fig. 8.2. With a foreseen 4×10^{14} electrons on target, Lohengrin would be able to probe the dark sector parameter space just up to the expected properties for scalar dark matter, assuming 2 MeV $\lesssim m_\chi \lesssim$ 10 MeV and $m_{A'}/m_\chi = 3$ [10].

The expected sensitivity for the second candidate signal region is shown in Fig. 8.3. If this approach is viable, it has the potential to close the gap to Pseudo-Dirac dark matter, given a longer run time with more electrons on target [10]. A comparison to the expected sensitivity of Phase 1 of LDMX is shown in addition. LDMX uses a higher beam energy. For a similar number of electrons on target, this yields a substantially larger dark photon phase space, which LDMX is sensitive to [10].

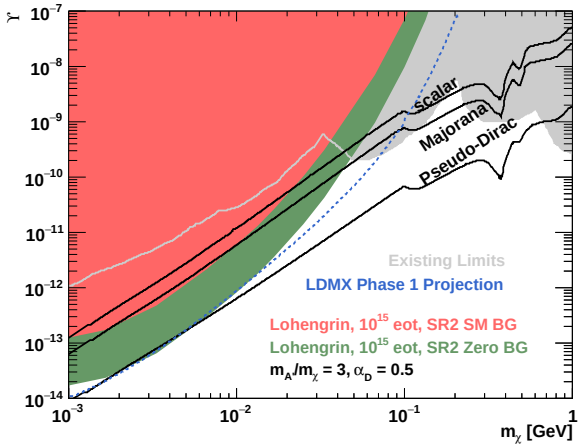

Figure 8.3: Estimated sensitivity of the Lohengrin experiment for the extended ECAL coverage, an extended beam time and the more aggressive signal electron phase space. The red area shows the expected sensitivity including the estimated number of background events, and the green area indicates the statistical limit for the sensitivity assuming a background free search (both limits are calculated at the 90% CL). The gray area shows existing limits from various experiments, in light blue the expected limit from Phase 1 of LDMX is shown. Taken from [10].

In addition to the backgrounds discussed in this chapter, also an optimistic zero background case is shown in Fig. 8.2 and Fig. 8.3. This shows the potential assuming a significant improvement in the background suppression. Assuming this optimistic scenario, Lohengrin could achieve a similar sensitivity as LDMX Phase 1 for a part of the phase space with a moderate increase in luminosity [10].

If α_D is varied, the relic targets move accordingly. The sensitivity of Lohengrin however depends only on ε due to it relying on a disappearance based experimental technique. The expected Lohengrin limits therefore scale with α_D in this parameter space [10]. This is in contrast to other planned experiments like SHiP. The SHiP collaboration has published expected limits for $\alpha_D = 0.1$ in [113]. The expected sensitivity for Lohengrin is compared to the one published by SHiP in Fig. 8.4. This figure assumes extended ECAL coverage, the more aggressive signal region, and a higher luminosity corresponding to 1×10^{15} electrons on target [10]. It can be seen, that Lohengrin is competitive and might even outperform SHiP for dark photon masses below 30 MeV for the zero background case [10].

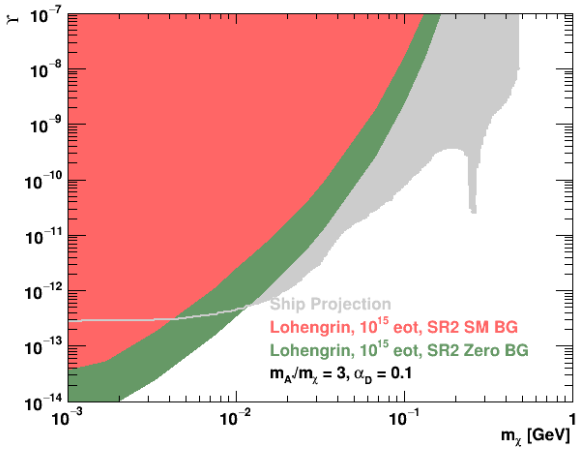

Figure 8.4: Estimated sensitivity of the LOHENGRIN experiment for the extended ECAL coverage, an extended beam time and the more aggressive signal electron phase space. The red area shows the expected sensitivity including the estimated number of background events, and the green area indicates the statistical limit for the sensitivity assuming a background free search (both limits are calculated at the 90% CL). The gray area shows the projected sensitivity of the SHiP experiment. In contrast to Fig. 8.2 and Fig. 8.3, in this figure a value of $\alpha_D = 0.1$ is assumed. Taken from [10].

Chapter 9

Conclusion and Outlook

This thesis presents a design study for a dark photon search experiment at ELSA. The theoretical foundations and motivation to search for such particles as a possible portal to the dark sector is established. The kinematics of the main signal process of dark photon creation are described. This includes an explanation how the specific kinematics can be used for a search experiment.

The idea for a possible detector is given and the requirements for each component determined. In this work, special emphasis is placed on the simulation of the electromagnetic calorimeter and tracking assembly, the two components most critical to the sensitivity of the experiment. It is shown, that the CALICE calorimeter prototype is a viable candidate in terms of energy resolution with a simple clustering algorithm and energy calibration, and signal processing capabilities given future improvements to the analogue signal processing.

The foreseen Lohengrin tracking assembly is constructed within ACTS, a toolkit designed to facilitate experiment agnostic tracking. Special emphasis is placed on the validation of the software implementation, especially concerning the accurate description of the material budget. A material validation is done and a GSF employed to successfully reconstruct electron momenta down to 25 MeV with a high efficiency.

Finally, a combined sensitivity estimate using results from the different detector components is established on the basis of theoretical calculations. Lohengrin can close the gap between existing limits and the relic target for different dark matter models under the assumption of a dark photon that kinetically mixes with the SM photon or hypercharge boson. The unique experimental strategy of looking for the disappearance of energy/-momentum, allows Lohengrin to be sensitive to extensions of the SM that go beyond the dark sector models that are used as a benchmark here [10]. It shows, that Lohengrin can be competitive to phase 1 of LDMX in parts of the phase space. For 1×10^{15} electrons on target and improvements in the reconstruction abilities of the tracker (lower momenta than 25 MeV), Lohengrin might even be able to outperform experiments with different experimental strategies like SHiP.

The realisation of the LOHENGRIN experiment has the potential to shed light on so far uncovered parts of the dark photon parameter space. The work presented in this thesis and in [10], shows that the operation of a missing momentum dark photon search experiment is feasible and can provide meaningful measurements. It is understood, that some significant R&D is required for the construction of an adequate tracking detector and ECAL. Significant potential for improvement exists in the increase of the angular coverage of the ECAL and improvements of the analogue signal processing (for the ECAL and trackers). The reconstruction of electron tracks down to the lowest possible momenta is another area with significant potential. The realisation could proceed in a phased approach, with each phase giving new insights and improving the confidence on the capabilities of the experimental approach outlined in this thesis.

Appendix A

Appendix

A.1 Generating Dark Photon Events with MadGraph5_aMC@NLO

Since the generation of dark photons is not part of the SM, such events can not be produced by running one of the default physics lists in Geant4. One of the options to get Monte Carlo generated events like shown in Fig. 2.7, is to use MadGraph5_aMC@NLO [114] in conjuntion with FeynRules [115].

A.1.1 FeynRules Setup

FeynRules is a Mathematica based package which allows the user to extract a so called UFO (Universal FeynRules Output) model from an arbitrary custom Lagrangian. This model can then be used as input to many event generators including MadGraph5_aMC@NLO. The first step is thus to include the Lagrangian, which allows for dark photon production to take place, in FeynRules.

The Lagrangian in Eqs. (2.8) and (2.11) can be used as a basis. However there is the need for an effective term which describes the interaction between the photon and the tungsten nucleus. One can make use of the fact, that $\approx 86\,\%$ of naturally occurring tungsten nuclei are scalars [116, 117]. The interaction is thus approximated with scalar QED [25]. This leads to the following Lagrangian being implemented in FeynRules:

$$\mathcal{L} = -\frac{1}{4}F'^{\mu\nu}F'_{\mu\nu} + \frac{m^2_{A'}}{2} - \epsilon e A'_\mu \bar{f}\gamma^\mu f + (\partial^\mu + ieA^\mu)\phi(\partial_\mu - ieA^\mu)\phi^* - m^2_\phi \phi\phi^* \qquad \text{(A.1)}$$

In Eq. (A.1), $F'_{\mu\nu} = \partial_\mu A'_\nu - \partial_\nu A'_\mu$ and ϕ represents the scalar tungsten nucleus with $m_\phi = 171\,\text{GeV}$ the approximate mass of the tungsten nucleus. This Lagrangian contains just the interactions necessary for dark photon production via dark Bremsstrahlung and the respective UFO model is then used in MadGraph5_aMC@NLO.

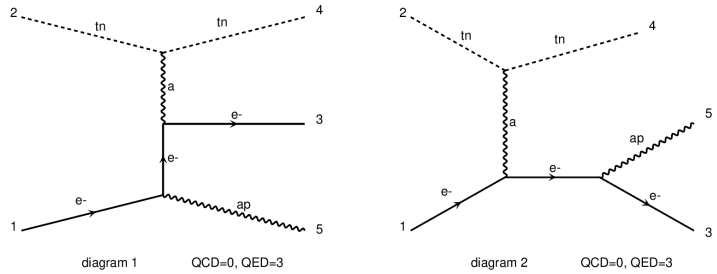

Figure A.1: `MadGraph5_aMC@NLO` generated Feynman diagrams for dark Bremsstrahlung. Differences to the common notation are: *tn* for the tungsten nucleus, *a* for the photon, *ap* for the dark photon, and *e-* for the electron.

A.1.2 `MadGraph5_aMC@NLO` Setup

The generated UFO model is then used as input for `MadGraph5_aMC@NLO`. It is possible to check whether this works by trying to generate Dark Bremsstrahlung events as the particles involved in that process are not all available with a default model. `MadGraph5_aMC@NLO` also outputs the relevant Feynman Diagrams, which are depicted in Fig. A.1. It shows the same processes as in Fig. 2.6 considering the simplifications highlighted in Appendix A.1.1 and excluding VCS.

The details of the tungsten nucleus photon interaction can be described with a custom form factor. This was done using the "Fortran Way" as it is described in [118]. The form factor $F(q^2)$, which is used, comes from the improved Weizsäcker-Williams approximation and is described in e.g. [119].

$$\begin{aligned} F(q^2) &= \left(\frac{-a^2q^2}{1-a^2q^2}\right)\left(\frac{1}{1-\frac{q^2}{d}}\right)\cdot Z^2, \\ \text{with } a &= 111\cdot\frac{Z^{-1/3}}{m_e} \text{ and } d = 0.164\,\text{GeV}^2\cdot A^{-2/3}. \end{aligned} \tag{A.2}$$

In Eq. (A.2) Z and A refer the number of protons and nucleons in the tungsten nucleus respectively. After these steps it is possible to generate dark Bremsstrahlung events following the steps outlined in [118]. The output is standardised in a Les-Houches event file. The format is explained in [120, 121]. A summary and algorithm on how to extract the relevant kinematic variables and include these generated events in a detector simulation are given [17].

A.1.3 Comparison to Theoretical Calculations

The kinematic variables of events generated with the setup given in this section can be compared to theoretical calculations using the same Lagrangian and form factors. This can be done qualitatively only, since events generated with `MadGraph5_aMC@NLO` are not normalised to any kind of cross section and only represent the kinematic distributions of dark bremsstrahlung events within the model described in this section. It is however possible to draw histograms of certain interesting kinematic variables and compare them to the normalised calculated cross sections of said variable. This is done in Fig. A.2[1]. The agreement is good enough for general statements regarding the behaviour of the involved particles.

The setup described in this section allows for the generation of events with any kind of custom Lagrangian. It can thus easily be used to be modified and improved at a later date. Such modifications might also include different mediator models.

A.2 Table of Energetically Possible Background Interactions Involving Hadrons

A table of energetically possible background events is given in Appendix A.2. It also indicates possible background rejection strategies by indicating relevant detector components. The notation works as follows: $|x$: can be measured by trackers, $\overline{x}$: can be vetoed by measuring energy in the ECA L, $|x|$: can be vetoed by ECAL hits, $\underline{x}$: can be vetoed by HCAL hits. Note that the table is not exhaustive but only illustrates the most basic final state combinations.

[1] The plots were made in collaboration with Martin Schürmann who also performed the theoretical calculations.

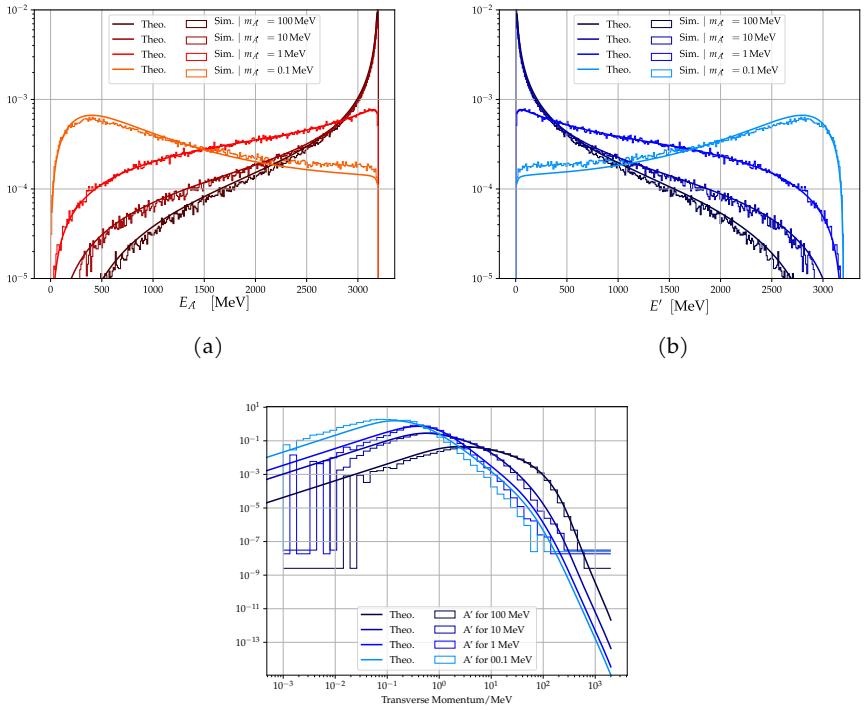

(a) (b)

(c)

Figure A.2: Comparison of kinematic variables including generated events with `MadGraph5_aMC@NLO` and theoretical calculations for different dark photon masses. Cross sections of theoretical calculations and histograms are normalised and displayed in a.u. s.t. a qualitative comparison is possible. (a): Distribution of the dark photon energy. (b): Distribution of the energy of the recoiling electron. (c): Transverse momentum of the recoiling electron

Process			
Elastic scattering	$e^- \mathcal{H} \to e^- \mathcal{H}$		
Bremsstrahlung	$e^- \mathcal{H} \to e^- \mathcal{H} \gamma$		
Subsequent photon conversion			
	$\gamma^\star \to e^+ \; e^-$	$\gamma^\star \to \mu^+ \; \mu^-$	
	$\gamma^\star \to \pi^0 + X$	$\gamma^\star \to \eta + X$	$\gamma^\star \to K^0 \; \bar{K}^0$
	$\gamma^\star \to \pi^+ \; \pi^-$		$\gamma^\star \to K^+ \; K^-$
	$\gamma^\star \to p \; \bar{p}$	$\gamma^\star \to n \; \bar{n}$	
Electro- and subsequent photonuclear processes w/ psudoscalar meson and baryon octet			
$\gamma^\star N \to \mathcal{B}$	$\gamma^\star p \to p$		
	$\gamma^\star n \to n$		
$\gamma^\star N \to \mathcal{M}\mathcal{B}$	$\gamma^\star p \to \pi^0 \; p$	$\gamma^\star p \to \eta \; p$	$\gamma^\star p \to K^0 \; \Sigma^+$
	$\gamma^\star p \to \pi^+ \; n$		$\gamma^\star p \to K^+ \; \Lambda/\Sigma^0$
	$\gamma^\star n \to \pi^0 \; n$	$\gamma^\star n \to \eta \; n$	$\gamma^\star n \to K^0 \; \Lambda/\Sigma^0$
	$\gamma^\star n \to \pi^- \; p$		$\gamma^\star n \to K^+ \; \Sigma^-$
$\gamma^\star N \to \mathcal{M}\mathcal{M}\mathcal{B}$	$\gamma^\star p \to \pi^+ \; \pi^- \; p$	$\gamma^\star p \to K^+ \; K^- \; p$	$\gamma^\star p \to \pi^+ \; K^0 \; \Lambda/\Sigma^0$
	$\gamma^\star p \to \pi^0 \; \pi^0 \; p$	$\gamma^\star p \to K^0_S \; K^0_L \; p$	$\gamma^\star p \to \pi^0 \; K^+ \; \Lambda/\Sigma^0$
	$\gamma^\star p \to \pi^+ \; \pi^0 \; n$		$\gamma^\star p \to \pi^0 \; K^0 \; \Sigma^+$
	$\gamma^\star n \to \pi^+ \; \pi^- \; n$	$\gamma^\star n \to K^+ \; K^- \; n$	$\gamma^\star n \to \pi^0 \; K^0 \; \Lambda/\Sigma^0$
	$\gamma^\star n \to \pi^0 \; \pi^0 \; n$	$\gamma^\star n \to K^0 \; \bar{K}^0 \; n$	$\gamma^\star n \to \pi^- \; K^+ \; \Lambda/\Sigma^0$
	$\gamma^\star n \to \pi^0 \; \pi^- \; p$		$\gamma^\star n \to \pi^\mp \; K^0 \; \Sigma^\pm$
$\gamma^\star N \to \mathcal{B}\bar{\mathcal{B}}\mathcal{B}$	$\gamma^\star p \to n \; \bar{n} \; p$	+ combinations with	
	$\gamma^\star p \to p \; \bar{p} \; p$	Σ and Λ baryons	
	$\gamma^\star n \to n \; \bar{n} \; n$		
	$\gamma^\star n \to p \; \bar{p} \; n$		

Table A.1: Table of energetically possible background events considering a 3.2 GeV electron beam. Possible rejection strategies are indicated by the detector component which can be used to veto the respective particles. The notation is to be understood like the following: line on the left: can be measured by tracker, line on top: can be vetoed by measuring ECAL energy, line on the right: can be vetoed due to hits in the ECAL, line on the bottom: can be vetoed by HCAL hits. Particularly challenging channels are marked in red. $\mathcal{H}$ represents a general hadronic target, while the symbols N, $\mathcal{M}$ and $\mathcal{B}$ indicate nucleons, mesons and baryons, respectively. X is a placeholder for multi-meson states.

Bibliography

[1] *Richard Wagner Verband International: Lohengrin*,
URL: https://www.richard-wagner.org/rwvi/de/richard-wagner/werke/?collection_id=115 (visited on 24/07/2024)
(cit. on p. I).

[2] M. Dine, W. Fischler and M. Srednicki,
A simple solution to the strong CP problem with a harmless axion,
Physics Letters B **104** (1981) 199, ISSN: 0370-2693,
URL: https://www.sciencedirect.com/science/article/pii/0370269381905906 (cit. on pp. 1, 6).

[3] M. Battaglieri et al., *US Cosmic Visions: New Ideas in Dark Matter 2017: Community Report*, 2017, arXiv: 1707.04591 [hep-ph] (cit. on pp. 1, 12).

[4] J. Alexander et al., *Dark Sectors 2016 Workshop: Community Report*, 2016,
arXiv: 1608.08632 [hep-ph] (cit. on pp. 1, 7, 10–12).

[5] R. Essig et al., *Working Group Report: New Light Weakly Coupled Particles*, 2013,
arXiv: 1311.0029 [hep-ph] (cit. on pp. 1, 7, 11).

[6] X. Chu, T. Hambye and M. H. G. Tytgat,
The Four Basic Ways of Creating Dark Matter Through a Portal, JCAP **05** (2012) 034,
arXiv: 1112.0493 [hep-ph] (cit. on pp. 1, 7).

[7] J. Blumlein and J. Brunner,
New Exclusion Limits for Dark Gauge Forces from Beam-Dump Data,
Phys. Lett. B **701** (2011) 155, arXiv: 1104.2747 [hep-ex] (cit. on pp. 1, 7).

[8] S. Andreas, C. Niebuhr and A. Ringwald,
New Limits on Hidden Photons from Past Electron Beam Dumps,
Phys. Rev. D **86** (2012) 095019, arXiv: 1209.6083 [hep-ph]
(cit. on pp. 1, 7).

[9] M. Graham, C. Hearty and M. Williams, *Searches for Dark Photons at Accelerators*,
Annual Review of Nuclear and Particle Science **71** (2021) 37, ISSN: 1545-4134, URL:
http://dx.doi.org/10.1146/annurev-nucl-110320-051823
(cit. on pp. 1, 7, 19, 20).

[10] P. Bechtle et al.,
A proposal for the Lohengrin experiment to search for dark sector particles at the ELSA Accelerator,
The European Physical Journal C **85** (2025) 600, ISSN: 1434-6052,
URL: https://doi.org/10.1140/epjc/s10052-025-14257-z
(cit. on pp. 1, 2, 10–12, 14–19, 21, 23, 25–29, 31, 41, 43–45, 47, 48, 50, 52, 54–57, 61–67, 83, 85, 87, 90, 94–104).

[11] E. Izaguirre, G. Krnjaic, P. Schuster and N. Toro,
Testing GeV-Scale Dark Matter with Fixed-Target Missing Momentum Experiments,
Phys. Rev. D **91** (2015) 094026, arXiv: 1411.1404 [hep-ph] (cit. on p. 1).

[12] S. Andreas, M. D. Goodsell and A. Ringwald,
Hidden Photons in connection to Dark Matter,
AIP Conf. Proc. **1563** (2013) 114, ed. by R. Milner, R. Carlini and F. Maas,
arXiv: 1306.1168 [hep-ph] (cit. on p. 1).

[13] E. Izaguirre, G. Krnjaic, P. Schuster and N. Toro,
Analyzing the Discovery Potential for Light Dark Matter, Phys. Rev. Lett. **115** (2015) 251301,
arXiv: 1505.00011 [hep-ph] (cit. on p. 1).

[14] J. Jaeckel, *A force beyond the Standard Model - Status of the quest for hidden photons*,
Frascati Phys. Ser. **56** (2012) 172, ed. by F. Bossi, S. Giovannella, P. Santangelo and B. Sciascia, arXiv: 1303.1821 [hep-ph] (cit. on p. 1).

[15] N. Blinov, G. Krnjaic and D. Tuckler,
Characterizing dark matter signals with missing momentum experiments,
Physical Review D **103** (2021), ISSN: 2470-0029,
URL: http://dx.doi.org/10.1103/PhysRevD.103.035030
(cit. on pp. 1, 8, 9).

[16] A. Berlin, N. Blinov, G. Krnjaic, P. Schuster and N. Toro, *Dark matter, millicharges, axion and scalar particles, gauge bosons, and other new physics with LDMX*,
Physical Review D **99** (2019), ISSN: 2470-0029,
URL: http://dx.doi.org/10.1103/PhysRevD.99.075001
(cit. on pp. 1, 8).

[17] J.-E. Heinrichs, *A First Simulation Study for a Light Dark Matter Experiment at ELSA*,
MA thesis: Universität Bonn, 2020, URL: https://web.physik.uni-bonn.de/group/view.php?&group=1&lang=de&c=t&id=119
(cit. on pp. 3, 22, 24, 25, 33, 71–73, 106).

[18] C. Burgard, *Texample: Standard model of physics*, Slightly adapted from original, 2016, URL: http://www.texample.net/tikz/examples/model-physics/ (visited on 29/08/2024) (cit. on p. 4).

[19] S. Abachi et al., *Observation of the top quark*, Physical Review Letters **74** (1995) 2632, arXiv: hep-ex/9503003 [hep-ex] (cit. on p. 3).

[20] F. Abe et al., *Observation of Top Quark Production in $\bar{p}p$ Collisions*, Physical Review Letters **74** (1995) 2626, ISSN: 1079-7114, URL: http://dx.doi.org/10.1103/PhysRevLett.74.2626 (cit. on p. 3).

[21] G. Aad et al., *Observation of a new particle in the search for the Standard Model Higgs boson with the ATLAS detector at the LHC*, Physics Letters B **716** (2012) 1, arXiv: 1207.7214 [hep-ex] (cit. on p. 3).

[22] S. Chatrchyan et al., *Observation of a new boson at a mass of 125 GeV with the CMS experiment at the LHC*, Physics Letters B **716** (2012) 30, arXiv: 1207.7235 [hep-ex] (cit. on p. 3).

[23] V. A. Bednyakov, N. D. Giokaris and A. V. Bednyakov, *On Higgs mass generation mechanism in the Standard Model*, Physics of Particles and Nuclei **39** (2008) 13, arXiv: hep-ph/0703280 [hep-ph] (cit. on p. 4).

[24] M. Thomson, "Modern Particle Phsyics", Cambridge University Press, 2013 4 (cit. on p. 4).

[25] M. D. Schwartz, *QUANTUM FIELD THEORY and the STANDARD MODEL*, Cambridge University Press, 2019, ISBN: 978-1-107-03473-0, URL: https://www.ebook.de/de/product/21354919/matthew_d_schwartz_quantum_field_theory_and_the_standard_model.html (cit. on pp. 5, 6, 10, 105).

[26] M. E. Peskin and D. V. Schroeder, *Introduction to Quantum Field Theory*, CRC Press, 2018, ISBN: 978-0-201-50397-5 (cit. on p. 5).

[27] Y. Fukuda et al., *Evidence for Oscillation of Atmospheric Neutrinos*, Phys. Rev. Lett. **81** (8 1998) 1562, URL: https://link.aps.org/doi/10.1103/PhysRevLett.81.1562 (cit. on p. 6).

[28] Y. Fukuda et al., *Measurement of the Flux and Zenith-Angle Distribution of Upward Throughgoing Muons by Super-Kamiokande*, Physical Review Letters **82** (1999) 2644, ISSN: 1079-7114, URL: http://dx.doi.org/10.1103/PhysRevLett.82.2644 (cit. on p. 6).

[29] Q. R. Ahmad et al., *Direct Evidence for Neutrino Flavor Transformation from Neutral-Current Interactions in the Sudbury Neutrino Observatory*, Physical Review Letters **89** (2002), ISSN: 1079-7114, URL: http://dx.doi.org/10.1103/PhysRevLett.89.011301 (cit. on p. 6).

[30] Q. R. Ahmad et al., *Measurement of the Rate of $\nu_e + d \rightarrow p + p + e^-$ Interactions Produced by ^8B Solar Neutrinos at the Sudbury Neutrino Observatory*, Phys. Rev. Lett. **87** (7 2001) 071301, URL: https://link.aps.org/doi/10.1103/PhysRevLett.87.071301 (cit. on p. 6).

[31] K. Eguchi et al., *First Results from KamLAND: Evidence for Reactor Antineutrino Disappearance*, Physical Review Letters **90** (2003), ISSN: 1079-7114, URL: http://dx.doi.org/10.1103/PhysRevLett.90.021802 (cit. on p. 6).

[32] F. P. An et al., *Observation of Electron-Antineutrino Disappearance at Daya Bay*, Physical Review Letters **108** (2012), ISSN: 1079-7114, URL: http://dx.doi.org/10.1103/PhysRevLett.108.171803 (cit. on p. 6).

[33] T. D. C. Collaboration, *Double Chooz θ13 measurement via total neutron capture detection*, Nature Physics **16** (2020) 558, ISSN: 1745-2481, URL: http://dx.doi.org/10.1038/s41567-020-0831-y (cit. on p. 6).

[34] D. G. Michael et al., *Observation of Muon Neutrino Disappearance with the MINOS Detectors in the NuMI Neutrino Beam*, Physical Review Letters **97** (2006), ISSN: 1079-7114, URL: http://dx.doi.org/10.1103/PhysRevLett.97.191801 (cit. on p. 6).

[35] K. Abe et al., *Indication of Electron Neutrino Appearance from an Accelerator-Produced Off-Axis Muon Neutrino Beam*, Physical Review Letters **107** (2011), ISSN: 1079-7114, URL: http://dx.doi.org/10.1103/PhysRevLett.107.041801 (cit. on p. 6).

[36] A. Abeln et al., *Conceptual design of BabyIAXO, the intermediate stage towards the International Axion Observatory*, JHEP **05** (2021) 137, arXiv: 2010.12076 [physics.ins-det] (cit. on p. 6).

[37] P. Schneider, *Extragalactic Astronomy and Cosmology - An Introduction*, Berlin New York: Springer, 2006, ISBN: 9783540331742 (cit. on pp. 6, 7).

[38] P. Mróz et al., *Rotation Curve of the Milky Way from Classical Cepheids*, The Astrophysical Journal **870** (2019) L10, ISSN: 2041-8213, URL: http://dx.doi.org/10.3847/2041-8213/aaf73f (cit. on p. 7).

[39] R. Massey, T. Kitching and J. Richard, *The dark matter of gravitational lensing*, Reports on Progress in Physics **73** (2010) 086901, ISSN: 1361-6633, URL: http://dx.doi.org/10.1088/0034-4885/73/8/086901 (cit. on pp. 7, 8).

[40] Y. Kahn, G. Krnjaic, S. Mishra-Sharma and T. M. P. Tait, *Light weakly coupled axial forces: models, constraints, and projections*, Journal of High Energy Physics **2017** (2017), ISSN: 1029-8479, URL: http://dx.doi.org/10.1007/JHEP05(2017)002 (cit. on p. 9).

[41] J. A. Dror, R. Lasenby and M. Pospelov, *Dark forces coupled to nonconserved currents*, Physical Review D **96** (2017), ISSN: 2470-0029, URL: http://dx.doi.org/10.1103/PhysRevD.96.075036 (cit. on p. 9).

[42] Amsterdam Cosmology Group, *Lecture Notes on Cosmology*, URL: http://cosmology.amsterdam/education/cosmology/ (visited on 20/02/2020) (cit. on p. 11).

[43] V. A. Rubakov and D. S. Gorbunov, *Introduction to the Theory of the Early Universe: Hot big bang theory*, Singapore: World Scientific, 2017, ISBN: 978-981-320-987-9 (cit. on p. 11).

[44] A. Berlin, N. Blinov, G. Krnjaic, P. Schuster and N. Toro, *Dark Matter, Millicharges, Axion and Scalar Particles, Gauge Bosons, and Other New Physics with LDMX*, Physical Review D **99** (2019) 075001, arXiv: 1807.01730 [hep-ph] (cit. on pp. 12, 19).

[45] T. Åkesson et al., *Light Dark Matter eXperiment (LDMX)*, 2018, arXiv: 1808.05219 [hep-ex] (cit. on pp. 12, 13, 19).

[46] J. L. Feng and J. Smolinsky,
Impact of a resonance on thermal targets for invisible dark photon searches,
Phys. Rev. D **96** (2017) 095022, arXiv: 1707.03835 [hep-ph] (cit. on p. 12).

[47] Geant4 Collaboration, *Book For Application Developers*, Release 11.3, 2024,
URL: https://geant4-userdoc.web.cern.ch/UsersGuides/ForApplicationDeveloper/fo/BookForApplicationDevelopers.pdf (cit. on pp. 15, 34).

[48] Geant4 Collaboration, *Guide For Physics Lists*, Release 11.3, 2024,
URL: https://geant4-userdoc.web.cern.ch/UsersGuides/PhysicsListGuide/fo/PhysicsListGuide.pdf (cit. on p. 15).

[49] D. Banerjee et al., *Dark Matter Search in Missing Energy Events with NA64*,
Phys. Rev. Lett. **123** (12 2019) 121801, URL: https://link.aps.org/doi/10.1103/PhysRevLett.123.121801 (cit. on pp. 15, 20, 100).

[50] E. Cortina Gil et al., *Search for dark photon decays to $\mu^+\mu^-$ at NA62*,
Journal of High Energy Physics **2023** (2023) 35, ISSN: 1029-8479,
URL: https://doi.org/10.1007/JHEP09(2023)035 (cit. on p. 15).

[51] D. Banerjee et al.,
Improved limits on a hypothetical $X(16.7)$ boson and a dark photon decaying into e^+e^- pairs,
Physical Review D **101** (2020), ISSN: 2470-0029,
URL: http://dx.doi.org/10.1103/PhysRevD.101.071101 (cit. on p. 15).

[52] A. A. Aguilar-Arevalo et al., *Dark matter search in nucleon, pion, and electron channels from a proton beam dump with MiniBooNE*, Physical Review D **98** (2018), ISSN: 2470-0029,
URL: http://dx.doi.org/10.1103/PhysRevD.98.112004 (cit. on pp. 15, 20, 100).

[53] J. Batley et al., *Search for the dark photon in $\pi 0$ decays*, Physics Letters B **746** (2015) 178,
ISSN: 0370-2693, URL: https://www.sciencedirect.com/science/article/pii/S0370269315003342 (cit. on p. 15).

[54] C. Ahdida et al.,
Sensitivity of the SHiP experiment to dark photons decaying to a pair of charged particles,
The European Physical Journal C **81** (2021), ISSN: 1434-6052,
URL: http://dx.doi.org/10.1140/epjc/s10052-021-09224-3 (cit. on p. 15).

[55] S. Abrahamyan et al., *Search for a New Gauge Boson in Electron-Nucleus Fixed-Target Scattering by the APEX Experiment*, Physical Review Letters **107** (2011), ISSN: 1079-7114, URL: http://dx.doi.org/10.1103/PhysRevLett.107.191804 (cit. on p. 15).

[56] H. Merkel et al., *Search at the Mainz Microtron for Light Massive Gauge Bosons Relevant for the Muon $g-2$ Anomaly*, Physical Review Letters **112** (2014), ISSN: 1079-7114, URL: http://dx.doi.org/10.1103/PhysRevLett.112.221802 (cit. on p. 15).

[57] Y. Hochberg, E. Kuflik, H. Murayama, T. Volansky and J. G. Wacker, *Model for Thermal Relic Dark Matter of Strongly Interacting Massive Particles*, Phys. Rev. Lett. **115** (2015) 021301, arXiv: 1411.3727 [hep-ph] (cit. on p. 19).

[58] Y. Hochberg, E. Kuflik and H. Murayama, *SIMP Spectroscopy*, JHEP **05** (2016) 090, arXiv: 1512.07917 [hep-ph] (cit. on p. 19).

[59] A. Berlin, N. Blinov, S. Gori, P. Schuster and N. Toro, *Cosmology and Accelerator Tests of Strongly Interacting Dark Matter*, Phys. Rev. D **97** (2018) 055033, arXiv: 1801.05805 [hep-ph] (cit. on p. 19).

[60] E. Kuflik, M. Perelstein, N. R.-L. Lorier and Y.-D. Tsai, *Elastically Decoupling Dark Matter*, Phys. Rev. Lett. **116** (2016) 221302, arXiv: 1512.04545 [hep-ph] (cit. on p. 19).

[61] E. Kuflik, M. Perelstein, N. R.-L. Lorier and Y.-D. Tsai, *Phenomenology of ELDER Dark Matter*, JHEP **08** (2017) 078, arXiv: 1706.05381 [hep-ph] (cit. on p. 19).

[62] K. Petraki and R. R. Volkas, *Review of asymmetric dark matter*, Int. J. Mod. Phys. A **28** (2013) 1330028, arXiv: 1305.4939 [hep-ph] (cit. on p. 19).

[63] K. M. Zurek, *Asymmetric Dark Matter: Theories, Signatures, and Constraints*, Phys. Rept. **537** (2014) 91, arXiv: 1308.0338 [hep-ph] (cit. on p. 19).

[64] L. J. Hall, K. Jedamzik, J. March-Russell and S. M. West, *Freeze-In Production of FIMP Dark Matter*, JHEP **03** (2010) 080, arXiv: 0911.1120 [hep-ph] (cit. on p. 19).

[65] M. J. Baker, M. Breitbach, J. Kopp and L. Mittnacht, *Dynamic freeze-in: impact of thermal masses and cosmological phase transitions on dark matter production*, Journal of High Energy Physics **2018** (2018), ISSN: 1029-8479, URL: http://dx.doi.org/10.1007/JHEP03(2018)114 (cit. on p. 19).

[66] M. Becker, E. Copello, J. Harz, J. Lang and Y. Xu, *Confronting dark matter freeze-in during reheating with constraints from inflation*, Journal of Cosmology and Astroparticle Physics **2024** (2024) 053, ISSN: 1475-7516, URL: http://dx.doi.org/10.1088/1475-7516/2024/01/053 (cit. on p. 19).

[67] J. Jaeckel and A. Ringwald, *The Low-Energy Frontier of Particle Physics*, Ann. Rev. Nucl. Part. Sci. **60** (2010) 405, arXiv: 1002.0329 [hep-ph] (cit. on p. 19).

[68] P. Ilten, Y. Soreq, M. Williams and W. Xue, *Serendipity in dark photon searches*, JHEP **06** (2018) 004, arXiv: 1801.04847 [hep-ph] (cit. on p. 19).

[69] S. Dodelson and L. M. Widrow, *Sterile-neutrinos as dark matter*, Phys. Rev. Lett. **72** (1994) 17, arXiv: hep-ph/9303287 (cit. on p. 19).

[70] DELPHI Collaboration, *Photon events with missing energy in e + e- collisions at $\sqrt{s}$ = 130 to 209 GeV*, The European Physical Journal C **38** (2005) 395, ISSN: 1434-6052, URL: http://dx.doi.org/10.1140/epjc/s2004-02051-8 (cit. on pp. 20, 100).

[71] J. Abdallah et al., *Search for one large extra dimension with the DELPHI detector at LEP*, The European Physical Journal C **60** (2009) 17, ISSN: 1434-6052, URL: http://dx.doi.org/10.1140/epjc/s10052-009-0874-9 (cit. on pp. 20, 100).

[72] P. J. Fox, R. Harnik, J. Kopp and Y. Tsai, *LEP shines light on dark matter*, Physical Review D **84** (2011), ISSN: 1550-2368, URL: http://dx.doi.org/10.1103/PhysRevD.84.014028 (cit. on pp. 20, 100).

[73] J. P. Lees et al., *Search for Invisible Decays of a Dark Photon Produced in e^+e^- Collisions at BaBar*, Physical Review Letters **119** (2017), ISSN: 1079-7114, URL: http://dx.doi.org/10.1103/PhysRevLett.119.131804 (cit. on pp. 20, 100).

[74] E. Cortina Gil et al., *Search for production of an invisible dark photon in π^0 decays*, Journal of High Energy Physics **2019** (2019), ISSN: 1029-8479, URL: http://dx.doi.org/10.1007/JHEP05(2019)182 (cit. on pp. 20, 100).

[75] P. deNiverville, M. Pospelov and A. Ritz, *Observing a light dark matter beam with neutrino experiments*, Phys. Rev. D **84** (7 2011) 075020, URL: https://link.aps.org/doi/10.1103/PhysRevD.84.075020 (cit. on pp. 20, 100).

[76] G. Angloher et al., *Results on light dark matter particles with a low-threshold CRESST-II detector*, The European Physical Journal C **76** (2016), ISSN: 1434-6052, URL: http://dx.doi.org/10.1140/epjc/s10052-016-3877-3 (cit. on pp. 20, 100).

[77] A. H. Abdelhameed et al., *First results from the CRESST-III low-mass dark matter program*, Physical Review D **100** (2019), ISSN: 2470-0029, URL: http://dx.doi.org/10.1103/PhysRevD.100.102002 (cit. on pp. 20, 100).

[78] E. Aprile et al., *Light Dark Matter Search with Ionization Signals in XENON1T*, Physical Review Letters **123** (2019), ISSN: 1079-7114, URL: http://dx.doi.org/10.1103/PhysRevLett.123.251801 (cit. on pp. 20, 100).

[79] M. Bauer, P. Foldenauer and J. Jaeckel, *Hunting all the hidden photons*, Journal of High Energy Physics **2018** (2018), ISSN: 1029-8479, URL: http://dx.doi.org/10.1007/JHEP07(2018)094 (cit. on p. 19).

[80] A. Andrianavalomahefa et al., *Search for dark photons as candidates for Dark Matter with FUNK*, PoS **ICRC2019** (2021) 517 (cit. on p. 20).

[81] A. Anastasi et al., *Combined limit on the production of a light gauge boson decaying into $\mu+\mu-$ and $\pi+\pi-$*, Physics Letters B **784** (2018) 336, ISSN: 0370-2693, URL: http://dx.doi.org/10.1016/j.physletb.2018.08.012 (cit. on p. 20).

[82] M. Ablikim et al., *Dark Photon Search in the Mass Range Between 1.5 and 3.4 GeV/c^2*, Phys. Lett. B **774** (2017) 252, arXiv: 1705.04265 [hep-ex] (cit. on p. 20).

[83] R. Aaij et al., *Search for Dark Photons Produced in 13 TeV pp Collisions*, Phys. Rev. Lett. **120** (6 2018) 061801, URL: https://link.aps.org/doi/10.1103/PhysRevLett.120.061801 (cit. on p. 20).

[84] R. Aaij et al., *Search for $A' \to \mu^+\mu^-$ Decays*, Phys. Rev. Lett. **124** (4 2020) 041801, URL: https://link.aps.org/doi/10.1103/PhysRevLett.124.041801 (cit. on p. 20).

[85] V. Gorkavenko et al., *LHCb potential to discover long-lived new physics particles with lifetimes above 100 ps*, The European Physical Journal C **84** (2024), ISSN: 1434-6052, URL: http://dx.doi.org/10.1140/epjc/s10052-024-12906-3 (cit. on p. 20).

[86] H. Abreu et al., *Search for dark photons with the FASER detector at the LHC*, Physics Letters B **848** (2024) 138378, ISSN: 0370-2693, URL: http://dx.doi.org/10.1016/j.physletb.2023.138378 (cit. on p. 20).

[87] The ELSA-Group, *The Accelerator*, URL: https://www.pi.uni-bonn.de/elsa/en/ (visited on 18/12/2024) (cit. on p. 22).

[88] Nikolas Heurich, *Die externe Strahlführung für Detektortests X3ED an der Elektronen-Stretcher-Anlage ELSA*, PhD thesis: Rheinische Friedrich-Wilhelms-Universität Bonn, 2017, URL: https://hdl.handle.net/20.500.11811/7310 (cit. on p. 21).

[89] M. Pullia, *Slow extraction dynamics and its influence on transfer lines design*, PhD thesis: TERA, Novara, 1999, URL: https://inspirehep.net/record/511446?ln=en (cit. on pp. 22–24).

[90] K. Wille, *The Physics of Particle Accelerators - An Introduction*, Oxford University Press, 2005, 332 pp., ISBN: 9780198505495, URL: https://www.ebook.de/de/product/2758400/klaus_wille_the_physics_of_particle_accelerators.html (cit. on pp. 22, 23).

[91] B. Goddard, *Injection & Extraction*,
Talk given during Introduction to Accelerator Physics 2009, 2009,
URL: https://indico.cern.ch/event/43703/contributions/1086895/attachments/939252/1331885/Goddard.pdf.pdf
(visited on 07/01/2025) (cit. on p. 24).

[92] K. Moustakas et al.,
CMOS monolithic pixel sensors based on the column-drain architecture for the HL-LHC upgrade,
Nuclear Instruments and Methods in Physics Research Section A: Accelerators, Spectrometers, Detectors and Associated Equipment **936** (2019) 604, Frontier Detectors for Frontier Physics: 14th Pisa Meeting on Advanced Detectors,
ISSN: 0168-9002, URL: https://www.sciencedirect.com/science/article/pii/S0168900218312531 (cit. on p. 30).

[93] I. Caicedo et al.,
Improvement in the Design and Performance of the Monopix2 Reticle-Scale DMAPS,
JPS Conf. Proc. **42** (2024) 011021 (cit. on p. 30).

[94] O. Freyermuth, *Studies of ω Photoproduction off Proton at the BGO-OD Experiment*,
PhD thesis: Universität Bonn, 2017,
URL: https://hdl.handle.net/20.500.11811/7263
(cit. on p. 33).

[95] ROOT Team, *ROOT: analyzing petabytes of data, scientifically.* 2024,
URL: https://root.cern.ch/ (visited on 29/12/2024) (cit. on p. 33).

[96] Geant4 Collaboration, *The GEANT4 website*,
URL: https://geant4.web.cern.ch (visited on 29/12/2024)
(cit. on p. 34).

[97] *ExPlORA source code for the Lohengrin project*, Access might have to be requested from the administrators depending on the reader's access rights., URL:
https://bitbucket.team.uni-bonn.de/projects/PHYLHNG/
(cit. on p. 35).

[98] H. Kolanoski and N. Wermes, *Teilchendetektoren - Grundlagen und Anwendungen*,
Springer, 2016, ISBN: 978-3-662-45349-0,
URL: https://www.ebook.de/de/product/25501763/hermann_kolanoski_norbert_wermes_teilchendetektoren.html
(cit. on pp. 46, 47, 52, 59, 62, 68, 72, 89).

[99] W. Heitler, *The Quantum Theory of Radiation*, Clraendon Press, 1954 (cit. on p. 46).

[100] R. Pöschl, *The CALICE SiW ECAL Technological Prototype—Status and Outlook*, Instruments **6** (2022), ISSN: 2410-390X, URL: https://www.mdpi.com/2410-390X/6/4/75 (cit. on pp. 54, 55, 62).

[101] *Acts: Read the Docs*, URL: https://acts.readthedocs.io/en/stable/index.html (visited on 15/05/2025) (cit. on pp. 67, 68, 72, 74, 81, 82).

[102] X. Ai et al., *A Common Tracking Software Project*, 2021, arXiv: 2106.13593 [physics.ins-det] (cit. on pp. 67, 68, 70, 72, 78, 79).

[103] B. Huth, *Track reconstruction for future high-energy-physics experiments with classical and machine-learning methods*, PhD thesis, 2024, URL: https://epub.uni-regensburg.de/55604/ (cit. on pp. 68–78, 87, 88, 92).

[104] R. Fruehwirth and A. Strandlie, *Pattern recognition and estimation methods for track and vertex reconstruction*, PoS **ACAT2010** (2011) 003 (cit. on p. 69).

[105] R. Frühwirth, *Track fitting with non-Gaussian noise*, Computer Physics Communications **100** (1997) 1, ISSN: 0010-4655, URL: https://www.sciencedirect.com/science/article/pii/S0010465596001555 (cit. on p. 76).

[106] S. Navas et al., *Review of particle physics*, Phys. Rev. D **110** (2024) 030001 (cit. on p. 77).

[107] R. Frühwirth, *A Gaussian-mixture approximation of the Bethe–Heitler model of electron energy loss by bremsstrahlung*, Computer Physics Communications **154** (2003) 131, ISSN: 0010-4655, URL: https://www.sciencedirect.com/science/article/pii/S0010465503002923 (cit. on pp. 76, 77).

[108] R. Chytracek, "The Geometry Description Markup Language", *Proceedings of CHEP 2001*, Science Press, 2001 473 (cit. on p. 79).

[109] M. Zinser, "The ATLAS Experiment", *Search for New Heavy Charged Bosons and Measurement of High-Mass Drell-Yan Production in Proton—Proton Collisions*, Cham: Springer International Publishing, 2018 53, ISBN: 978-3-030-00650-1, URL: https://doi.org/10.1007/978-3-030-00650-1_5 (cit. on pp. 79, 83).

[110] R. Gluckstern,
Uncertainties in track momentum and direction, due to multiple scattering and measurement errors,
Nuclear Instruments and Methods **24** (1963) 381, ISSN: 0029-554X,
URL: https://www.sciencedirect.com/science/article/pii/0029554X63903471 (cit. on p. 89).

[111] M. Graham, C. Hearty and M. Williams, *Searches for Dark Photons at Accelerators*,
Ann. Rev. Nucl. Part. Sci. **71** (2021) 37, arXiv: 2104.10280 [hep-ph] (cit. on p. 100).

[112] T. Åkesson et al., *Current Status and Future Prospects for the Light Dark Matter eXperiment*,
2022, arXiv: 2203.08192 [hep-ex] (cit. on p. 100).

[113] C. Ahdida et al., *Sensitivity of the SHiP experiment to light dark matter*,
JHEP **2104** (2021) 199, 39 pages, 14 figures, 5 tables. v2: extended version as published on JHEP, arXiv: 2010.11057,
URL: https://cds.cern.ch/record/2743145 (cit. on p. 101).

[114] J. Alwall et al., *The automated computation of tree-level and next-to-leading order differential cross sections, and their matching to parton shower simulations*,
Journal of High Energy Physics **2014** (2014), ISSN: 1029-8479,
URL: http://dx.doi.org/10.1007/JHEP07(2014)079 (cit. on p. 105).

[115] A. Alloul, N. D. Christensen, C. Degrande, C. Duhr and B. Fuks,
FeynRules 2.0 — A complete toolbox for tree-level phenomenology,
Computer Physics Communications **185** (2014) 2250, ISSN: 0010-4655,
URL: http://dx.doi.org/10.1016/j.cpc.2014.04.012 (cit. on p. 105).

[116] J. R. de Laeter et al., *Atomic weights of the elements. Review 2000 (IUPAC Technical Report)*,
Pure and Applied Chemistry **75** (2003) 683,
URL: https://doi.org/10.1351/pac200375060683 (cit. on p. 105).

[117] National Nuclear Data Center at Brookhaven National Laboratory,
The NuDat3 Database, Contains information on spin states of tungsten nuclei, 2024,
URL: https://www.nndc.bnl.gov/nudat3/ (visited on 31/12/2024) (cit. on p. 105).

[118] O. Mattelaer, *The MadGraph5_aMC@NLO Wiki*, 2021,
URL: https://cp3.irmp.ucl.ac.be/projects/madgraph/wiki (visited on 31/12/2024) (cit. on p. 106).

[119] J. D. Bjorken, R. Essig, P. Schuster and N. Toro,
New fixed-target experiments to search for dark gauge forces, Physical Review D **80** (2009),
ISSN: 1550-2368,
URL: http://dx.doi.org/10.1103/PhysRevD.80.075018
(cit. on p. 106).

[120] J. Alwall et al., *A standard format for Les Houches Event Files*,
Computer Physics Communications **176** (2007) 300, ISSN: 0010-4655,
URL: http://dx.doi.org/10.1016/j.cpc.2006.11.010
(cit. on p. 106).

[121] E. Boos et al., *Generic User Process Interface for Event Generators*, 2001,
arXiv: hep-ph/0109068 [hep-ph] (cit. on p. 106).

List of Figures

List of Tables

Listings